Phase Behavior of

Complex Superprotonic Solid Acids

Thesis by

Chatr Panithipongwut

In Partial Fulfillment of the Requirements

For the Degree of

Doctor of Philosophy

California Institute of Technology

Pasadena, California

2013

(Defended May 17th, 2013)

Acknowledgements

Firstly and most importantly, I would like to thank Professor Sossina Haile, Professor William Johnson, Professor George Rossman, and Professor Kaushik Bhattacharya for reading and correcting my thesis. Professor Sossina Haile has been an amazing and caring advisor since I joined the group. Discussions with her always encouraged me to think about my work critically and find the connections and explanations for the results based on theories and previously reported data. Her guidance, patience and support were so valuable to me especially when I was clouded and could not think clearly. Also, I would like to thank Professor Axel van de Walle who was one of my candidacy committee members. This work was made possible by financial support provided by the U.S. National Science Foundation (DMR-0906543) and the Army Research Office (W911NF-07-1-0410). The Ministry of Science and Technology of Thailand through the Royal Thai Scholarship provided additional funding in the form of tuition and stipend.

I was fortunate to work with many exceptional collaborators and colleagues. I am grateful to Dr. Mary Louie who helped me a lot in many ways in both life and work, including general knowledge about solid acids, martensitic theory, measurement techniques, operating test stations and many other things. When I had work or life problems, she was always a good listener and gave me good suggestions. I thank Professor William Chueh, who also was my colleague and had and still has made a lot of contributions to the group, from some little things to some high-impact findings. My

conductivity measurements would have been more complicated without his well-written data-collection program. For those who helped, taught me or exchanged knowledge about how to operate, set up experimental conditions properly and perform data analysis, I thank Dr. Yoshihiro Yamazaki and Dr. Joon-Hyung Lee for DSC; Dr. Ayako Ikeda and Dr. Mikhail Kislitsyn for XRD; Dr. Aron Varga and Rob Usiskin for electrospray; Dr. Chi Ma and June Wicks in GPS division for SEM and EDS; and Fenton Harvey for general lab equipment. I thank Dr. Taesik Oh for discussions and answers to my random questions and for giving me some ideas for my research even though it was out of his area. Additionally, to Dr. Calum Chisholm and Dr. Lisa Cowan, for the initiation of wonderful solid acid works that I picked up and continued, I thank both of you.

There are many other individuals to whom I owe credits for this achievement and without whom I would not be able to complete my road to my Ph.D. I would like to thank Nicholas Eugene Scianmarello, who was my first SURF mentee and later became a friend and a supporter who somehow helped me through my candidacy exam. I give many thanks to Jeffrey Adam Kowalski, another SURF mentee and a very good friend, for helping me with some sample preparations and discussions, giving me some ideas on my work, inspiring me to do better things in life and take better care of myself, supporting me through the finish line of the Ph.D. program and for many other things I cannot describe. I thank Wolfgang Gerhard Zeier, my office mate, roommate, and a good friend, for all support and encouragements when I needed them. I also thank Stephen Wilke for figuring out the mistake in my enthalpy calculation, discussions about many other things, general talks about both work and life, and the support that he always provided. I was

lucky to have some others who enjoyed and fought together through the same program, namely Dr. Nicholas Stadie, Dr. Aron Varga, Scott Robers, and Jorge Munoz. Marcel Schreier, Carolyn Richmonds and Michael Ignatowich were friends with whom I spent some time outside the lab for good food and relief from stress towards the end of my residency. I thank Chirranjeevi BG for carrying the TA duty for a week when I was finishing my thesis writing.

Lastly, I am grateful to my family and friends in Thailand and in the U.S. for love and support, especially my parents, who encouraged and supported my decision to come to study abroad, and my siblings who took care of everything to ease my worry about my family and let me concentrate on my study.

Abstract

Superprotonic phase transitions and thermal behaviors of three complex solid acid systems are presented, namely $Rb_3H(SO_4)_2$-$RbHSO_4$ system, $Rb_3H(SeO_4)_2$-$Cs_3H(SeO_4)_2$ solid solution system, and $Cs_6(H_2SO_4)_3(H_{1.5}PO_4)_4$. These material systems present a rich set of phase transition characteristics that set them apart from other, simpler solid acids. A.C. impedance spectroscopy, high-temperature X-ray powder diffraction, and thermal analysis, as well as other characterization techniques, were employed to investigate the phase behavior of these systems.

$Rb_3H(SO_4)_2$ is an atypical member of the $M_3H(XO_4)_2$ class of compounds (M = alkali metal or NH_4^+ and X = S or Se) in that a transition to a high-conductivity state involves disproportionation into two phases rather than a simple polymorphic transition [1]. In the present work, investigations of the $Rb_3H(SO_4)_2$-$RbHSO_4$ system have revealed the disproportionation products to be Rb_2SO_4 and the previously unknown compound $Rb_5H_3(SO_4)_4$. The new compound becomes stable at a temperature between 25 and 140 °C and is isostructural to a recently reported trigonal phase with space group $P\bar{3}m$ of $Cs_5H_3(SO_4)_4$ [2]. At 185 °C the compound undergoes an apparently polymorphic transformation with a heat of transition of 23.8 kJ/mol and a slight additional increase in conductivity.

The compounds $Rb_3H(SeO_4)_2$ and $Cs_3H(SeO_4)_2$, though not isomorphous at ambient temperatures, are quintessential examples of superprotonic materials. Both adopt monoclinic structures at ambient temperatures and ultimately transform to a trigonal ($R\bar{3}m$) superprotonic structure at slightly elevated temperatures, 178 and 183 °C, respectively. The compounds are completely miscible above the superprotonic transition

and show extensive solubility below it. Beyond a careful determination of the phase boundaries, we find a remarkable 40-fold increase in the superprotonic conductivity in intermediate compositions rich in Rb as compared to either end-member.

The compound $Cs_6(H_2SO_4)_3(H_{1.5}PO_4)_4$ is unusual amongst solid acid compounds in that it has a complex cubic structure at ambient temperature and apparently transforms to a simpler cubic structure of the CsCl-type (isostructural with CsH_2PO_4) at its transition temperature of 100-120 °C [3]. Here it is found that, depending on the level of humidification, the superprotonic transition of this material is superimposed with a decomposition reaction, which involves both exsolution of (liquid) acid and loss of H_2O. This reaction can be suppressed by application of sufficiently high humidity, in which case $Cs_6(H_2SO_4)_3(H_{1.5}PO_4)_4$ undergoes a true superprotonic transition. It is proposed that, under conditions of low humidity, the decomposition/dehydration reaction transforms the compound to $Cs_6(H_{2-0.5x}SO_4)_3(H_{1.5}PO_4)_{4-x}$, also of the CsCl structure type at the temperatures of interest, but with a smaller unit cell. With increasing temperature, the decomposition/dehydration proceeds to greater and greater extent and unit cell of the solid phase decreases. This is identified to be the source of the apparent negative thermal expansion behavior.

References

[1] L.A. Cowan, R.M. Morcos, N. Hatada, A. Navrotsky, S.M. Haile, *Solid State Ionics* **179** (2008) (9-10) 305.
[2] M. Sakashita, H. Fujihisa, K.I. Suzuki, S. Hayashi, K. Honda, *Solid State Ionics* **178** (2007) (21-22) 1262.
[3] C.R.I. Chisholm, Superprotonic Phase Transitions in Solid Acids: Parameters affecting the presence and stability of superprotonic transitions in the MHnXO4 family of compounds (X=S, Se, P, As; M=Li, Na, K, NH4, Rb, Cs), *Materials Science*, California Institute of Technology, Pasadena, California (2003).

Table of Contents

List of Figures

List of Tables

List of Abbreviations and Symbols

a_0	Lattice constant of a cubic crystal
ACIS	A.C. impedance spectroscopy
B	Isotropic displacement parameter
DSC	Differential scanning calorimetry
GOF	Goodness of fit
HT	High temperature
LT	Low temperature
pH_2O	Water partial pressure
R_{Bragg}	Bragg residual (Rietveld refinement)
R_{exp}	Expected profile residual (Rietveld refinement)
R_{wp}	Weighted profile residual (Rietveld refinement)
SEM	Scanning electron microscopy
T_{SP}	Superprotonic transition temperature
TG	Thermal gravimetry
V	Unit cell volume
XRD	X-ray diffraction
Z	Number of formula units per unit cell

Chapter 1 Introduction

1.1 Solid Acids and Superprotonic Transition

A solid acid compound is an acid salt of a polyprotic acid that contains at least one acidic proton. Examples of these polyprotic acids are H_2SO_4, H_3PO_4, H_2SeO_4, and H_3AsO_4 and simple examples of solid acids are $CsHSO_4$ and CsH_2PO_4, which are well studied and can be prepared from various reactants. Sample reactions to form these compounds are:

Cs_2CO_3 (base) + 2 H_3PO_4 (polyprotic acid) → 2 CsH_2PO_4 (solid acid) + H_2O + CO_2

Cs_2SO_4 (salt) + H_2SO_4 (polyprotic acid) → 2 $CsHSO_4$ (solid acid)

Complex solid acids can be synthesized similarly using different bases, salts, acids, or mixtures of acids. Alternatively, they can be prepared from a mixture of two solid acids.

Solid acids can be classified under four groups: $MHXO_4$, $M_3H(XO_4)_2$, $M_5H_3(XO_4)_4$, and $mMHXO_4 \cdot MH_2ZO_4$ where commonly M = Cs, Rb, K, NH_4; X = S, Se; Z = P. Most of the solid acids are water-soluble and insulating at room temperature. At higher temperature, many of them are considered to be proton conductors as they exhibit dramatic changes in conductivity in the temperature range between ~ 100 and 300 °C. This characteristic becomes more of interest because the transition temperatures fall into the moderate temperature range of fuel cells where fuel flexibility, efficiency, and easiness of thermal cycling are optimal.

The transition giving this sudden increase in conductivity is called a superprotonic transition and the proton conductivity due to this transition usually increases by 3-4 orders of magnitude, as seen in Figure 1.1. These phenomena originate from the crystallographic transitions of solid acids from their low-symmetry, low-temperature

phases to high-symmetry, high-temperature phases, which change the arrangements of hydrogen bonds from ordered to disordered. This allows oxyanion reorientations followed by proton transfers, which are the mechanism of proton conductivity, to occur much faster which consequently increases the conductivity [1].

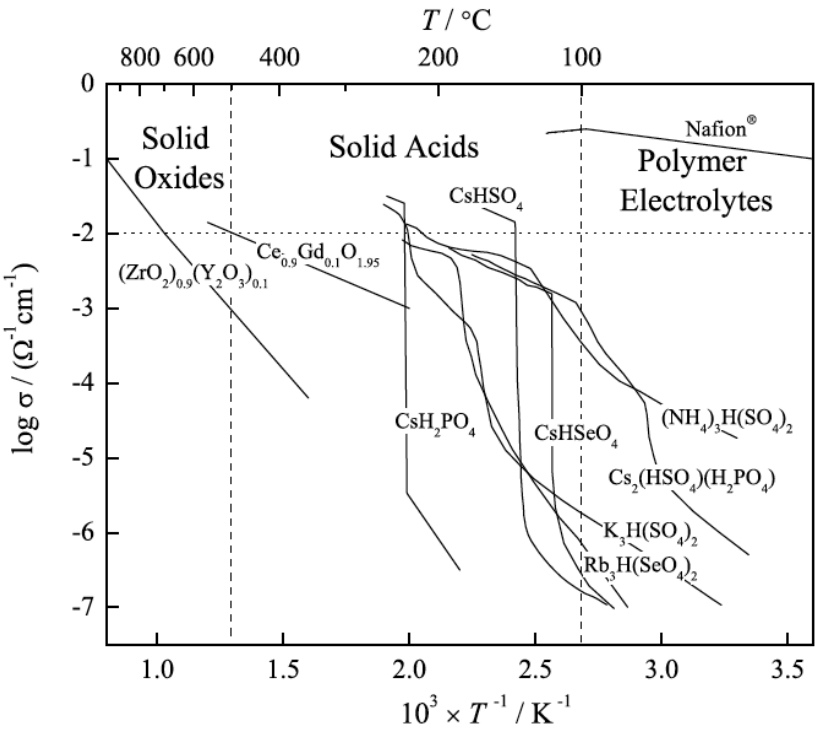

Figure 1.1. Conductivity of various fuel cell electrolytes, reproduced from [2].

1.2 Objectives

The main objectives of this study are to explore the properties of three complex solid acid systems, to understand the process of the superprotonic transitions, and to establish the phase diagrams. The challenge of this work is that many solid acids have similar physical, measurable properties, such as the increase in conductivity, and

sometimes mislead the researcher to jump to the same conclusion due to these similarities.

1.3 The Solid Acid Systems of Interest

In the following chapters, the results presented here will reveal that among these similarities, there is a unique behavior happens in each system. Also, some results that were mistakenly interpreted in the past are now re-evaluated taking into account new evidence. It is also shown that the solid acid systems are not less complicated than other types of materials and while general trends were established, it may not apply to another system even though they seem to be close to each other.

The solid acid systems investigated in this thesis are:

1) $Rb_3H(SO_4)_2$-$RbHSO_4$ mixtures
2) $Rb_3H(SeO_4)_2$-$Cs_3H(SeO_4)_2$ solid solutions – $(Cs_xRb_{1-x})_3H(SeO_4)_2$
3) $Cs_6(H_2SO_4)_3(H_{1.5}PO_4)_4$

The compounds listed in the titles of the three systems here are thermodynamically stable at room temperature and some of which will definitely change; either react, transform, disproportionate, or decompose; to other compounds at higher temperature.

$Rb_3H(SO_4)_2$, like many other solid acids in the family, shows a sharp rise in conductivity at ~ 205 °C with a hysteresis of about 30 °C on cooling. This observation was quickly conceived as a polymorphic superprotonic transition by various researchers [3-6]. Cowan et al. [7] discovered that although the compound is isostructural to others in the family at room temperature, the reaction happening here was not a polymorphic

transition, but a disproportionation of $Rb_3H(SO_4)_2$ to Rb_2SO_4 and another solid acid that must have a stoichiometry between $Rb_3H(SO_4)_2$ and $RbHSO_4$ and that is superprotonic phase in nature. In Chapter 3, further investigation of this case is presented. Starting from $Rb_3H(SO_4)_2$ and $RbHSO_4$, it is found that the two solid acids react and form a new compound $Rb_5H_3(SO_4)_4$ at a temperature as low as 140 °C and it adopts the same structure as the intermediate-temperature $Cs_5H_3(SO_4)_4$ [8]. At 185 °C, this compound undergoes a polymorphic superprotonic transition to its high-temperature, high-conductivity phase which gives an X-ray diffraction pattern similar to that of the high-temperature $Cs_5H_3(SO_4)_4$ [8]. This phase is stable beyond the temperature that $Rb_3H(SO_4)_2$ disproportionates and is confirmed that it is the other product of the disproportionation.

Chapter 4 discusses about the properties of solid solutions between $Rb_3H(SeO_4)_2$ and $Cs_3H(SeO_4)_2$. The system demonstrates noteworthy findings. The most significant is 40-fold increase in the superprotonic conductivity in the Rb-rich compositions as compared to either end member, while previously found in doped CsH_2PO_4 systems, the superprotonic conductivities of those solid solutions decreased with the doping level [9]. Another interesting result is the trend of the superprotonic transition temperature. In other solid solution systems, the trend of transition temperature shows one direction, i.e. either increasing or decreasing, with the content of the dopant. For example, in the $Cs_{1-x}Rb_xH_2PO_4$ system, the transition temperature increases with the rubidium content [9, 10]. $(Cs_xRb_{1-x})_3H(SeO_4)_2$ system, on the other hand, shows a minimum in transition temperature near the middle composition. Chisholm [11] attempted to find the driving force of superprotonic transitions of solid acids when line compounds in $CsHSO_4$-

CsH_2PO_4 family were chosen to represent solid acids with different transition temperatures and configurations of the oxyanions in the structures. The conclusion from this $CsHSO_4$-CsH_2PO_4 family was that the configurational entropy of the superprotonic transition provides the driving force. For $(Cs_xRb_{1-x})_3H(SeO_4)_2$ system, the configurational entropy is approximately constant across the compositions since all of them have the same high-temperature and low-temperature phases. The variation in the superprotonic transition temperature is set by the variation of the enthalpy, which could reflect differences in H-bond across the compositions.

$Cs_6(H_2SO_4)_3(H_{1.5}PO_4)_4$ is the only system here that starts with a single compound. It should be noted that the material, however, is composed of many more ions compared to other solid acids discovered to date. This compound was also studied along with the others in $CsHSO_4$-CsH_2PO_4 family [11] and found that it was the only one that did not have Cs:(S+P) mole ratio equals to 1, was a cubic at room temperature, and seemed to have negative thermal expansion in the high-temperature phase. However, other properties seemed similar to those of the other compounds in the family. Chapter 5 of this thesis will show that the transition of $Cs_6(H_2SO_4)_3(H_{1.5}PO_4)_4$ is not as simple as it seemed. In a small window of temperature near the transition, at least three reactions could happen at the same time, depending on humidity level. In other solid acids, if there is a dehydration involved, it will be that of the solid acid itself and the compound will transform to a liquid [7, 12-14]. If there is a decomposition or a disproportionation, the products will be salts or other solid acids as in the $Rb_3H(SO_4)_2$ system [7, 13]. This $Cs_6(H_2SO_4)_3(H_{1.5}PO_4)_4$ compound illustrates the case that neither of the two statements above is true. The experimental results in Chapter 5 will show that

$Cs_6(H_2SO_4)_3(H_{1.5}PO_4)_4$ can transform to its superprotonic phase and decompose to H_3PO_4 and another solid acid with a smaller unit cell, and H_3PO_4 can dehydrate all in a small temperature range.

1.4 References

[1] W. Munch, K.D. Kreuer, U. Traub, J. Maier, *Solid State Ionics* **77** (1995) 10.

[2] D.A. Boysen, Superprotonic Solid Acids: Structure, Properties. and Applications, *Materials Science*, California Institute of Technology, Pasadena, California (2004).

[3] A.I. Baranov, V.V. Dolbinina, E.D. Yakushkin, V.Y. Vinnichenko, V.H. Schmidt, S. Lanceros-Mendez, *Ferroelectrics* **217** (1998) (1-4) 285.

[4] V.V. Sinitsyn, A. Baranov, E.G. Ponyatovsky, *Solid State Ionics* **136** (2000) 167.

[5] K. Suzuki, S. Hayashi, *Phys. Rev. B* **74** (2006) (13) 10.

[6] M. Polomska, L.F. Kirpichnikova, T. Pawlowski, B. Hilczer, *Ferroelectrics* **290** (2003) 51.

[7] L.A. Cowan, R.M. Morcos, N. Hatada, A. Navrotsky, S.M. Haile, *Solid State Ionics* **179** (2008) (9-10) 305.

[8] M. Sakashita, H. Fujihisa, K.I. Suzuki, S. Hayashi, K. Honda, *Solid State Ionics* **178** (2007) (21-22) 1262.

[9] A. Ikeda, Superprotonic solid acids : thermochemistry, structure, and conductivity, *Materials Science*, California Institute of Technology, Pasadena, California (2013).

[10] M.W. Louie, M. Kislitsyn, K. Bhattacharya, S.M. Haile, *Solid State Ionics* **181** (2010) (3-4) 173.

[11] C.R.I. Chisholm, Superprotonic Phase Transitions in Solid Acids: Parameters affecting the presence and stability of superprotonic transitions in the MHnXO4 family of compounds (X=S, Se, P, As; M=Li, Na, K, NH4, Rb, Cs), *Materials Science*, California Institute of Technology, Pasadena, California (2003).

[12] A. Ikeda, S.M. Haile, *Solid State Ionics* **213** (2012) 63.

[13] C. Panithipongwut, S.M. Haile, *Solid State Ionics* **213** (2012) 53.

[14] Y.K. Taninouchi, T. Uda, Y. Awakura, A. Ikeda, S.M. Haile, *J. Mater. Chem.* **17** (2007) (30) 3182.

Chapter 2 Experimental Methods

2.1 Synthesis

Polycrystalline and single crystal samples of the solid acids studied were synthesized by various aqueous-solution-based methods including solvent-induced precipitation, also known as rapid precipitation and forced precipitation; thermal-induced precipitation, also called agitated evaporation; and crystallization, so-called slow evaporation. Each solution contained carbonate or sulfate compounds of the metal studied and acids of interest with a specific ratio.

Polycrystalline samples were vacuum-filtered and rinsed with an appropriate organic solvent, usually methanol or acetone, to remove residual solutions containing ions and acids. These samples were then let dry in a drying oven or at ambient air before further measurements were taken.

Single crystal samples were individually removed from their mother liquors and rinsed very quickly with deionized water to remove residual liquid without forming fine particles of other solid acids on the surface of the crystals. To be able to do this without losing the crystals, the crystals must be large enough and the rinsing must be very quick. The crystals were then patted dry with Kimwipe.

In general, the crystallization method is suitable for samples that require high purity, while precipitation method is more suitable for incorporation of another ions into a structure. Anyway, for simple solid acids such as $CsHSO_4$, CsH_2PO_4, or $Rb_3H(SO_4)_2$, that are likely to be both thermodynamically and kinetically stable, the forced-precipitation method will be the first choice to try as it is fast and the product is still a pure phase. However, this is not always true, for example, $RbHSO_4$ cannot be obtained as

a pure phase from the solvent-induced precipitation method in which case it is necessary to let single crystals of $RbHSO_4$ grow from the solution. For larger solid acids which requires many ions in the solution to form the correct stoichiometry, the crystallization method is the better choice since forced-precipitations will make other kinetically stable compounds to form with the desired product due to the differences in local concentrations of multiple ions. Specific details and appropriate methods for each solid acid system are described in the respective chapter.

2.2 X-Ray Diffraction (XRD)

After the synthesis, the phase of each sample was identified using X-ray diffraction to confirm its purity at room temperature before further examinations. Consider Bragg's law:

$$2d \sin\theta = n\lambda \quad (1)$$

where d is the interplanar distance or the d-spacing, θ is the angle between the normal vector of the incident beam and the plane, λ is the X-ray wavelength, and n is the order of reflection which is always taken as 1 since the higher order can be represented by first order of reflections of planes with higher indices. Since every crystalline material has a different crystal structure and lattice parameters, it will give a unique set of reflections. By combining the diffraction data with chemical information, the sample can be easily identify especially for the known compounds in which case, one can either simply compare the pattern with a published one to just confirm the phase or perform Rietveld refinement for more structural information. For a new compound, *ab initio* determination

can be employed using diffraction data analysis software to determine the plausible unit cells along with related information.

For solid solution systems, XRD was used to determine the solubility limits. As an alien ion dissolves into a structure, the lattice parameter changes due to the difference in ionic radii of the original ion and the substituent. This will cause shifts in peak positions, which follow the Bragg's law until the solubility limit is reached. Beyond the solubility limit, the peaks will no longer move and another set of peaks from another phase will start showing up in the pattern. The raise of the other set of peaks might be difficult to be detected and if higher accuracy is needed, one may calculate the lattice parameters from the XRD patterns below and above the solubility limit, plot them against the composition, extrapolate the straight lines and find the intercept which in theory will represent the solubility limit.

In high-temperature studies, when there is no transition occurs, the shifts in peak positions are expected because of thermal expansions of materials that change the interplanar distance. Almost all of solid acids show regular thermal expansion behavior, i.e. the structure expands with the temperature, except one solid acid discovered so far, $Cs_6(H_2SO_4)_3(H_{1.5}PO_4)_4$, that shows an apparent negative thermal expansion behavior. Temperature dependence of lattice constants can be determined using either Rietveld method for a known structure. For a new phase, *ab initio* method will give the unit cell information such as plausible space groups as well as lattice constants associating with the space groups. At a polymorphic phase transition, a solid acid adopts another crystal structure, which could be a different or the same crystal system, but a different space group, and will usually give a different XRD pattern. Hence, this technique can be used

to estimate the transition temperature, but, in practice, it might not give a very accurate temperature due to operational limitations.

As mentioned above, we rely on peak positions to determine lattice parameters, space groups, and other cell information. Thus, correctness of peak positions is crucial. For a solid acid experiment with a regular size and thickness on an X-ray diffractometer that is well aligned, sample displacement is the source of error that occurs easily and is often found when a sample preparation for XRD is not done properly. The error from sample displacement can be corrected using internal standard addition method where a standard of known peak positions is added and mixed with the sample, then figure out the relationship between the shift in the peak positions of the standard and the observed positions and use the relationship to correct the peak positions of the sample. This method works fine as long as the standard does not react with the sample and its pattern does not interfere with the pattern of the sample. However, for a powder sample, it is relatively very easy to prepare the sample such that it is at the correct position, leading to the correct peak positions in the XRD pattern without the use of an internal standard and more analysis. Plus, the internal standard may not be applicable in some situations, such as when the peaks of the standard overlap with those of the sample. In this thesis, the sample displacement error was avoided successfully by careful sample preparations for the XRD experiments to ensure that the surfaces of the samples were at the right position.

Rietveld refinement is a method that is used to refine a structure using a set of initial parameters from a known structure to calculate diffraction patterns until a set of refined parameters giving the best fit between the calculated and the measured patterns is found.

Philips X'Pert Pro diffractometer with Cu Kα radiation was utilized to obtain X-ray diffraction data. Unless otherwise noted, the 2θ range was from 10 to 60° with a step size of 0.0167° for a total time of about 20 minutes for each measurement at both ambient and high temperatures.

The in situ high-temperature XRD data were collected using Anton Paar HTK1200 high-temperature chamber equipped to the diffractometer under flowing humidified helium (pH_2O ~ 0.023 atm) to prevent dehydration of the solid acids. Prior to data collection, powder samples were compacted into 15-mm-diameter pellets using ~ 194-MPa uniaxial pressure for 15 minutes to facilitate solid-state interdiffusion and phase equilibration. The measurement temperatures were reached at a ramp rate of 5 °C/min and the samples were allowed to reach equilibrium at each temperature as no changes in the diffraction patterns were observed.

Rietveld refinements and cell determinations were performed using X'Pert Plus software.

2.3 A.C. Impedance Spectroscopy (ACIS)

The conductivities of the solid acids were obtained using A.C. impedance spectroscopy. In this technique, alternating voltages, $V(t) = V_0 \cdot exp(i\omega t)$, at various angular frequencies, ω, where V_0 is the amplitude of the applied voltage, t is the time, and $i = \sqrt{-1}$, are applied to the material and corresponding alternating currents, $I(t) = I_0 \cdot exp(i\omega t+\theta)$, where I_0 is the amplitude of the current and θ is the phase difference between $V(t)$ and $I(t)$, are measured. Impedances, $Z(\omega)$, are then calculated from the equation:

$$Z(\omega) = \frac{V(t)}{I(t)} \tag{2}$$

The impedances can be written as

$$Z(\omega) = |Z|\cos\theta - i\,|Z|\sin\theta = Z_R - iZ_I \tag{3}$$

where $|Z|$ is the magnitude of the impedance, $Z_R = |Z|\cos\theta$ is the real, and $Z_R = |Z|\sin\theta$ is the imaginary parts of the impedance. A plot of $-Z_I$ against Z_R is called a Nyquist plot. For electrochemical processes with different characteristic frequencies, a separate arc along the x-axis will represent each process and the width of the arc on the real axis will represent the respective resistance. Figure 2.1 shows a schematic Nyquist plot for a material with resistances from three common contributions: bulk, grain boundary, and electrode. In this study, there are usually two arcs from the bulk and the electrode observed at low temperatures and only a straight line representing the electrode contribution is observed above the superprotonic transition as shown in Figure 2.2 a and b. The dotted lines in Figure 2.2 are theoretical arcs that are not detected due to the limited frequency range of the impedance analyzer.

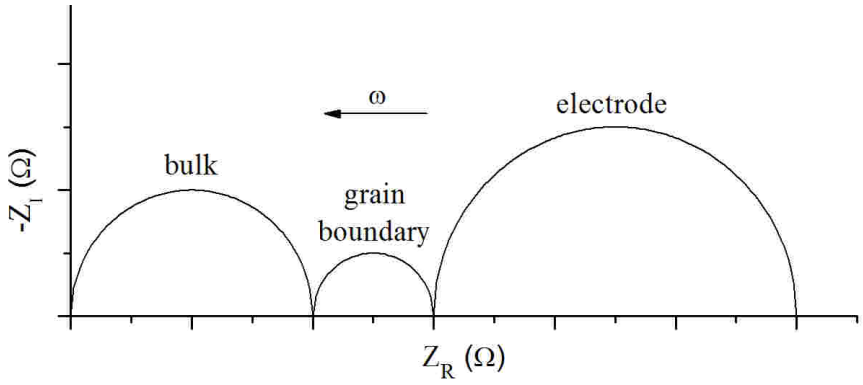

Figure 2.1. Schematic Nyquist plot of a material with contributions from bulk, grain boundary, and electrode resistances.

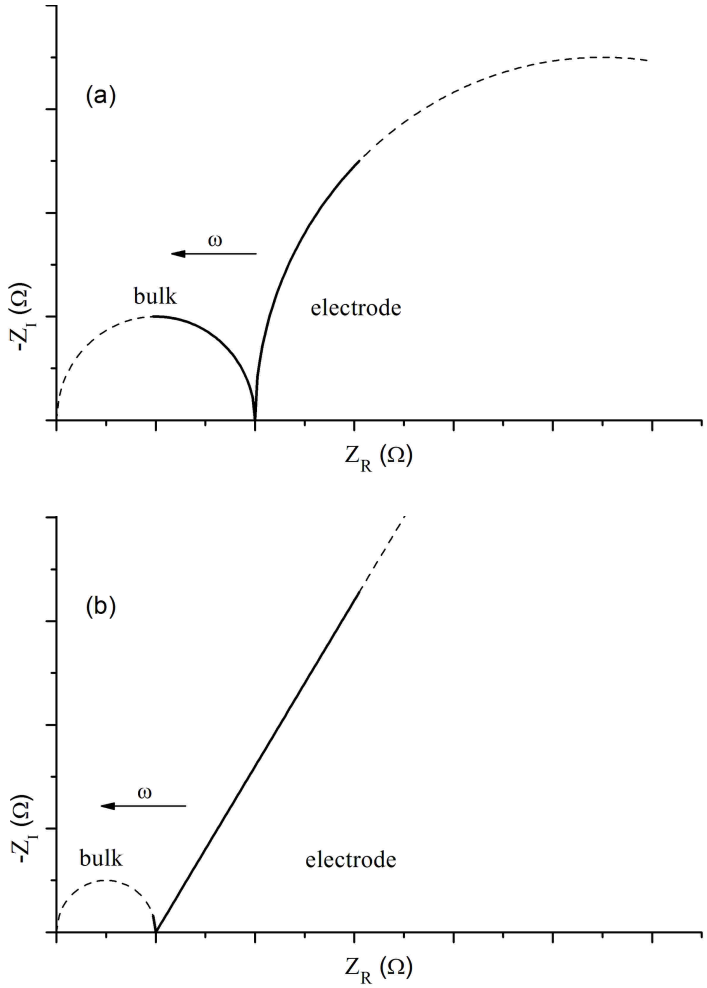

Figure 2.2. Schematic Nyquist plot of solid acids (a) below and (b) above the superprotonic transition. The dotted lines are theoretical arcs that are not detected due to the limited frequency range of the impedance analyzer.

Since the x-intercept here is the same as the width of the arc of the bulk resistance, as seen in Figure 2.2, measuring the impedance just at the intercept is essentially the same as fitting the arc to obtain the width. By simply selecting a frequency that gives such data point, this mode of measurement is called single-frequency mode, which measures the impedance of only one point instead of the full frequency range allowing faster and continuous data collection, i.e. a few seconds as opposed to 1-2 minutes for a full-range spectrum. The single-frequency mode also reduces the complications occurring during fittings of the spectra near the superprotonic transition

since the full spectra might be changing during the measurements resulting in distorted, poorly defined arcs.

Conductivity measurements were performed on 9.3-mm-diameter pellet samples, prepared under 15 min of uniaxial pressure (~ 216 MPa). PELCO Colloidal silver paste (Ted Pella, #16032) was applied to opposing sides to serve as electrodes. Data were collected using a HP 4284 precision LCR meter.

Most of the measurements were performed under active humidification, with pH_2O ~ 0.02-0.03 atm attained by passing the inlet N_2 through a room-temperature bubbler. Only in the case of some samples, such as $RbHSO_4$, which were found to be particularly sensitive to dehydration, the pH_2O was increased to 0.5 atm. Some measurements were carried out under ambient and dry atmospheres to study the effect of humidity.

The temperature ranges of measurements were from a temperature as low as 25 °C under ambient humidity or 60 °C under humidified gas to a maximum temperature slightly above the transition temperatures of the solid acids. The samples were held at the starting temperatures for at least 30 minutes prior to data collection, and the ramp rate was 0.1-1 °C/min.

After a set of preliminary full spectrum measurements (20 Hz to 1 MHz), a frequency at which the imaginary component of the impedance was at minimum was selected as appropriate for capturing bulk phase transformation behavior in single-frequency measurements. Because only a single frequency was examined, the data could be recorded continuously under constant heating and cooling rates.

2.4 Differential Scanning Calorimetry (DSC)

In DSC technique, the difference in the amount of heat needed to keep the temperatures of a sample and a reference equal is measured as a function of temperature. At a transition, for instance, a phase transition or a disproportionation, an amount of heat is absorbed due to the latent heat of the process, so an additional amount of heat is required to compensate and keep the temperatures of the material and the reference equal.

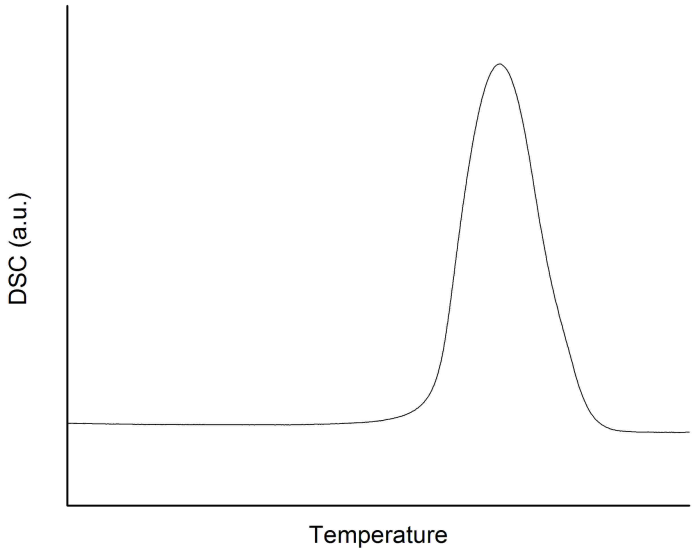

Figure 2.3. Schematic DSC profile.

Figure 2.3 shows a schematic DSC profile. An integrated peak area can be calibrated using a set of standard materials to correlate to an amount of heat and this connection can be used to calculate the heat from a peak area of a sample.

A Netzsch STA 449 simultaneous DSC/TG instrument was employed to study thermal behavior of the samples. Each sample was compacted to a 5.25-mm-diameter pellet under a pressure of ~ 226 MPa for 5 minutes to facilitate solid-state interdiffusion. The pellet samples were examined under either dry or flowing humidified nitrogen gas

with various pH_2O up to ~ 0.023 atm in the temperature ranges similar to those in ACIS experiments.

2.5 Energy-Dispersive X-Ray Spectroscopy (EDS)

When excited with certain energy, an atom can release a set of X-rays with characteristic energies, which is unique for each element. This technique uses these characteristic spectra to identify the elemental composition of the sample.

Energy-dispersive X-ray spectroscopy was performed on solid solution samples and $Cs_6(H_2SO_4)_3(H_{1.5}PO_4)_4$ to determine the actual compositions at room temperature using Oxford X-Max SDD X-ray Energy Dispersive Spectrometer. The powder samples were pressed into pellets and polished so that the surfaces of the samples were flat and suitable for EDS measurements. For each sample, at least eight EDS data were collected and the atomic percentages of the elements in the materials were used to determine the actual compositions.

Chapter 3 $Rb_3H(SO_4)_2$-$RbHSO_4$ Pseudo-Binary System

Adapted with permission from: C. Panithipongwut, S.M. Haile. High-temperature phase behavior in the $Rb_3H(SO_4)_2$-$RbHSO_4$ pseudo-binary system and the new compound $Rb_5H_3(SO_4)_4$. *Solid State Ionics* **213** (2012) 53.

3.1 Introduction: Absence of Polymorphic Transition of $Rb_3H(SO_4)_2$

Several solid acid compounds, materials formed of oxyanion groups linked by hydrogen bonds, are known to undergo superprotonic phase transitions at elevated temperatures (~ 100 – 300 °C). At the transition, the materials transform from their respective low-symmetry, low-conductivity phases to high-symmetry, high-conductivity phases. The family of solid acid compounds with stoichiometry $M_3H(XO_4)_2$, where M = NH_4, K, Rb, Cs; X = S, Se, typifies this behavior. Many within this family display a transformation from a room-temperature monoclinic phase to a high-temperature trigonal phase (symmetry $R\bar{3}m$, phase I). The increase in conductivity at the transition is generally 3-4 orders of magnitude. The compound $Rb_3H(SO_4)_2$ is unusual in that, despite being isostructural at room temperature to others in the family, the increase in conductivity on heating under ambient pressures is a result of disproportionation rather than a polymorphic transition. [1] That is, whereas a high-temperature trigonal phase occurs for $Rb_3H(SeO_4)_2$, $Cs_3H(SeO_4)_2$, $(NH_4)_3H(SeO_4)_2$ and $(NH_4)_3H(SO_4)_2$, $Rb_3H(SO_4)_2$ decomposes at ~ 210 °C into Rb_2SO_4 and an unknown phase of generic stoichiometry $Rb_mH_n(SO_4)_p$, with $p=(m+n)/2$.[1] Stabilization of the trigonal phase requires pressures in excess of 0.14 GPa and temperatures in excess of 228 °C. [2, 3] A remarkable attribute of the two-phase mixture that results from $Rb_3H(SO_4)_2$ is a sharp increase in conductivity

(by about 2 orders in magnitude) concomitant with the disproportionation reaction, giving the impression of a polymorphic superprotonic transition. [1, 2] Indeed, the two-phase mixture has been referred to as phase IV in the literature as a result of some misinterpretation of the nature of the phase change. [2]

This work was carried out with the objective of fully elucidating the high-temperature behavior of $Rb_3H(SO_4)_2$. Cowan *et al*. demonstrated that the unknown phase $Rb_mH_n(SO_4)_p$ must be an intermediate between $RbHSO_4$ and $Rb_3H(SO_4)_2$ and suggested the composition $Rb_5H_3(SO_4)_4$. [1] A preliminary evaluation of the phase behavior in the Rb_2SO_4-$RbHSO_4$ system was further provided in that study. Here, we carry out a systematic characterization of phase behavior in the narrower composition range between $Rb_3H(SO_4)_2$ and $RbHSO_4$ using a combination of A.C. impedance spectroscopy, high-temperature X-ray powder diffraction, and differential scanning calorimetry.

3.2 Synthesis and Characterizations

3.2.1 Sample preparation

The compositions examined are shown in Figure 3.1 as points along the abscissa of the schematic pseudo-binary phase diagram for the Rb_2SO_4-H_2SO_4 system proposed by Cowan et al. [1] Because the compositions of interest for the present work lie within the range of $Rb_3H(SO_4)_2$ and $RbHSO_4$, they are hereafter referred to in terms of mole % of $RbHSO_4$ in the overall system. Samples of (1-x) $Rb_3H(SO_4)_2$ – x $RbHSO_4$ were prepared simply from solid-state mixtures of the two end members, where the end members were prepared from aqueous solutions of rubidium sulfate (Rb_2SO_4, Alfa Aesar 99%) and sulfuric acid (H_2SO_4, EMD Chemicals 95-98%).

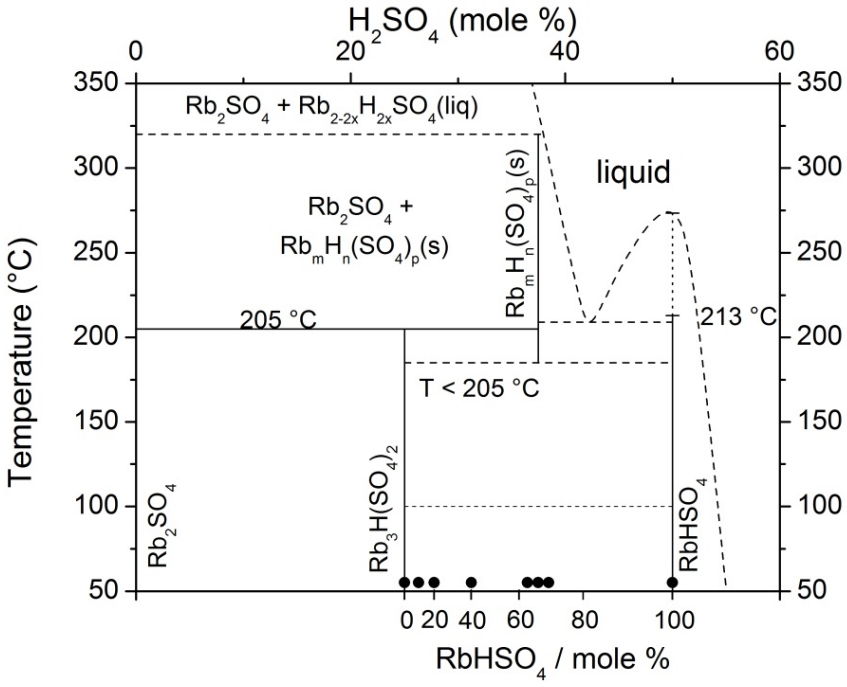

Figure 3.1. Proposed phase diagram in the Rb_2SO_4-H_2SO_4 system after Cowan et al. [1]; compositions within the $R_3H(SO_4)_2$-$RbHSO_4$ region examined in this work as indicated.

The trirubidium compound, $Rb_3H(SO_4)_2$, was obtained using a solution in which the Rb:H molar ratio was fixed at 3:1. Introduction of methanol to the solution induced rapid precipitation of the target compound. The product was filtered, rinsed with methanol, and finally dried in an oven at ~ 100 °C for 24 hours or more prior to further experimentation. In contrast, rubidium hydrogen sulfate was synthesized in single crystal form. In principle, the stoichiometry $RbHSO_4$ dictates a molar ratio of Rb:H of 1:1, however, it was found that excess sulfuric acid was necessary to obtain the target material as the sole product. Solutions were prepared in a 1:2 molar ratio of Rb:H, and slow evaporation of water over about 4 days under ambient conditions eventually yielded moderately sized crystals (~ 0.3 cm × 1 cm). These were removed from the mother liquor and quickly rinsed with deionized water to eliminate excess sulfuric acid. After an

additional rinse with acetone, they were dried overnight in a drying oven at ~ 100 °C. Solid mixtures of $Rb_3H(SO_4)_2$ and $RbHSO_4$ were prepared by combining and grinding in a mortar and pestle appropriate amounts of polycrystalline $Rb_3H(SO_4)_2$ and $RbHSO_4$ for approximately 10 minutes.

3.2.2 X-ray diffraction (XRD)

X-ray powder diffraction was performed for phase identification at both ambient and high temperatures using a Phillips X'Pert Pro diffractometer with Cu Kα radiation. Diffraction data were collected in the 2θ range from 10 to 60° with a step size of 0.0167°. The dwell time for each detector position, which covers several steps, was 50.165 s for a total measurement time for each sample or condition of 20:34 min. An Anton Paar HTK1200 oven, supplied with humidified helium (pH_2O ~ 0.032 atm), was employed to acquire high-temperature data.

High-temperature measurements were focused on $Rb_3H(SO_4)_2$ and on 66.67% $RbHSO_4$, the latter corresponding to the proposed compound $Rb_5H_3(SO_4)_4$. To facilitate solid-state interdiffusion and phase equilibration, samples were formed into 15-mm-diameter compacts using ~ 194 MPa uniaxial pressure for 15 min prior to data collection. In the case of the 66.67% $RbHSO_4$ sample, data were collected at 160, 180, 190, and 200 °C sequentially. After reaching the highest temperature, the furnace was cooled and data collected at 160 and 150 °C and room temperature. The temperature ramp rate was 5 °C/min, and at each measurement temperature samples were equilibrated, as indicated by the absence of changes in the diffraction patterns.

3.2.3 A.C. impedance spectroscopy (ACIS)

Conductivity measurements were performed using 9.3-mm-diameter pellet samples, again prepared under 15 min of uniaxial pressure (~ 216 MPa). PELCO Colloidal silver paste (Ted Pella, #16032) was applied to opposing sides to serve as electrodes. Data were collected using a HP 4284 precision LCR meter. After a set of preliminary full spectrum measurements (20 Hz to 1 MHz), a frequency of 45 kHz was selected as appropriate for capturing bulk phase transformation behavior. Specifically, the maximum contribution from the imaginary component to the total impedance was only 5% at 45 kHz and decreased with increasing temperature to essentially zero at the highest temperature in the experiment. The measurements were performed under active humidification, with pH_2O = 0.032 atm attained by passing the inlet N_2 through a room-temperature bubbler. Only in the case of the end-member $RbHSO_4$, which was found to be particularly sensitive to dehydration, the pH_2O was increased to 0.5 atm. The temperature range of measurement was from 140 to 220 °C, except for samples with 10-20% and pure $RbHSO_4$, for which the range was 160 to 212 °C. The samples were held at the starting temperatures for at least 30 minutes prior to data collection, and the ramp rate was 0.1-1 °C/min. Because only a single frequency was examined, the data were recorded continuously under constant heating.

3.2.4 Thermal analysis

Thermal behavior of the 66.67% $RbHSO_4$ material was examined using a Netzsch STA 449. A compact 61.141 mg in mass, 5.25 mm in diameter was formed, using 226-MPa pressure for 5 minutes, in order again to facilitate solid-state reaction. The

measurement was carried out under humidified nitrogen (pH_2O ~ 0.032 atm). Prior to data collection, the sample was held at 150 °C for 6 hours (in the STA). Data were then collected on heating to 210 °C, and then over three additional thermal cycles in the temperature range from 30 to 210 °C, in all cases using a ramp rate of 2 °C/min.

3.3 Conductivity Studies

The conductivities so measured of $Rb_3H(SO_4)_2$, $RbHSO_4$, and selected mixed compositions are shown in Figure 3.2. The most striking feature of these results is the occurrence of multiple, sharp increases in conductivity at various temperatures, with the specific behavior strongly dependent on composition. In the case of $Rb_3H(SO_4)_2$, in agreement with the results reported earlier by Cowan et al. [1], Sinitsyn et al. [2], and Baranov et al. [4], a single, dramatic increase in conductivity, from 3.6×10^{-5} to 2.0×10^{-3} S/cm, occurs at ~ 201 °C. On cooling, the high-conductivity state is maintained to a temperature of ~ 180 °C.

Upon introduction of up to 66.67% $RbHSO_4$ into mixtures with $Rb_3H(SO_4)_2$, three features are observed: a new conductivity anomaly appears at 185 °C; with increasing $RbHSO_4$ content the magnitude of the conductivity change at 205 °C decreases; and the low-temperature conductivity generally increases. At compositions beyond 66.67% $RbHSO_4$, as exemplified by the composition with 70% $RbHSO_4$, the anomaly at 185 °C is retained, and, in addition, a new anomaly at 168 °C appears. In the case of 100% $RbHSO_4$, a small, broad anomaly occurs at 168 °C, followed by what appears to be a very broad solid to liquid transformation at 205 °C. Upon removal from the test station, unlike any of the other compositions, the sample of neat $RbHSO_4$ was mechanically deformed

and displayed a glossy sheen. These characteristics are indicative of the presence of a liquid phase at the highest temperatures examined. It is known that in the case of CsH_2PO_4, for example, partial dehydration can yield a liquid phase [5, 6] and it appears that $RbHSO_4$ may display similar behavior. For this reason, the high $RbHSO_4$ region of the phase diagram has not been fully studied here.

The most significant aspect of the results depicted in Figure 3.2 is the absence of a conductivity anomaly at 205 °C for the 66.67% $RbHSO_4$ composition. The conductivity of this composition at temperatures below 205 °C is moreover much higher than that of either of the end members $Rb_3H(SO_4)_2$ and $RbHSO_4$. This combination of factors suggests that the unknown product of the disproportionation of $Rb_3H(SO_4)_2$ at 205 °C indeed has composition 66.67% $RbHSO_4$ as originally speculated [1] and, furthermore, that the stability of this compound extends to temperatures below 140 °C. That is, the conductivity data suggest that the new compound $Rb_5H_3(SO_4)_2$, corresponding to 66.67% $RbHSO_4$, is both thermodynamically stable and kinetically accessible at temperatures as low as 140 °C.

(a)

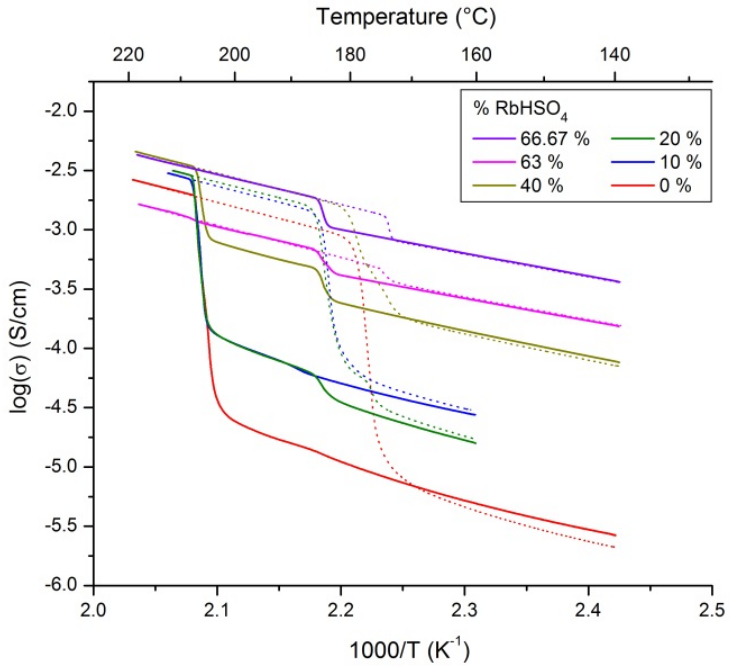

(b)

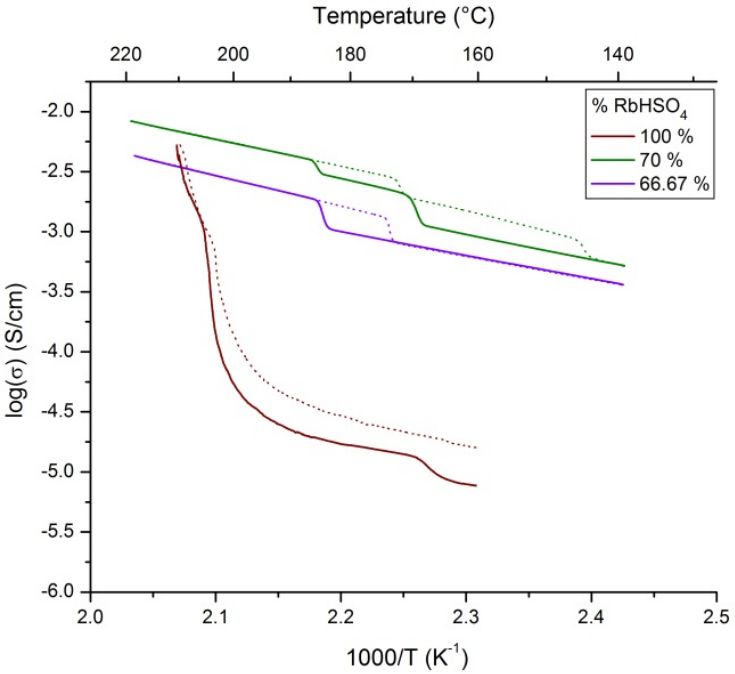

Figure 3.2. Conductivity of compositions in the $Rb_3H(SO_4)_2$-$RbHSO_4$ system upon heating under humidified nitrogen (pH_2O ~ 0.032 atm) at a ramp rate of 0.1 °C/min: (a) 0-66.67% $RbHSO_4$; and (b) 66.67-100% $RbHSO_4$.

3.4 High-Temperature XRD and Rietveld Refinement of LT-$Rb_5H_3(SO_4)_4$

The circumstantial evidence for the existence of $Rb_5H_3(SO_4)_4$ as a new, stable compound provided by the conductivity measurements is supported unequivocally by the diffraction (Figures 3.3 and 3.4).

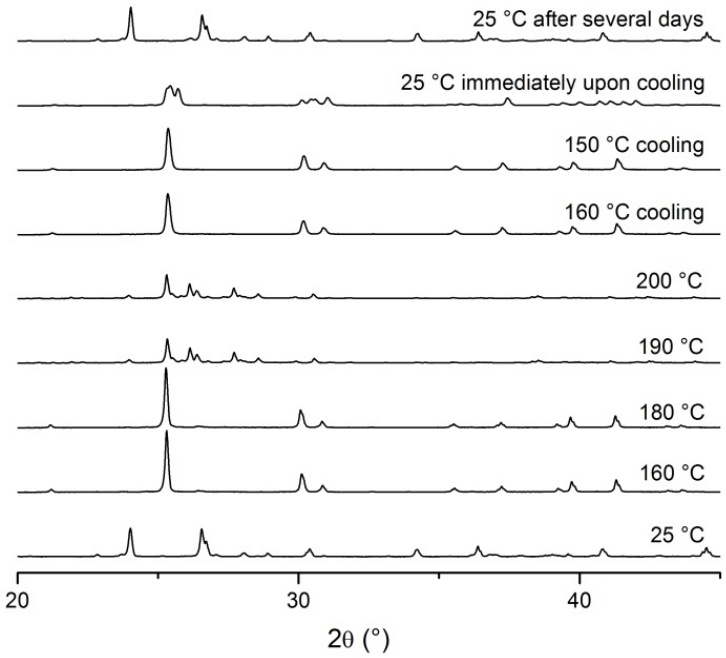

Figure 3.3. Equilibrium high-temperature XRD patterns of the 66.67%-$RbHSO_4$ content composition at indicated temperatures, under humidified helium ($pH_2O \sim 0.032$ atm).

At room temperature the 66.67% $RbHSO_4$ composition displays the diffraction pattern of a mixture of the two end-member compounds $Rb_3H(SO_4)_2$ and $RbHSO_4$, indicating the absence of reactions under ambient conditions. At 160 °C, however, as shown clearly in Figure 3.4a, an entirely different pattern emerges. These diffraction data can be described according to a structure recently reported for a high-temperature form of $Cs_5H_3(SO_4)_4$ with space group $P\bar{3}m$ [7], along with minor peaks due to residual

$Rb_3H(SO_4)_2$ and $RHSO_4$. Specifically, Rietveld refinement using as an initial starting model the atomic coordinates of $Cs_5H_3(SO_4)_4$ and *ab initio* determined cell constants yielded the following: a = 5.9298(2) Å, c = 14.4736(6) Å, cell volume V = 440.74(3) $Å^3$, and the atomic parameters listed in Table 3.1. With Z =1, the computed density is 3.0691(2) Mg/m^3. The asymmetric unit contains three crystallographically distinct Rb atoms and two distinct sulfate groups. The oxygen atoms about S(2) have low occupancy, as reported by [7], and the coordinates listed in Table 3.1 for these oxygen species have not been refined from their initial values. Likewise, the isotropic displacement parameters (for all species) have not been refined. The final refinement parameters are R_{wp} = 7.64%, R_{Bragg} = 2.97%, and GOF = 9.35. The rotational disorder associated with the S(2) sulfate group appears responsible for the high conductivity of this phase (Figure 3.2).

Table 3.1. Atomic coordinates, occupancies, and isotropic displacement parameters in $Rb_5H_3(SO_4)_4$ at 160 °C, refined in space group $P\bar{3}m$ with a = 5.9298(2) Å and c = 14.4736(6) Å.

Atom	Site	Occupancy	x	y	z	B (10^4 pm^2)
Rb(1)	1b	1.0000	0.0000	0.0000	0.5000	0.0900
Rb(2)	2d	1.0000	0.6667	0.3333	0.0621(3)	0.0552
Rb(3)	2d	1.0000	0.3333	0.6667	0.2613(4)	0.0751
S(1)	2c	1.0000	0.0000	0.0000	0.1373(7)	0.0507
O(1)	2c	1.0000	0.0000	0.0000	0.249(1)	0.0633
O(2)	6i	1.0000	0.134(1)	0.866(1)	0.1065(7)	0.0633
S(2)	2d	1.0000	0.6667	0.3333	0.3686(6)	0.0760
O(3)	6i	0.3333	0.5532	0.2766	0.2785	0.0887
O(4)	6i	0.5000	0.5408	0.4592	0.4162	0.2533
O(5)	12j	0.2500	0.7385	0.1561	0.3658	0.2533

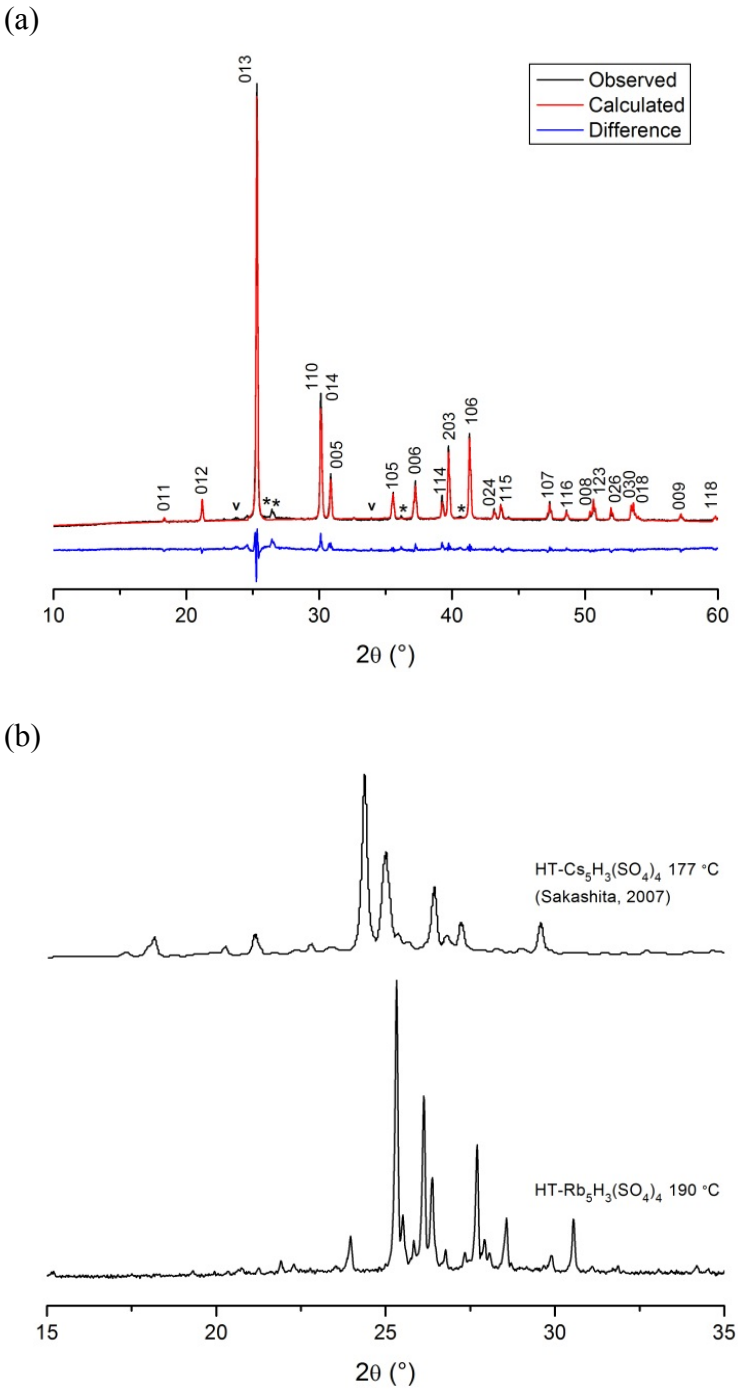

Figure 3.4. XRD patterns of the 66.67%-$RbHSO_4$ content composition under humidified helium (pH_2O ~ 0.032 atm) at (a) 160 °C and (b) 190 °C. The pattern in (a) is analyzed in terms of the reported intermediate-temperature (130 °C) structure of $Cs_5H_3(SO_4)_4$ [7], with a primitive trigonal cell, space group $P\bar{3}m$, and lattice constants a = 5.9298(2) Å and c = 14.4736(6) Å. Peaks marked with * and ᵛ are from residual $Rb_3H(SO_4)_2$ and $RbHSO_4$, respectively. The pattern in (b) is compared to that of a higher-temperature form of $Cs_5H_3(SO_4)_4$ [7].

At temperatures beyond 185 °C (specifically 190 and 200 °C), at which a conductivity anomaly is observed for almost all compositions (Figure 3.2), the diffraction pattern of the 66.67% $RbHSO_4$ composition changes yet again, Figures 3.3 and 3.4b. In a manner almost identical to the high-temperature behavior of $Cs_5H_3(SO_4)_4$ [7], heating, in this case, causes the pattern complexity to increase, suggesting either a reduction in symmetry or a further disproportionation. As possible disproportionation products, Rb_2SO_4 and $RbHSO_4$ are ruled out simply by the features of diffraction patterns (though not shown, major peaks due to the phases are absent). An overall composition change due to dehydration is unlikely due to the reversibility of the transformation. Specifically, on cooling, the trigonal pattern is recovered, as shown, for example, by the pattern at 160 °C. Even at room temperature, the material eventually returns to being a mixture of $RbHSO_4$ and $Rb_3H(SO_4)_2$, as shown in the final diffraction pattern collected after several days at ambient conditions. Dehydration is further ruled out because the transition temperature was found to be independent of water partial pressure (data not shown). As shown in Figure 3.2, the transformation is associated with a moderate but clear (about 3 times) increase in conductivity. This behavior, along with the general features of the inferred phase diagram (discussed further below), suggests a polymorphic transformation rather than disproportionation. Accordingly, $Rb_5H_3(SO_4)_4$ is tentatively assigned two phases, a lower-temperature trigonal form, LT-$Rb_5H_3(SO_4)_4$ (below 185 °C) and an unindexed, higher-temperature form, HT-$Rb_5H_3(SO_4)_4$ (above 185 °C). The overall similarity to the behavior of $Cs_5H_3(SO_4)_4$ [7] is noteworthy.

3.5 DSC Studies

The thermal behavior of the 66.67% $RbHSO_4$ composition is shown in Figure 3.5. Based on the diffraction data, the 6-hour anneal at 150 °C (prior to the first cycle) was implemented with the objective of generating single phase $Rb_5H_3(SO_4)_4$.

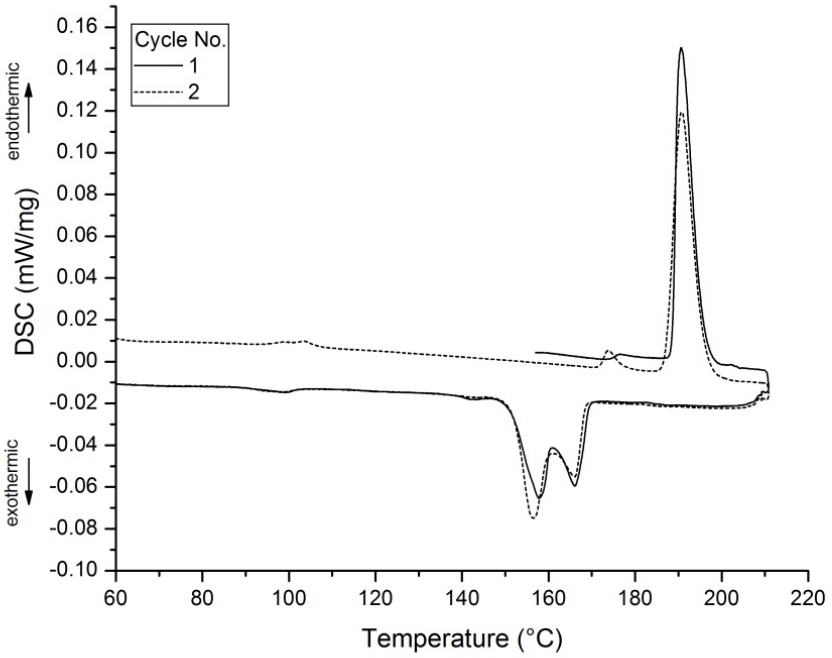

Figure 3.5. DSC profiles of the 66.67% $RbHSO_4$ sample under humidified nitrogen (pH_2O ~ 0.032 atm) at a ramp rate of 2 °C/min. First and second cycles.

On heating after this treatment, a large endothermic event with a heat of transformation of 23.8 kJ/mol and an onset temperature of 185 °C is evident, clearly corresponding to the transformation between the LT and HT forms of $Rb_5H_3(SO_4)_4$, already diagnosed by conductivity and X-ray powder diffraction. This transformation enthalpy is smaller, but still close to that reported for the apparently analogous transition in $Cs_5H_3(SO_4)_4$ (26.4 – 29.9 kJ/mol). [8] Given the somewhat preliminary evaluation of both materials, it would be premature to attribute this discrepancy to distinct phase

behaviors. Both values can be considered typical of superprotonic transitions heat of transformation. Specifically, compounds in the $MHSO_4$ family display heats of transformation of ~ 5.5-10.5 kJ/mol [9-11], whereas those in the $M_3H(SO_4)_2$ family, for which the structural difference between the two phases is small, have values of ~ 4 kJ/mol. [12, 13] The simple molar weighted sum is then ~ 15-25 kJ/mol for a compound in the $M_5H_3(SO_4)_4$ family. On cooling, the reverse transformation occurs by a two-step process, with exothermic peaks centered at approximately 170 and 155 °C. The reasons for the two-step behavior are unknown. On further cooling, a very weak, broad thermal event is observed at ~ 100 °C, which may be associated with the partial disproportionation of $Rb_5H_3(SO_4)_4$ back into $Rb_3H(SO_4)_2$ and $RbHSO_4$, or possibly water condensation. The subsequent thermal cycle shows on heating a weak endothermic event at 100 °C, and a new, but also weak, exothermic event at 170 °C. Based on the conductivity data, no transformation is expected for the 66.67% $RbHSO_4$ composition at this latter temperature. However, for $RbHSO_4$-rich compositions, a conductivity anomaly is clearly observed at 168 °C. Thus, the occurrence of a DSC peak at 170 °C for the 66.67% $RbHSO_4$ composition may reflect the presence of $RbHSO_4$ that is formed on cooling to ambient temperatures (and is not fully consumed to form single phase $Rb_5H_3(SO_4)_4$ on the subsequent heating). The slight decrease in the magnitude of the thermal event at 185 °C from the first to subsequent cycle is consistent with this interpretation.

3.6 Phase Diagram of Rb_2SO_4-H_2SO_4 System

The combination of conductivity, diffraction and thermal data collected here enable construction of the modified phase diagram for the Rb_2SO_4-rich end of the Rb_2SO_4-H_2SO_4 system presented in Figure 3.6.

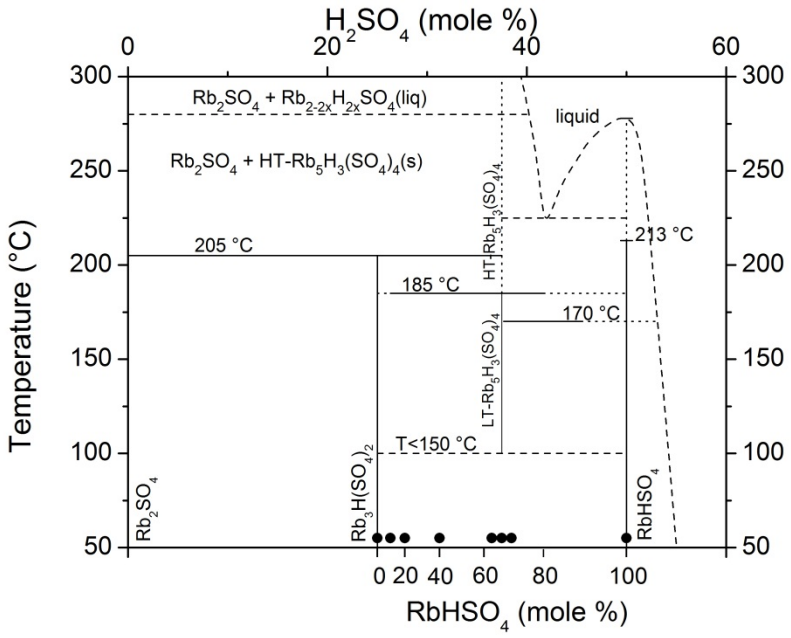

Figure 3.6. Revised phase diagram for the pseudo-binary Rb_2SO_4-H_2SO_4 system, constructed on the basis of the previously proposed diagram of Cowan et al. [1] and new findings in this work.

Here, the conductivity anomaly occurring at 205 °C for all compositions in the $Rb_3H(SO_4)_2$-$RbHSO_4$ mixtures with $RbHSO_4$ content less than 66.67 % is attributed to the disproportionation of $Rb_3H(SO_4)_2$ into Rb_2SO_4 and the new phase identified as $Rb_5H_3(SO_4)_4$. At the high temperature of the disproportionation reaction, $Rb_5H_3(SO_4)_4$ adopts what appears to be a high-temperature structure with a surprisingly complex diffraction pattern. The new compound $Rb_5H_3(SO_4)_4$ forms at temperatures at least as low

as 140 °C. Between 140 and 185 °C it adopts a trigonal structure, isomorphous to a known trigonal phase of $Cs_5H_3(SO_4)_4$ [7], and displays a relatively high conductivity. The conductivity anomaly observed at 185 °C for all compositions examined, with the exception of the two end members and the 10% $RbHSO_4$ content sample, is tentatively attributed to the polymorphic transformation of $Rb_5H_3(SO_4)_4$ from its lower temperature, trigonal form to a higher temperature, higher conductivity form.

The possibility that $Rb_5H_3(SO_4)_4$ itself undergoes a disproportionation reaction at 185 °C cannot be entirely ruled out; however, such behavior would appear to be contradictory to the results obtained. Specifically, disproportionation would require the formation of a $Rb_3H(SO_4)_2$-rich and a $RbHSO_4$-rich phase relative to $Rb_5H_3(SO_4)_4$. The $Rb_3H(SO_4)_2$-rich phase, existing somewhere between $Rb_3H(SO_4)_2$ and $Rb_5H_3(SO_4)_4$ would be required to undergo some sort of transition at 205 °C, coinciding with the confirmed disproportionation of $Rb_3H(SO_4)_2$. On the other hand, this transformation would simultaneously be required to be absent at compositions with $RbHSO_4$ content greater than 66.67% although such compositions would be expected to contain the new phase. This contradiction leads us to propose the polymorphic transformation. The fact that the 185 °C anomaly is absent for the 10% $RbHSO_4$ content sample is attributed to the small amount of $Rb_5H_3(SO_4)_4$ that would have formed at this composition (5.56 mol%). Turning to the compositions rich in $RbHSO_4$ relative to $Rb_5H_3(SO_4)_4$, Figure 3.2b, the conductivity anomaly occurring at 170 °C for all compositions with $RbHSO_4$ content greater than 66.67 % is tentatively attributed to a polymorphic transition in $RbHSO_4$. [14, 15] A surprising feature of this transition is its sharp appearance in the 70% $RbHSO_4$ content sample, which constitutes a mixture of 75 mol% $Rb_5H_3(SO_4)_4$ and only 25 mol%

$RbHSO_4$. The reason for this behavior is unclear. As noted above, measurements in the $RbHSO_4$-rich portion of the $Rb_3H(SO_4)_2$-$RbHSO_4$ system were limited due to the poor thermal stability of these compositions.

3.7 Conclusions

In combination, the results from conductivity measurements, high-temperature XRD, and DSC reveal the occurrence of a new phase in the Rb_2SO_4-H_2SO_4 system, specifically, $Rb_5H_3(SO_4)_4$. The compound is not stable at room temperature but can be formed from direct solid state reaction between $Rb_3H(SO_4)_2$ and $RbHSO_4$ at temperatures as low as 140 °C. At 160 °C, it adopts a structure with primitive trigonal lattice, space group $P\bar{3}m$, and lattice parameters a = 5.9298(2) Å and c = 14.4736(6) Å. At 185 °C, $Rb_5H_3(SO_4)_4$ undergoes what is proposed to be a polymorphic transition to a phase of somewhat higher conductivity but lower symmetry with a heat of transformation of 23.8 kJ/mol. The reverse transition occurs at ~170 °C, depending on the cooling rate. Under ambient temperatures, $Rb_5H_3(SO_4)_4$ slowly disproportionates over the course of several days to the two original compounds, $Rb_3H(SO_4)_2$ and $RbHSO_4$. The low and high temperature phases of $Rb_5H_3(SO_4)_4$ are isostructural with the intermediate and high temperature phases of $Cs_5H_3(SO_4)_4$ reported by Sakashita *et al.*[7], respectively.

3.8 References

[1] L.A. Cowan, R.M. Morcos, N. Hatada, A. Navrotsky, S.M. Haile, *Solid State Ionics* **179** (2008) (9-10) 305.

[2] V.V. Sinitsyn, A. Baranov, E.G. Ponyatovsky, *Solid State Ionics* **136** (2000) 167.

[3] H. Yamawaki, H. Fujihisa, M. Sakashita, K. Honda, Y. Gotoh, *Physica B* **405** (2010) (1) 291.

[4] A.I. Baranov, V.V. Dolbinina, E.D. Yakushkin, V.Y. Vinnichenko, V.H. Schmidt, S. Lanceros-Mendez, *Ferroelectrics* **217** (1998) (1-4) 285.

[5] Y. Taninouchi, T. Uda, Y. Awakura, *Solid State Ionics* **178** (2008) (31-32) 1648.

[6] Y.K. Taninouchi, T. Uda, Y. Awakura, A. Ikeda, S.M. Haile, *J. Mater. Chem.* **17** (2007) (30) 3182.

[7] M. Sakashita, H. Fujihisa, K.I. Suzuki, S. Hayashi, K. Honda, *Solid State Ionics* **178** (2007) (21-22) 1262.

[8] K.-i. Suzuki, S. Hayashi, *Phys. Rev. B* **73** (2006) (2) 024305.

[9] C.R.I. Chisholm, S.M. Haile, *Chemistry of Materials* **19** (2007) (2) 270.

[10] M. Friesel, B. Baranowski, A. Lunden, *Solid State Ionics* **35** (1989) (1-2) 85.

[11] S. Yokota, *J. Phys. Soc. Jpn.* **51** (1982) (6) 1884.

[12] A. Pawlowski, M. Polomska, B. Hilczer, L. Szczesniak, A. Pietraszko, *Journal of Power Sources* **173** (2007) (2) 781.

[13] A. Pawlowski, L. Szczesniak, M. Polomska, B. Hilczer, L. Kirpichnikova, *Solid State Ionics* **157** (2003) (1-4) 203.

[14] H. Feki, H. Khemakhem, Y. Abid, *J. Phys.-Condes. Matter* **13** (2001) (37) 8509.

[15] V.G. Ponomareva, G.V. Lavrova, *Solid State Ionics* **145** (2001) (1-4) 197.

Chapter 4 Phase Transition Behavior of $(Cs_xRb_{1-X})_3H(SeO_4)_2$ Solid Solutions

4.1 Introduction

Trirubidium hydrogen diselenate, $Rb_3H(SeO_4)_2$, and tricesium hydrogen diselenate, $Cs_3H(SeO_4)_2$, are solid acids in the $M_3H(XO_4)_2$ family where M=NH_4, K, Rb, Cs and X=S, Se. Many of the solid acids are monoclinic at room temperature and are known to undergo superprotonic phase transitions at elevated temperatures, ranging from ~ 100 to 300 °C, to high-symmetry, high-conductivity phases. These two materials have the same behavior with an additional phase transition at a lower temperature for each of them. Specifically, $Rb_3H(SeO_4)_2$ transforms from its monoclinic *A2/a* phase to another monoclinic *C2/m* phase at 175 °C before its superprotonic transition occurs at 178 °C giving the high-temperature trigonal *R-3m* phase [1]. $Cs_3H(SeO_4)_2$, on the other hand, is *C2/m* at room temperature and transforms to *A2/a* at 96 °C before further transforming to the same *R-3m* phase at 183 °C [2-7].

Properties and behaviors of solid solutions of other solid acids have been studied to explore the nature and to understand the reasons behind such behaviors, for example, what affects the transition temperatures or what the driving force of the transition is. Louie et al. [8] studied solid solutions of CsH_2PO_4 and RbH_2PO_4 to try to find the correlation between the magnitude of the hysteresis and the crystallographic compatibility between the high- and the low-temperature phases. Also observed in the same work was the change in the superprotonic transition temperature with increasing rubidium content. Ikeda [9] also studied the same solid solution system and $Cs_{1-x}K_xH_2PO_4$ system to investigate the effects of dopants on the transition temperatures,

the dehydration temperatures, and the conductivities of the materials. Chisholm [10], even though the materials he studied were not solid solutions but line compounds between $CsHSO_4$ and CsH_2PO_4, demonstrated that the transition temperatures varied with the ratios of $CsHSO_4$:CsH_2PO_4 and the driving force of the transitions was the configurational entropies change at the transition of each compound.

This current work was carried out to explore the transition behavior, the phase diagram, and the conductivity of $Rb_3H(SeO_4)_2$-$Cs_3H(SeO_4)_2$ solid solutions using a combination of high-temperature X-ray diffraction, A.C. impedance spectroscopy, and differential scanning calorimetry.

4.2 Experimental Methods: Synthesis and Characterization Techniques

4.2.1 Sample preparation

The compositions of $(Cs_xRb_{1-x})_3H(SeO_4)_2$, x = 0–1 with 0.1 increment and x = 0.15, 0.95, 0.98, were examined in this work and were prepared from aqueous solutions of cesium carbonate (Cs_2CO_3, Alfa Aesar 99.99%), rubidium carbonate (Rb_2CO_3, Alfa Aesar 99.8%) and selenic acid (H_2SeO_4, Alfa Aesar 40%) at specific molar ratios of Cs:Rb. Despite the stoichiometric ratio of (Cs+Rb):H = 3:4, the actual ratio used to obtain the pure phase of each composition was fixed to 3:5, except for the pure $Rb_3H(SeO_4)_2$ where the ratio was 3:6. An ice bath and slow addition of selenic acid into carbonate solution were used to prevent excessive heat released from the reaction that can cause decomposition of selenic acid. The solution was then gently heated (below 70 °C) on a hot plate to accelerate water evaporation until the precipitate of the product formed and eventually the whole solution turned into slurry. After the slurry was vacuum-filtered

for a long time to remove residual liquid, the remaining solid was rinsed several times with methanol until it became non-sticky to ensure complete removal of the residual acid. The product was dried in a drying oven at ~ 100 °C overnight before further examination.

4.2.2 Energy-dispersive X-ray spectroscopy (EDS)

Energy-dispersive X-ray spectroscopy was performed on the samples to determine the actual compositions at room temperature using Oxford X-Max SDD X-ray Energy Dispersive Spectrometer. The powder samples were pressed into pellets and polished so that the surfaces of the samples were flat and suitable for EDS measurements. For each sample, at least eight EDS data were collected and the average molar ratio of cesium-to-rubidium was taken.

4.2.3 X-ray diffraction (XRD)

For phase identification of each sample, X-ray diffraction data were obtained using Philips X'Pert Pro diffractometer with Cu Kα radiation at both ambient and high temperatures from 10 to 60° of 2θ with a step size of 0.0167° for a total time of 20:34 minutes for each measurement.

The in situ high-temperature X-ray diffraction data of the samples were collected with Anton Paar HTK1200 high-temperature chamber equipped to the diffractometer under flowing humidified helium (pH_2O ~ 0.023 atm) to prevent dehydration of the solid acids. Prior to data collection, powder samples were compacted into 15-mm-diameter pellets using ~ 194-MPa uniaxial pressure for 15 minutes to facilitate solid-state interdiffusion and phase equilibration. The measurement temperatures were reached at a

ramp rate of 5 °C/min and the samples were allowed to reach equilibrium at each temperature as no changes in the diffraction patterns were observed.

4.2.4 A.C. impedance spectroscopy (ACIS)

9.3-mm-diameter pellet samples were also prepared under 216-MPa uniaxial pressure for 15 minutes for conductivity measurements with PELCO Colloidal silver paste (Ted Pella, #16032) applied on both sides to serve as electrodes. An HP 4284 precision LCR meter was used to obtain A.C. impedance data. The measurements were carried out in the temperature range from 140 to 200 °C, except for $Cs_3H(SeO_4)_2$ to 210 °C, under flowing humidified nitrogen gas with pH_2O ~ 0.023 atm. Every sample was held at 140 °C for at least 30 minutes prior to data collection and the temperature ramp rate was 0.5 °C/min. A set of full spectra (20 Hz to 1 MHz) was collected in the temperature range in order to determine an appropriate frequency to follow the transition behavior for each sample which were 1.6 kHz for $Rb_3H(SeO_4)_2$, 1 kHz for $Cs_3H(SeO_4)_2$, and 2.5 kHz for all of the solid solutions. These frequencies were selected from the frequency giving the intercept on the real axis of the Nyquist plot of the full spectra of each sample. At these frequencies, the real component dominates and the contribution of the imaginary component to the total impedance was minimal, specifically, only 0.04-1.84% for most the samples and 5% for only one sample, $Rb_3H(SeO_4)_2$.

4.2.5 Thermal analysis: Differential scanning calorimetry

A Netzsch STA 449 simultaneous DSC/TG instrument was employed to study thermal behavior of the samples. An amount of 120-180 mg of each sample was used to

prepare a 5.25-mm-diameter pellet under a pressure of ~ 226 MPa for 5 minutes to facilitate solid-state interdiffusion. The pellet samples were examined under flowing humidified nitrogen gas with pH_2O ~ 0.023 atm in the temperature range from 30 to 223 °C for three consecutive thermal cycles at a ramp rate of 10 °C/min, the highest ramp rate among the three methods to improve the DSC signals.

4.3 Determination of Compositions, Solubility Limits, and Volume Expansion at Room Temperature

The actual compositions of the solid solutions determined using EDS are shown in Figure 4.1 and were found to be different from the nominal cesium compositions. This is not unusual for solid acids consisted of multiple ions, especially for those with more than one metal cations, due to different solubility of each compound which allows each compound to form at a different moment. The room-temperature XRD patterns of these compositions (Figure 4.2), nonetheless, showed that every solid solution remained a single phase and retained the structure of $Rb_3H(SeO_4)_2$ with the space group *A2/a* up to 93% Cs, while the composition from 98% Cs and above adopted the structure of $Cs_3H(SeO_4)_2$ with the space group *C2/m*. This indicates that the missing cations did not form solid products and were filtered out during the synthesis or the amounts of other compounds that might form were so small that XRD could not detect. The two-phase region of *A2/a* and *C2/m* was found to be small, between 93 and 98% Cs as the XRD pattern of 97%-Cs sample depicted.

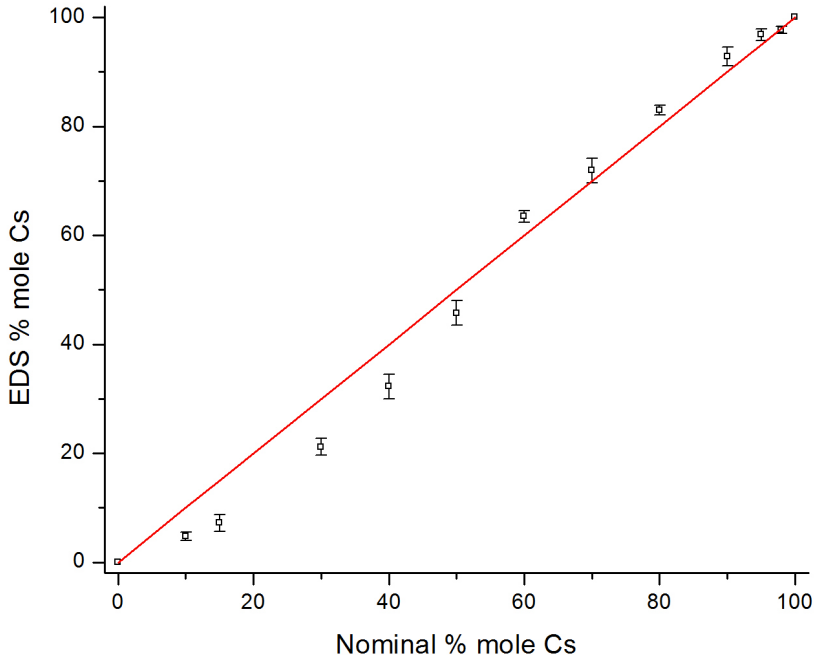

Figure 4.1. Actual compositions of the $(Cs_xRb_{1-x})_3H(SeO_4)_2$ solid solutions determined using EDS.

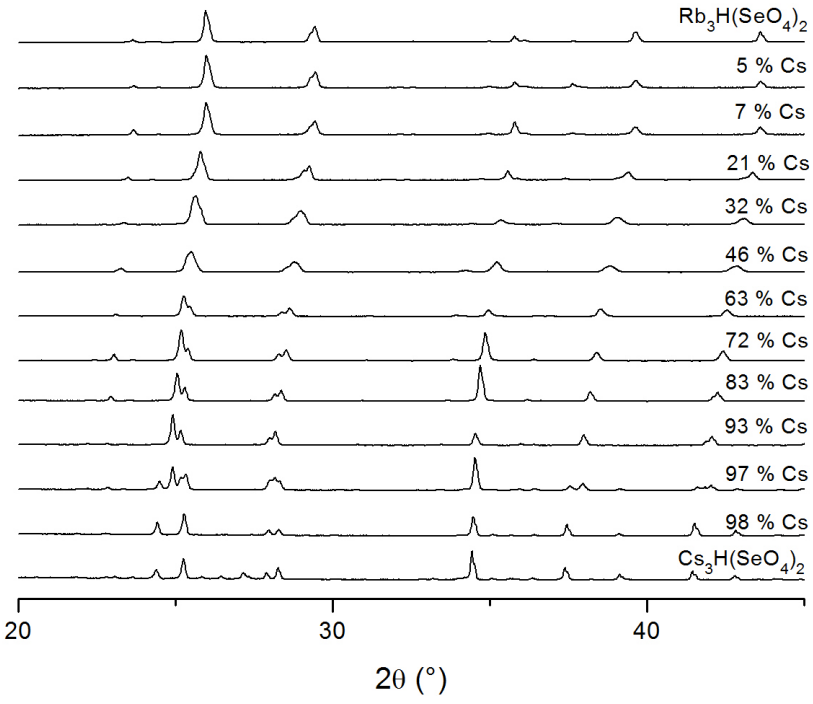

Figure 4.2. XRD patterns of the $(Cs_xRb_{1-x})_3H(SeO_4)_2$ solid solutions at room temperature. The pattern of 97%-Cs composition indicates two phases co-existed.

Rietveld refinements were performed on all diffraction data to determine the lattice parameters (not shown here) and the cell volumes (shown in Figure 4.3) of the solid solutions. The unit cells of both phases (*A2/a* and *C2/m*) expand monotonically with cesium content as expected since the ionic radius of cesium is larger than that of rubidium.

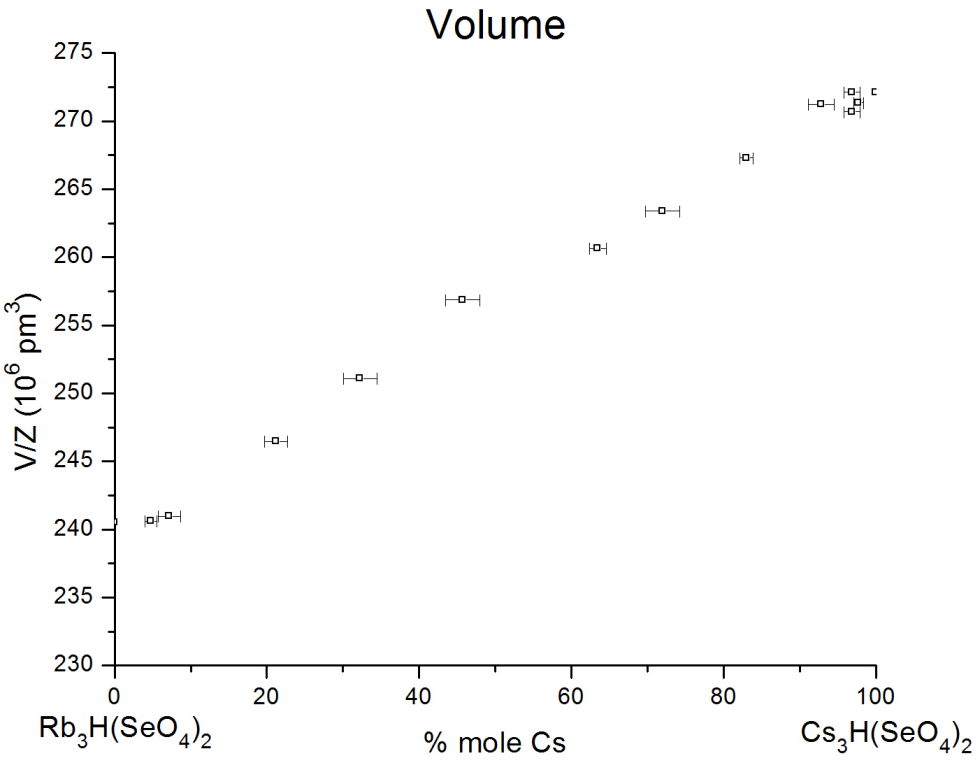

Figure 4.3. Volume expansion of the unit cells of the $(Cs_xRb_{1-x})_3H(SeO_4)_2$ solid solutions upon increasing content of cesium.

4.4 High-Temperature Phase Identification

High-temperature X-ray diffraction (HT-XRD) data were used to determine the phase diagram of the system. Five out of thirteen studied data sets were shown in Figure 4.4 a to e as representatives of the three regions observed at room temperature mentioned above and the two end members.

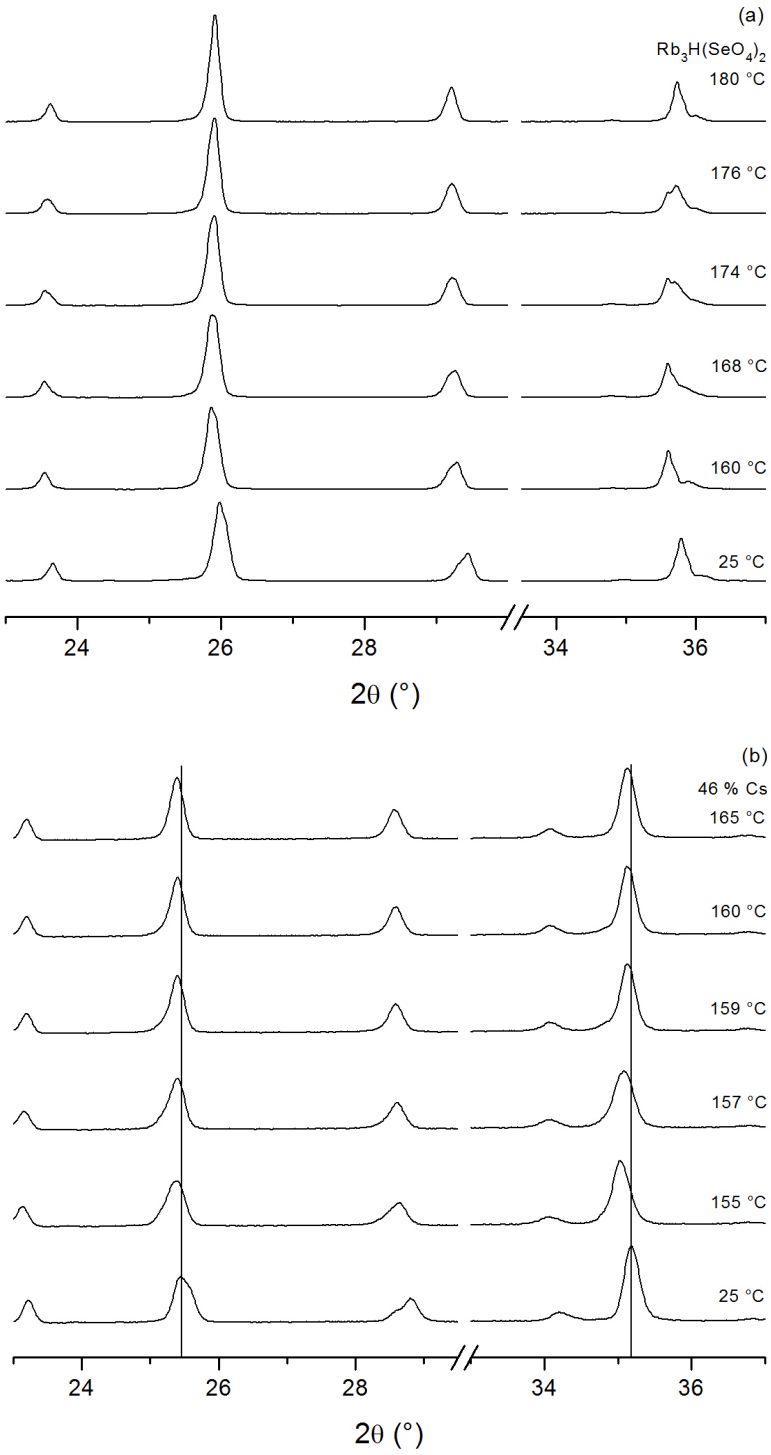

Figure 4.4 (See caption on next page)

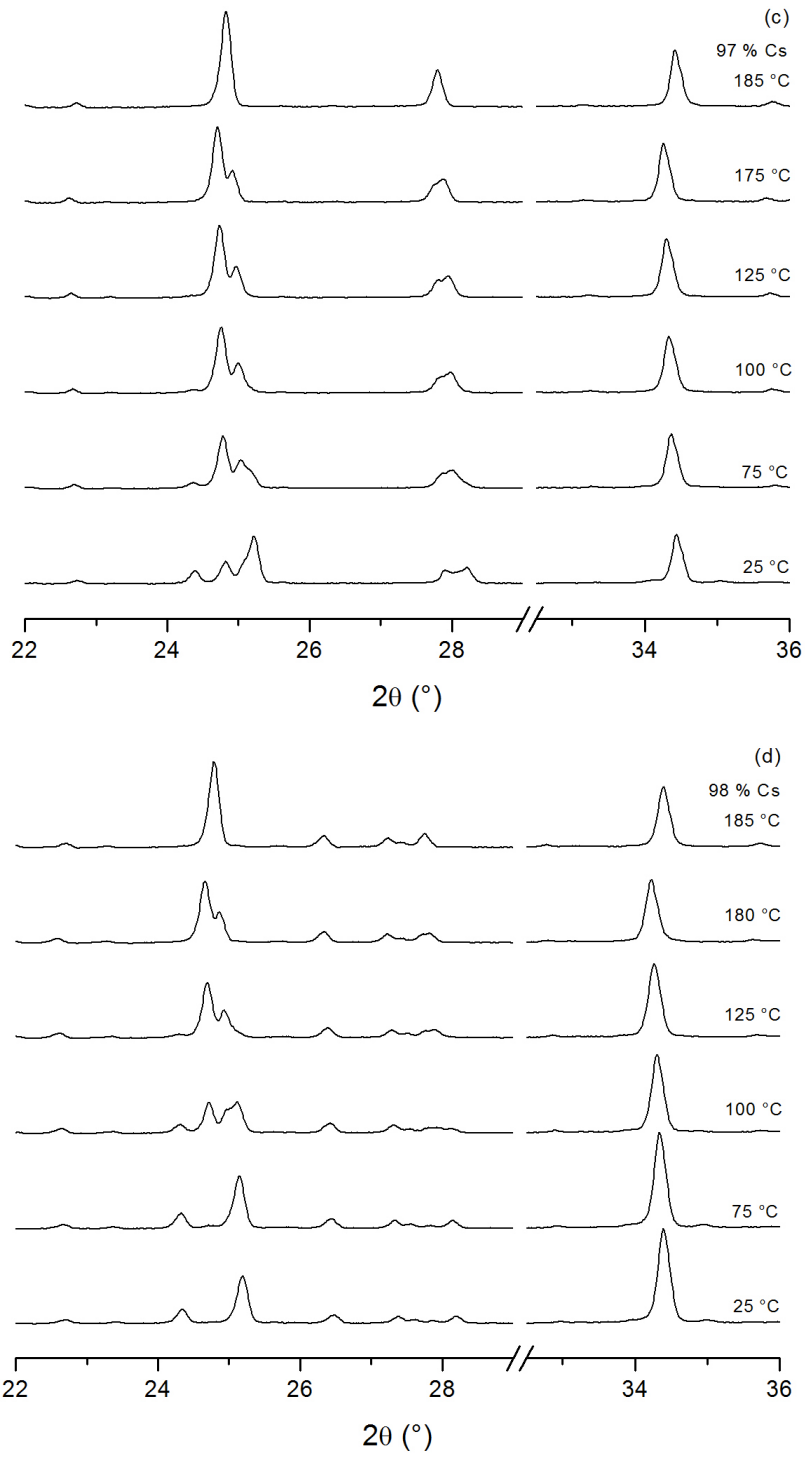

Figure 4.4 (See caption on next page)

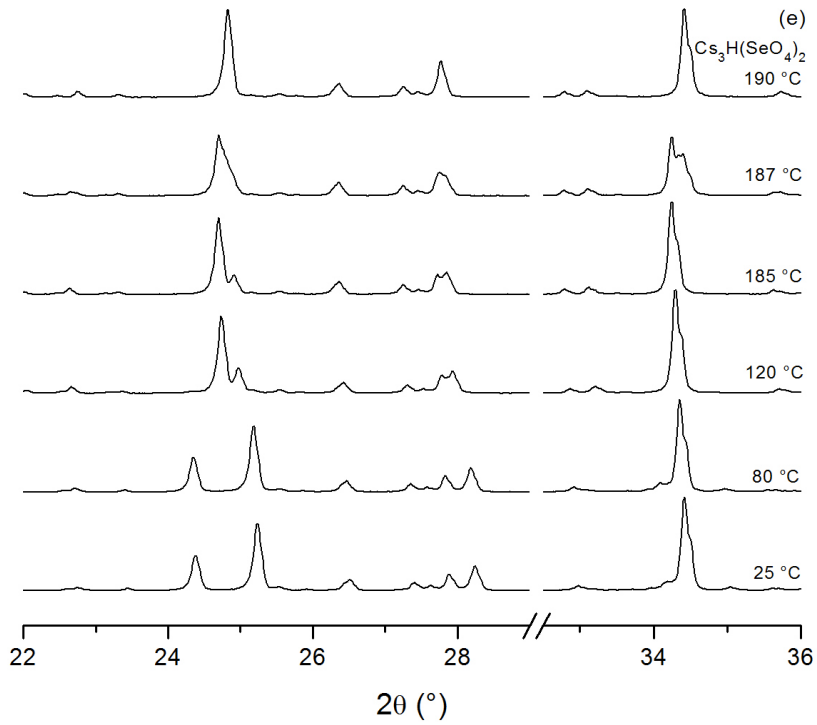

Figure 4.4. Equilibrium HT-XRD patterns at indicated temperatures under humidified helium (pH_2O ~ 0.023 atm) of (a) $Rb_3H(SeO_4)_2$, (b) 46%-Cs, (c) 97%-Cs, (d) 98%-Cs compositions, and (e) $Cs_3H(SeO_4)_2$. The vertical lines in (b) are meant to help notice the small peak shifts.

The HT-XRD patterns of $Rb_3H(SeO_4)_2$, Figure 4.4a, shows very minimal changes in peak shape and peak positions as the low-temperature and the high-temperature phases are highly compatible, i.e. the crystallographic planes barely move to transform from one to the other phase. However, two small changes could be observed in the peak at ~ 35.8° of 2θ at 168 and 180 °C indicating the transition temperatures which are close to reported values [11-14]. The low-temperature phase (T < 168 °C) again is the monoclinic *A2/a* and the high-temperature phase (T > 180 °C) is the trigonal *R-3m*. The intermediate phase (168 < T < 180 °C), even though could not be recognized clearly here, is another monoclinic *C2/m*, according to the literatures [1].

The changes in HT-XRD patterns of the 46% Cs composition, Figure 4.4b, were even harder to be noticed, but still distinguishable as follows: The peak at 35.2° moved to lower 2θ as the sample was heated from 25 to 155 °C because of thermal expansion of the lattice. The same peak, though, started to shift upward to higher angle at 157 °C, indicating the phase transformation, and eventually settled at 159 °C before moving downward again at higher temperatures due to thermal expansion as usual. Both the low- and the high-temperature phases in this case are still *A2/a* and *R-3m*, respectively, as found in $Rb_3H(SeO_4)_2$. The two-phase region is small (157-159 °C) and the phase boundaries are considered 'converged' at this composition. Other compositions, which have *A2/a* structure at room temperature, on the other hand, gave larger temperature range of the two-phase region (data not shown).

The patterns of the 97% Cs composition, which represents the compositions in the two-phase region at room temperature, are presented in Figure 4.4c. The two phases became a single phase of *A2/a* after the sample was heated to 100 °C and transformed to *R-3m* at 185 °C.

The 98% Cs composition, although started off with a single *C2/m* phase, passed through a two-phase region of *A2/a* and *C2/m*, as can be seen in Figure 4.4d, as the pellet sample was heated to 100 °C. Nevertheless, this two-phase region was small since the pattern at 125 °C shows that the sample turned into another single phase of *A2/a* before further transformed to *R-3m* at 185 °C.

The patterns of $Cs_3H(SeO_4)_2$ in Figure 4.4e shows similar results as previously reported by other authors [3-7]. The room-temperature phase of the monoclinic *C2/m*

transformed to another monoclinic phase, *A2/a*, at a temperature between 80 and 120 °C and then to the trigonal *R-3m* at 190 °C.

The high-temperature phases of all composition examined in this work are confirmed to be the same phase with different lattice parameters because the peak positions of the HT-XRD patterns shown in Figure 4.5 shift to lower 2θ as the cesium percentage increases and no new peaks from phase separation were observed. In other words, this system has full-range solubility at high temperature.

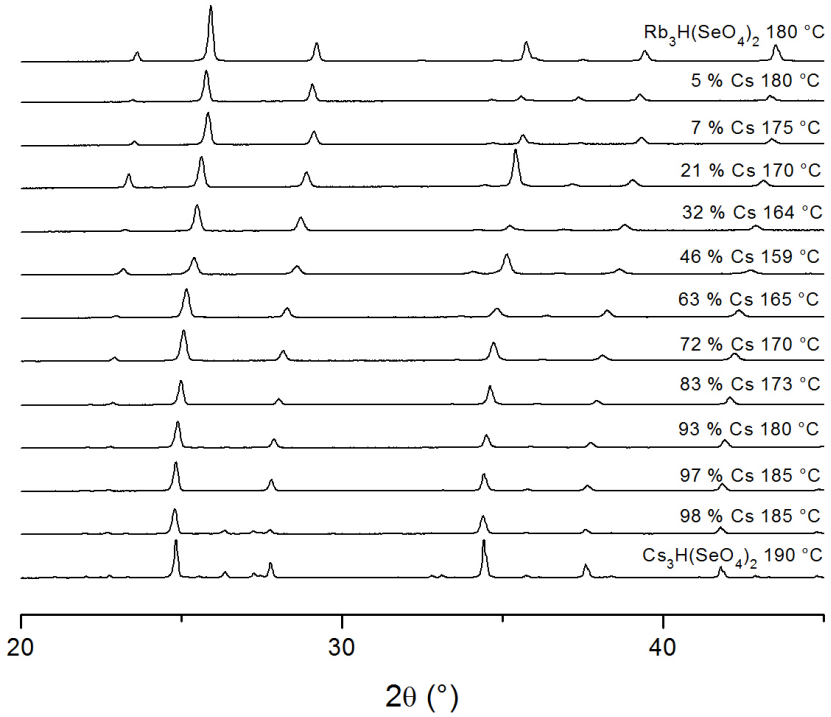

Figure 4.5. Equilibrium HT-XRD patterns of all composition under humidified helium (pH_2O ~ 0.023 atm), each at a temperature just above its superprotonic transition temperature as indicated.

4.5 Conductivity Studies

Figure 4.6 a and b show the results from the conductivity measurements of $Rb_3H(SeO_4)_2$, $Cs_3H(SeO_4)_2$, and their solid solutions. A sharp increase in conductivity, indicating the phase transition from a low-temperature, low-conductivity phase, *A2/a*, to a high-temperature, high-conductivity phase, *R-3m*, i.e. the superprotonic transition, occurred in the plot of each composition at a different temperature. The superprotonic transition temperature (T_{SP}) decreased from 180 °C of the pure $Rb_3H(SeO_4)_2$ to ~ 159 °C at 46% Cs, then increased again to 188 °C of the pure $Cs_3H(SeO_4)_2$. The transition temperatures of $Rb_3H(SeO_4)_2$ and $Cs_3H(SeO_4)_2$ quite agreed with previously reported temperatures from ACIS of 178-182 [11, 13] and 193 °C [11], respectively.

The hysteresis of the solid solutions became larger around 50% Cs and got smaller as the compositions approach either end members of the system. Nevertheless, the overall magnitude of the hysteresis of this system is still very small, ranging from 0.75 to 4.23 °C, compared to other solid acids.

The high-temperature conductivities of the solid solutions including those of the two end members at 200 °C are shown in Figure 4.7. The most outstanding feature of this system is that the superprotonic conductivities of all intermediate compositions are significantly higher than those of the two end members, especially those of the compositions rich in Rb (5 – 20% Cs) that are 30 – 40 times higher. $(Cs_xRb_{1-x})_3H(SeO_4)_2$ is the first solid solution system amongst other solid acids to show this improved conductivities; those of the others decrease with dopant contents [9].

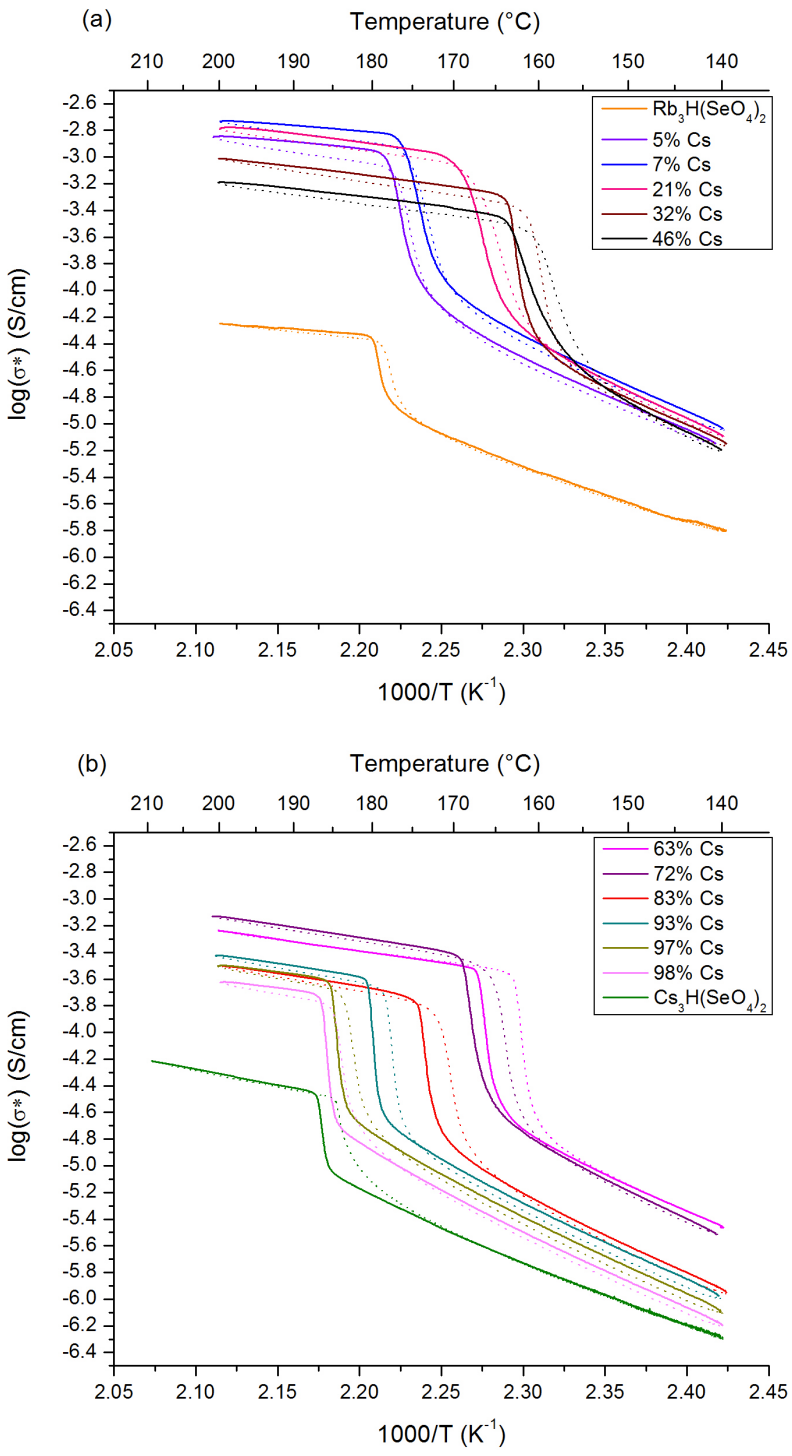

Figure 4.6. Conductivity plots of all compositions in $(Cs_xRb_{1-x})_3H(SeO_4)_2$ system upon heating (solid line) and cooling (dotted line) under humidified nitrogen (pH_2O ~ 0.023 atm) at a ramp rate of 0.5 °C/min: (a) 0-50% Cs and (b) 60-100% Cs.

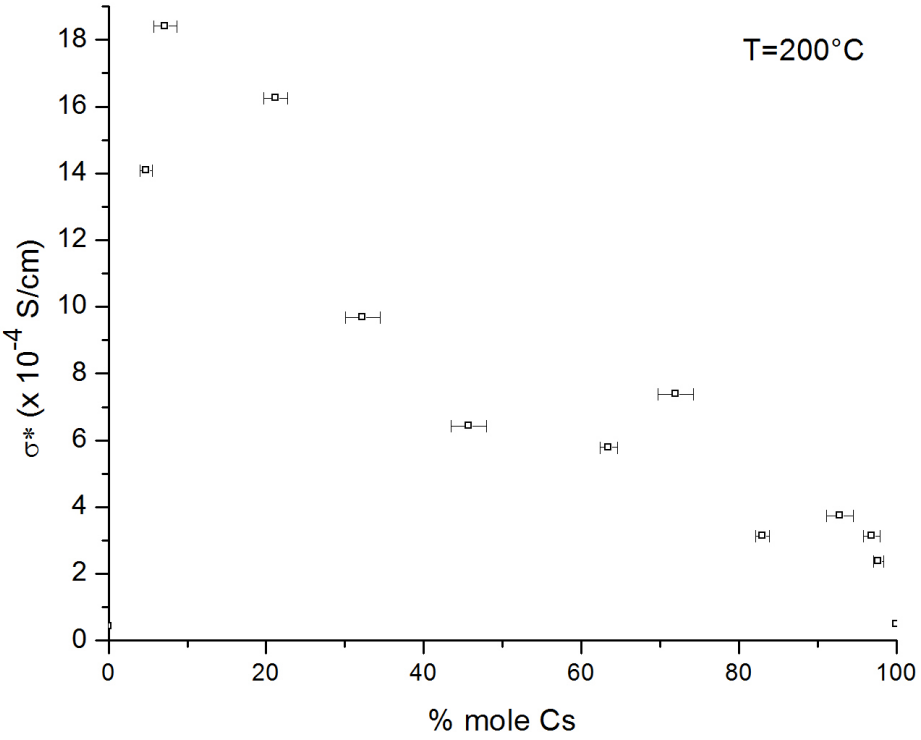

Figure 4.7. The conductivities of all compositions in $(Cs_xRb_{1-x})_3H(SeO_4)_2$ system at 200 °C.

4.6 DSC Studies: Enthalpies and Entropies of Superprotonic Phase Transition

Thermal behaviors of the samples were studied using DSC and three data sets are selected and shown in Figure 4.8 as examples. As can be seen in the examples, the DSC profiles of the compositions adopting the $Rb_3H(SeO_4)_2$ structure showed only one endothermic peak on heating with one corresponding exothermic peak on cooling, while those of the compositions with the $Cs_3H(SeO_4)_2$ structure revealed two endothermic peaks. These behaviors were expected as both $Cs_3H(SeO_4)_2$ and $Rb_3H(SeO_4)_2$ have two phase transitions reported previously in the temperature range examined: For $Cs_3H(SeO_4)_2$, at 96 and 183 °C [2] and for $Rb_3H(SeO_4)_2$, at 175 and 178 °C [1] which obviously are very close to each other and often cannot be separately detected in many

experiments and it was the case here where these two signal peaks overlapped and formed one peak. The transition of interest, however, is still the one at the higher temperature as the conductivity results showed earlier that it was where the superprotonic transition occurred. The T_{SP} observed by DSC showed the same behavior as the one by A.C. impedance spectroscopy. Again, the T_{SP} decreased from 167 °C of $Rb_3H(SeO_4)_2$ to a minimum temperature, 159 °C of the 46% Cs composition, then went back up to 185 °C of $Cs_3H(SeO_4)_2$.

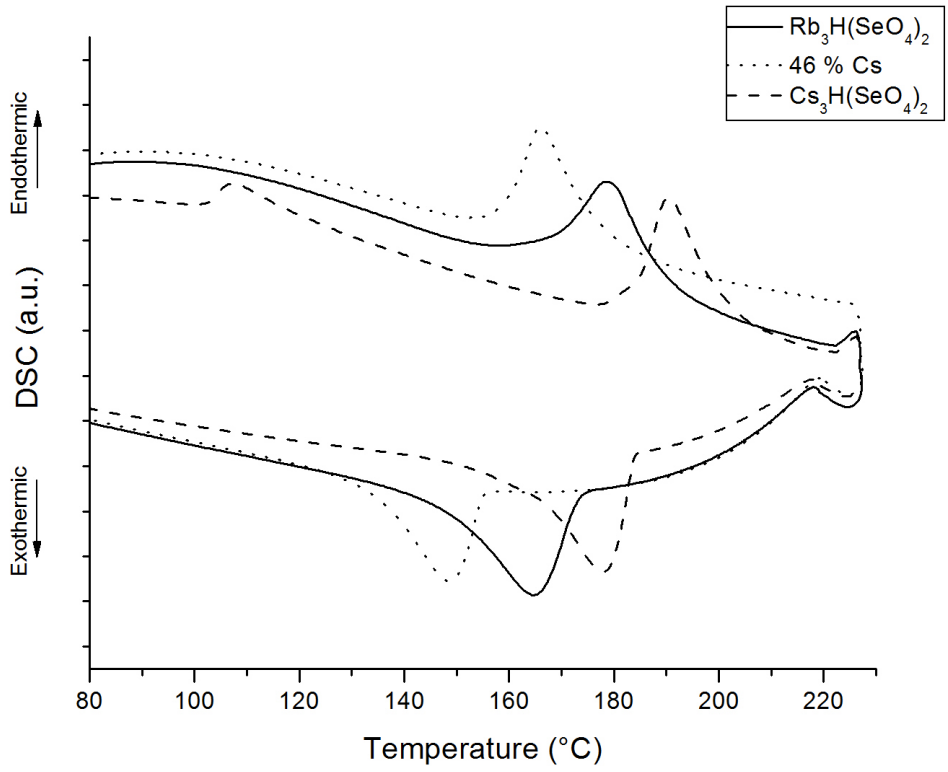

Figure 4.8. DSC profiles of $Rb_3H(SeO_4)_2$, 46%-Cs composition, and $Cs_3H(SeO_4)_2$ under humidified nitrogen (pH_2O ~ 0.023 atm) at a ramp rate of 10 °C/min.

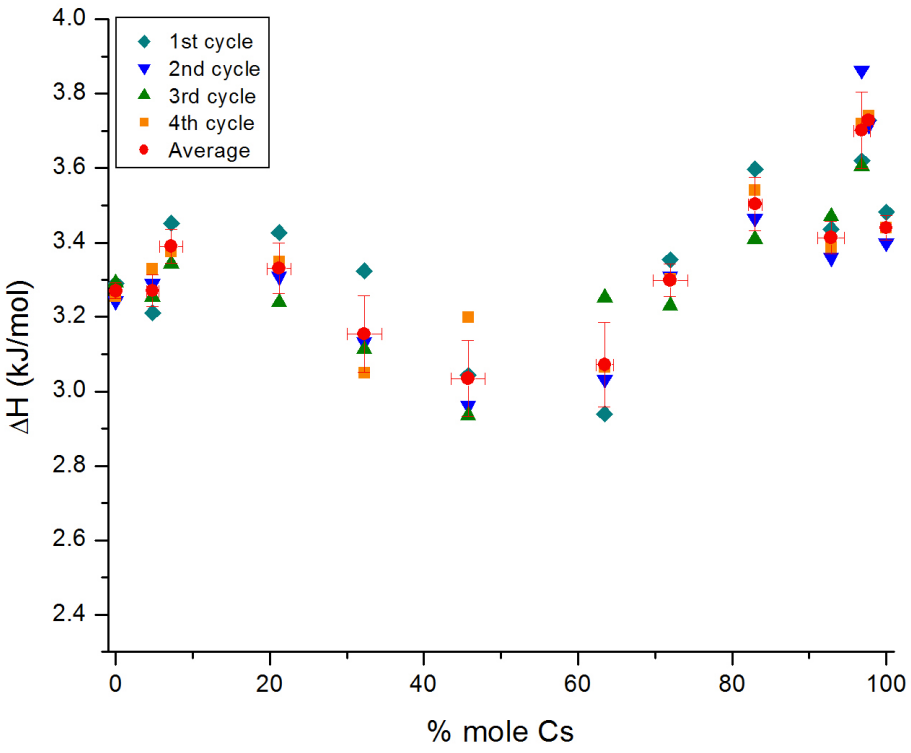

Figure 4.9. Enthalpies of superprotonic transitions of all compositions in $(Cs_xRb_{1-x})_3H(SeO_4)_2$ system. The x-error bars of the averages also represent those of the other points of the same compositions.

Figure 4.9 shows the enthalpy (ΔH) of the superprotonic transformation of every composition. The enthalpy of the transition of $Rb_3H(SeO_4)_2$ was 3.27 kJ/mol which agreed well with the values reported in the literatures (3.0-3.8 kJ/mol) [12-14], while that of $Cs_3H(SeO_4)_2$ was 3.44 kJ/mol, somewhat lower than 4.3 kJ/mol reported by Kirpichnikova et al. [12]. The heats of the solid solutions generally decreased from 3.39 kJ/mol of the 7%-Cs composition to 3.03 kJ/mol of the 46%-Cs composition, where once again the minimum occurred, then increased to 3.73 kJ/mol of the 98%-Cs composition. The entropy of $Rb_3H(SeO_4)_2$ was 7.43 J/(mol·K) which fell in the range of the published values, 6.7-8.2 J/(mol·K) [12-14], and that of $Cs_3H(SeO_4)_2$ was 7.48 J/(mol·K), again lower than the published value of 9.3 J/(mol·K) [12].

4.7 Phase Diagram and Variation of the Superprotonic Transition Temperature of $Rb_3H(SeO_4)_2$-$Cs_3H(SeO_4)_2$ System

The superprotonic transition temperatures of the system from all three methods, summarized in Figure 4.10, were consistent with one another with some deviations due to the limitations of the methods. Once again, every method detected a minimum of T_{SP} at 46% Cs and it is noteworthy that this solid solution system is the first to show this behavior among the other systems of solid acids. With the results from the three methods combined, the schematic phase boundaries could be determined, as also shown in Figure 4.10, and the two-phase region upon heating of each composition was small, ranging from 0 to 5 °C, and converged at the minimum temperature. The boundaries on the left side of the diagram are a little more complicated than the other part and were not studied in detailed; however, they were estimated from some results in this work and the presence of the intermediate phase of $Rb_3H(SeO_4)_2$ at 176 °C [1].

Further combination of Figure 4.10 and the results from room- and high-temperature XRD below the superprotonic transition allows construction of the phase diagram of the $Rb_3H(SeO_4)_2$-$Cs_3H(SeO_4)_2$ system proposed in Figure 4.11.

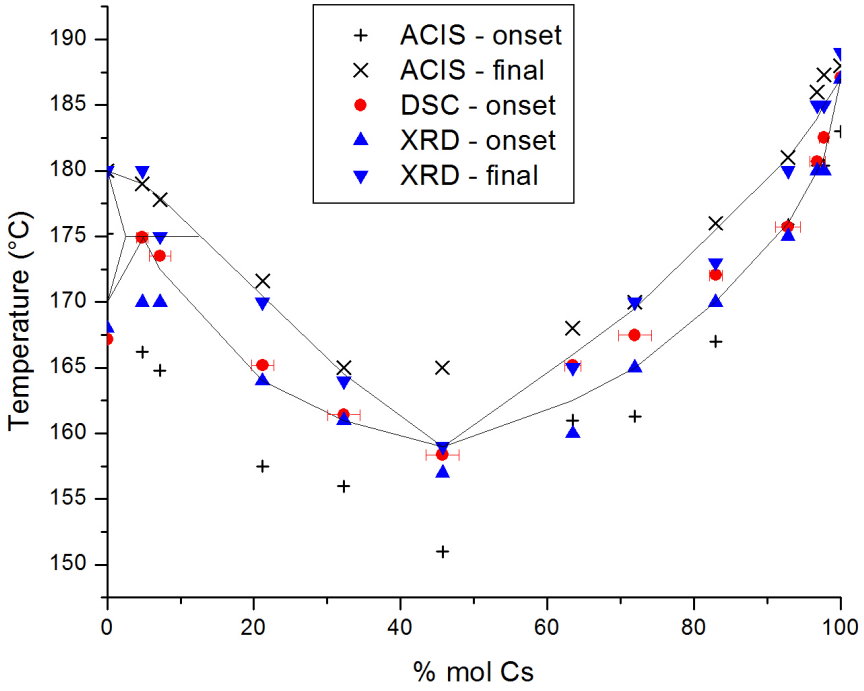

Figure 4.10. Superprotonic transition temperatures of all compositions in $(Cs_xRb_{1-x})_3H(SeO_4)_2$ system from HT-XRD, ACIS, and DSC. The x-error bars of the transition temperatures determined by DSC also represent those of the other points of the same compositions.

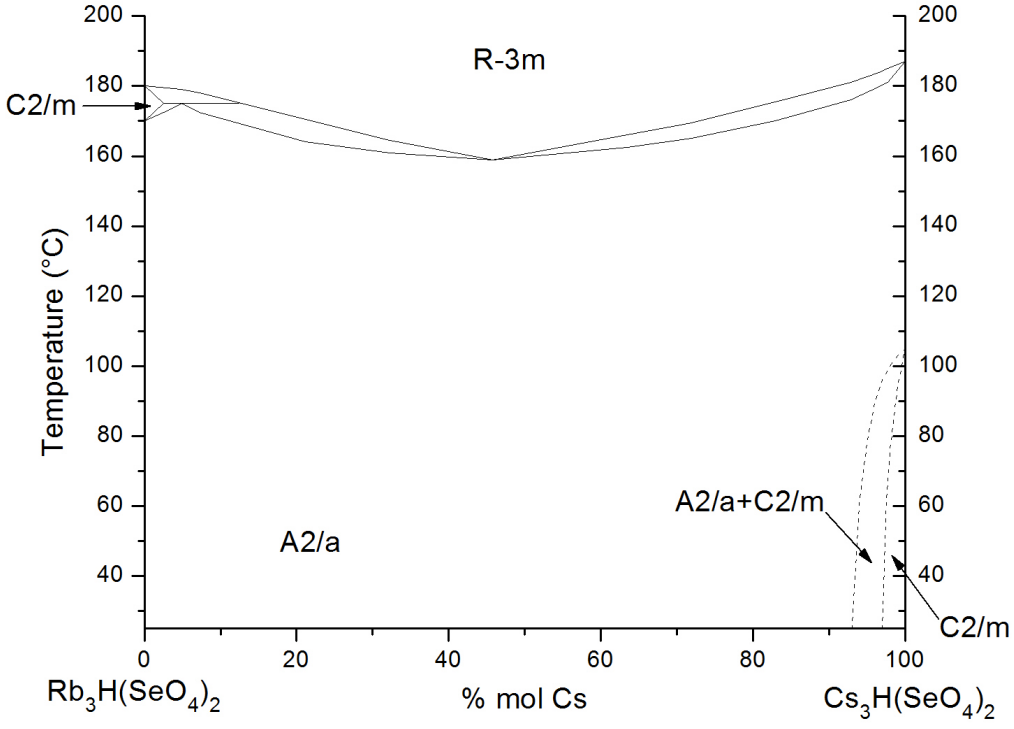

Figure 4.11. Phase diagram for the $(Cs_xRb_{1-x})_3H(SeO_4)_2$ system.

The entropies of the transitions of all of the compositions are taken to be a constant, R·ln 3 J/(mol·K), for the following reason: The entropy of the transition consists of (1) the change in the mixing entropy, ΔS_{mix}, of Cs and Rb ions from the low- to the high-temperature phase and (2) the change in the configurational entropy, ΔS_{config}, from the low- to the high-temperature phase. The ΔS_{mix} is zero because the composition does not change upon transition. The $\Delta S_{config} = R \cdot \ln(\Omega)$, where Ω is the number of equivalent, distinguishable ways of hydrogen-bond formation. For the transition of this system from *A2/a* to *R-3m*, $\Omega = 3$ [15]. Thus, $\Delta S = \Delta S_{mix} + \Delta S_{config} = 0 + R \cdot \ln 3 = 9.13$ J/(mol·K).

From the trends of ΔH in Figure 4.9 and T_{SP} in Figure 4.10, it can be concluded that the superprotonic transition temperature of this solid solution system varies with the enthalpy of transformation which can be explained as follows: At the transition, the chemical potentials of the two phases are equal, hence the Gibb's free energy is zero and ΔH equals $T_{SP} \cdot \Delta S$. ΔS of these solid solutions are constant as described above. Therefore, T_{SP} varies with the heat of transformation.

4.8 Conclusions

With the results from XRD, A.C. impedance spectroscopy, and DSC, the phase diagram at room temperature of the $Rb_3H(SeO_4)_2$-$Cs_3H(SeO_4)_2$ system is divided into three regions: *A2/a* phase of $Rb_3H(SeO_4)_2$ below 93% Cs, two-phase region of *A2/a*+*C2/m* between 93 – 98% Cs, and *C2/m* phase of $Cs_3H(SeO_4)_2$ above 98% Cs. All compositions, however, became a single phase of *A2/a* above 100 °C before underwent the superprotonic transition at various temperatures through a small two-phase region,

depending on the composition, to the same trigonal phase, *R-3m*. The transition temperature has a minimum at 46% Cs as opposed to either an increasing or a decreasing trend with the increasing dopant and varies with the enthalpy of the superprotonic transition. The superprotonic conductivities of the intermediate compositions increased tremendously. At 5 – 20% Cs content, they increased ~ 40-fold.

4.9 References

[1] B.V. Merinov, S.M. Haile, U. Bismayer, *Solid State Ionics* **146** (2002) (3-4) 355.

[2] Y. Matsuo, Y. Tanaka, J. Hatori, S. Ikehata, *Solid State Communications* **134** (2005) (5) 361.

[3] B.V. Merinov, A.I. Baranov, L.A. Shuvalov, *Kristallografiya* **35** (1990) (2) 355.

[4] B.V. Merinov, N.B. Bolotina, A.I. Baranov, L.A. Shuvalov, *Kristallografiya* **33** (1988) (6) 1387.

[5] B.V. Merinov, N.B. Bolotina, A.I. Baranov, L.A. Shuvalov, *Kristallografiya* **36** (1991) (5) 1131.

[6] R. Sonntag, R. Melzer, T. Wessels, P.G. Radaelli, *Acta Crystallographica Section C-Crystal Structure Communications* **53** (1997) 1529.

[7] M. Komukae, K. Sakata, T. Osaka, Y. Makita, *J. Phys. Soc. Jpn.* **63** (1994) (3) 1009.

[8] M.W. Louie, M. Kislitsyn, K. Bhattacharya, S.M. Haile, *Solid State Ionics* **181** (2010) (3-4) 173.

[9] A. Ikeda, Superprotonic solid acids : thermochemistry, structure, and conductivity, *Materials Science*, California Institute of Technology, Pasadena, California (2013).

[10] C.R.I. Chisholm, Superprotonic Phase Transitions in Solid Acids: Parameters affecting the presence and stability of superprotonic transitions in the MHnXO4 family of compounds (X=S, Se, P, As; M=Li, Na, K, NH4, Rb, Cs), *Materials Science*, California Institute of Technology, Pasadena, California (2003).

[11] A. Pawlowski, C. Pawlaczyk, B. Hilczer, *Solid State Ionics* **44** (1990) (1-2) 17.

[12] L. Kirpichnikova, B. Hilczer, M. Polomska, L. Szczesniak, A. Pawlowski, *Solid State Ionics* **145** (2001) (1-4) 191.

[13] A. Pawlowski, L. Szczesniak, M. Polomska, B. Hilczer, L. Kirpichnikova, *Solid State Ionics* **157** (2003) (1-4) 203.

[14] A. Pawlowski, M. Polomska, B. Hilczer, L. Szczesniak, A. Pietraszko, *Journal of Power Sources* **173** (2007) (2) 781.

[15] A.I. Baranov, *Crystallogr Rep*+ **48** (2003) (6) 1012.

Chapter 5 Transition Behaviors of $Cs_6(H_2SO_4)_3(H_{1.5}PO_4)_4$ and Apparent Negative Thermal Expansion at High Temperature

5.1 Introduction

Solid acids are chemical intermediates between oxy acids and its salts. Many solid acids are found to undergo superprotonic phase transition at elevated temperatures (~ 100 – 300 °C) where their conductivities usually suddenly increases by 3 – 4 orders of magnitude due to the changes of their structures from low-symmetry phases to their respective high-symmetry phases. Most of the compounds in $CsHSO_4$-CsH_2PO_4 family exhibit the same way. Specifically, they are monoclinic, such as *C*2/c and $P2_1/m$, at room temperature and transform to tetragonal $I4_1/amd$ or cubic *P*m-3m phases [1-9]. Even though in this family, $Cs_6(H_2SO_4)_3(H_{1.5}PO_4)_4$ becomes of interest due to the fact that it is already a cubic structure with *I*-43d space group, but still transforms to another cubic *P*m-3m phase and exhibits the superprotonic behavior [9]. The driving force of the transitions in $CsHSO_4$-CsH_2PO_4 system was determined by Chisholm to be the entropies of the transitions [9]. Another interesting property of $Cs_6(H_2SO_4)_3(H_{1.5}PO_4)_4$, also previously observed by Chisholm [9], is the negative thermal expansion in the high-temperature phase which has never been found in any other solid acid compounds before.

The objectives of this work are to explore the physical properties and to understand the transition behavior and the origin of the negative thermal expansion observed in $Cs_6(H_2SO_4)_3(H_{1.5}PO_4)_4$.

5.2 Experimental Methods

5.2.1 Sample preparation

Crystals of $Cs_6(H_2SO_4)_3(H_{1.5}PO_4)_4$ were prepared by slow evaporation of water from an aqueous solution consisted of cesium carbonate (Cs_2CO_3, Alfa Aesar 99.99%), sulfuric acid (H_2SO_4, EMD Chemicals 95-98%), and phosphoric acid (H_3PO_4, Fisher Scientific 85%) in the stoichiometric ratio. Some large crystals (larger than ~ 2 mm × 4 mm × 5 mm) were carefully extracted from the mother liquor and rinsed quickly with a few drops of water to remove the remaining solution on the their surfaces. Even though rinsing with water dissolved the exterior of the crystals, it was the best way to obtain the pure phase since using an organic solvent such as methanol or acetone would cause other compounds to precipitate on the crystals. The rinsing water was combined with the mother liquor to ensure that the stoichiometry of the solution remained the same. This solution was then allowed to evaporate further until completely dried. The dry chunk of the product was ground in a mortar and pestle to form polycrystalline $Cs_6(H_2SO_4)_3(H_{1.5}PO_4)_4$.

5.2.2 Energy-dispersive X-ray spectroscopy (EDS)

The composition of the sample at room temperature was determined using Oxford X-Max SDD X-ray Energy Dispersive Spectrometer. The powder sample was pressed into pellets and polished so that its surface was flat and suitable for EDS measurements. Eight EDS data were collected and the atomic percentages of cesium, sulfur, phosphorus, and oxygen were taken.

5.2.3 X-ray diffraction (XRD)

Philips X'Pert Pro diffractometer with Cu Kα radiation was utilized at room and elevated temperatures for phase identification. Diffraction data of the samples were collected over the 2θ range from 10 to 60° with a step size of 0.0167° resulting in a total time of 20:34 minutes for each measurement.

The XRD patterns at high temperatures were obtained *in situ* using a high-temperature chamber HTK1200 from Anton Paar. The powder sample was pressed using ~ 194-MPa uniaxial pressure for 15 minutes to form 15-mm-diameter compacts before the measurements to promote interdiffusion and phase equilibration in the solid. The high-temperature experiments were conducted for two purposes: 1) study the transition behaviors and determine the lattice parameters; and 2) study the effect of humidity level on dehydration of the compound at a fixed temperature.

To study the transition behaviors and determine the lattice parameters, the measurements were carried out both under stagnant ambient atmosphere (pH_2O ~ 0.011 atm) and under flowing humidified helium (pH_2O ~ 0.023 atm). The temperature ramp rate was 5 °C/min and the pellet samples were hold at each temperature until reaching equilibrium, i.e. until the diffraction patterns were stable.

To study the effect of humidity level, the sample was heated up and held at 120 °C under flowing humidified helium (pH_2O ~ 0.023 atm) until the equilibrium was reached before the diffraction pattern was taken. The atmosphere was then changed to flowing dry helium and the sample was allowed to reach the new equilibrium before its diffraction pattern was collected. The atmosphere was switched between humidified and dry helium three times and a diffraction pattern was collected each time.

5.2.4 Physical observations of a crystal sample

The crystal sample was heated up to 130 °C both under stagnant ambient atmosphere of which pH_2O measured using a humidity sensor was about 0.011 atm and under flowing humidified nitrogen gas with pH_2O ~ 0.023 atm to study physical changes due to the phase transition. Magnified images of the crystal were taken using an optical microscope and the microstructures were examined using ZEISS 1550VP field emission scanning electron microscope.

5.2.5 A.C. impedance spectroscopy (ACIS)

The impedances of the polycrystalline sample were measured using an HP 4284 precision LCR meter. The polycrystalline sample was also compacted into 9.3-mm-diameter pellets under 15 minutes of ~ 216-MPa uniaxial pressure. PELCO Colloidal silver paste (Ted Pella, #16032) was applied onto opposing sides of the pellets to be electrodes. The measurements of the samples were performed under two atmosphere, dry and humidified (pH_2O ~ 0.023 atm) nitrogen, in the temperature range from 60 to 122 °C with a ramp rate of 0.1 °C/min for both cases. Single-frequency mode, which allowed for continuous recordings, was employed to capture the transition behavior. After full spectrum scans (20 Hz to 1 MHz), an appropriate frequency of 2 kHz was selected. At this frequency, the imaginary part contributed to the total impedance only at most 0.42% for the pellet.

5.2.6 Thermal analysis: Differential scanning calorimetry (DSC) and thermal gravimetry (TG)

5.25-mm-diameter pellets were prepared from the powder sample using ~ 226 MPa pressure for 5 minutes, again to facilitate the diffusion. The samples were examined in a Netzsch STA 449 simultaneous DSC/TG system. The atmospheres were controlled to have three levels of water partial pressure: < 0.001, 0.011, and 0.023 atm. The temperature range was from 30 to 122 °C with a ramp rate of 1 °C/min for the study of the transformation below 122 °C and the samples were heated up to 220 °C to study the dehydration.

5.3 Determination of Composition, Phase Identification, and Crystal Structure at Room Temperature

The composition of the synthesis product determined using EDS is shown in Table 5.1 in comparison to the expected normalized atomic percentages and ratios of S:P and Cs:(S+P) in the proposed formula, $Cs_6(H_2SO_4)_3(H_{1.5}PO_4)_4$. The measured values and ratios were very close to the ideal values. The XRD pattern of the sample collected at room temperature, shown in Figure 5.1, matched very well with that presented by Chisholm [9] and no reflections from other phases were observed. The combination of the results from EDS and XRD confirmed that the product was a pure phase of the new compound $Cs_6(H_2SO_4)_3(H_{1.5}PO_4)_4$.

Table 5.1. Atomic percentages of the elements in $Cs_6(H_2SO_4)_3(H_{1.5}PO_4)_4$ without H and ratios of S:P and Cs:(S+P) calculated from the proposed formula and from the determination using EDS.

	O	Cs	S	P	S:P	Cs:(S+P)
Normalized atomic percentage in formula	68.3	14.6	7.3	9.8	75.0	85.7
Average atomic percentage by EDS	71.1(11)	12.9(8)	6.8(2)	9.2(4)	74.0(32)	81.0(41)

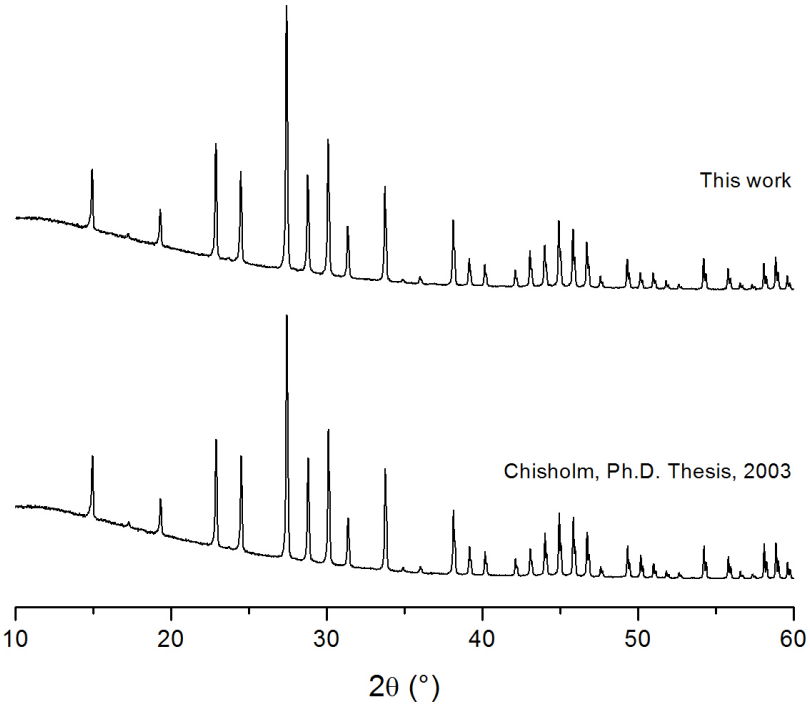

Figure 5.1. XRD pattern of $Cs_6(H_2SO_4)_3(H_{1.5}PO_4)_4$ synthesized in this work compared with that of the one reported by Chisholm [9].

The diffraction data were further refined via Rietveld method using the atomic coordinates also reported by Chisholm [9] as the initial values. At room temperature, the material is cubic with space group *I*-43d and refinement yielded a_0 = 14.5413(4) Å, V = 3074.7(1) $Å^3$, and the atomic parameters listed in Table 5.2. It was also determined that the number of formula unit per unit cell, Z, was 4. Consequently, the calculated density is 3.1919 g/cm^3. The occupancy and the isotropic displacement parameters for all elements have not been refined. The final refinement parameters are R_{wp} = 6.765%, R_{Bragg} = 6.679%, and GOF = 13.867.

Table 5.2. Atomic coordinates, sites, isotropic displacement parameters, and occupancies in $Cs_6(H_2SO_4)_3(H_{1.5}PO_4)_4$ at 25 °C in space group *I*-43d with a_0 = 14.5413(4) Å, V = 3074.7(1) $Å^3$, Z = 4, density = 3.1919 g/cm^3, R_{exp} = 1.817%, R_{wp} = 6.765%, R_{Bragg} = 6.679%, and GOF = 13.867.

Atom	Site	Occupancy	x	y	z	B ($Å^2$)
H	48e	1.0000	0.69(2)	0.84(2)	0.84(1)	0.50
Cs	24d	1.0000	0.7500	0.8483(2)	1.0000	0.50
P	16c	1.0000	0.7443(8)	0.7443(8)	0.7443(8)	0.50
S	12a	1.0000	0.7500	0.1250	1.0000	0.50
O(1)	48e	1.0000	0.696(1)	0.859(2)	0.794(1)	0.50
O(2)	48e	1.0000	0.684(1)	0.187(2)	0.020(2)	0.50
O(3)	16c	1.0000	0.706(2)	0.706(2)	0.706(2)	0.50

5.4 High-Temperature Phase Behavior and Determinations of Lattice Parameters

A set of high-temperature X-ray diffraction experiments, illustrated in Figure 5.2 a-d, was performed to study the transition behaviors of the sample under different humidity levels and maximum temperatures.

Firstly, as being heated up to 120 °C under flowing humidified helium, the material underwent a phase transition upon heating between 112 and 116 °C, as can be seen in Figure 5.2a, to a high-temperature phase that gave XRD patterns similar to those of the high-temperature, cubic *P*m-3m phases of other compounds in the $CsHSO_4$-CsH_2PO_4 family [8-11]. On cooling, the reverse transition occurred at a lower temperature between 82 and 78 °C (data not shown). The reflections of the sample after cooling measured immediately at 25 °C appeared at the same 2θ positions as those of the original phase which indicates that the material had transformed back to its low-temperature phase.

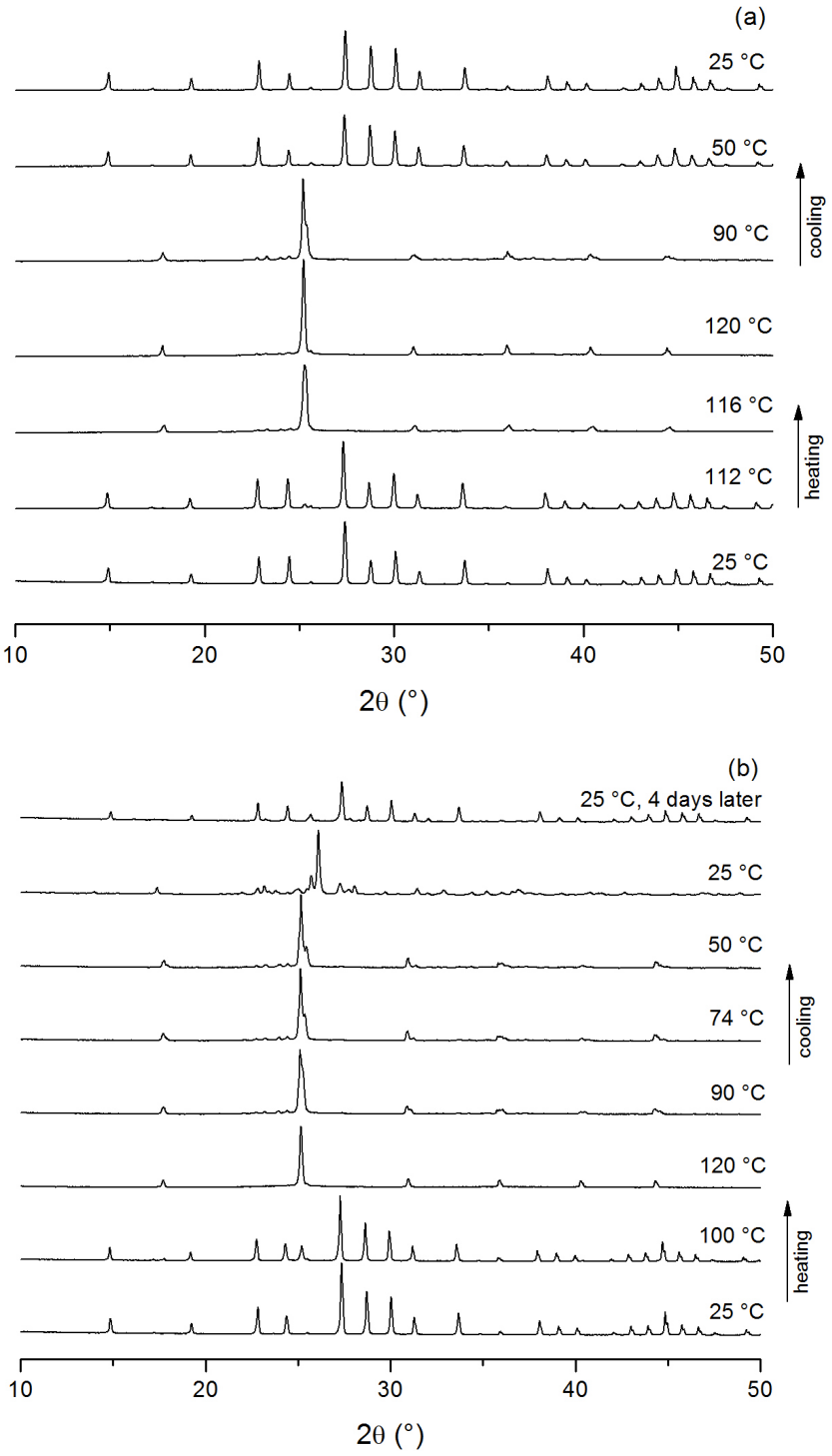

Figure 5.2. (See caption on next page)

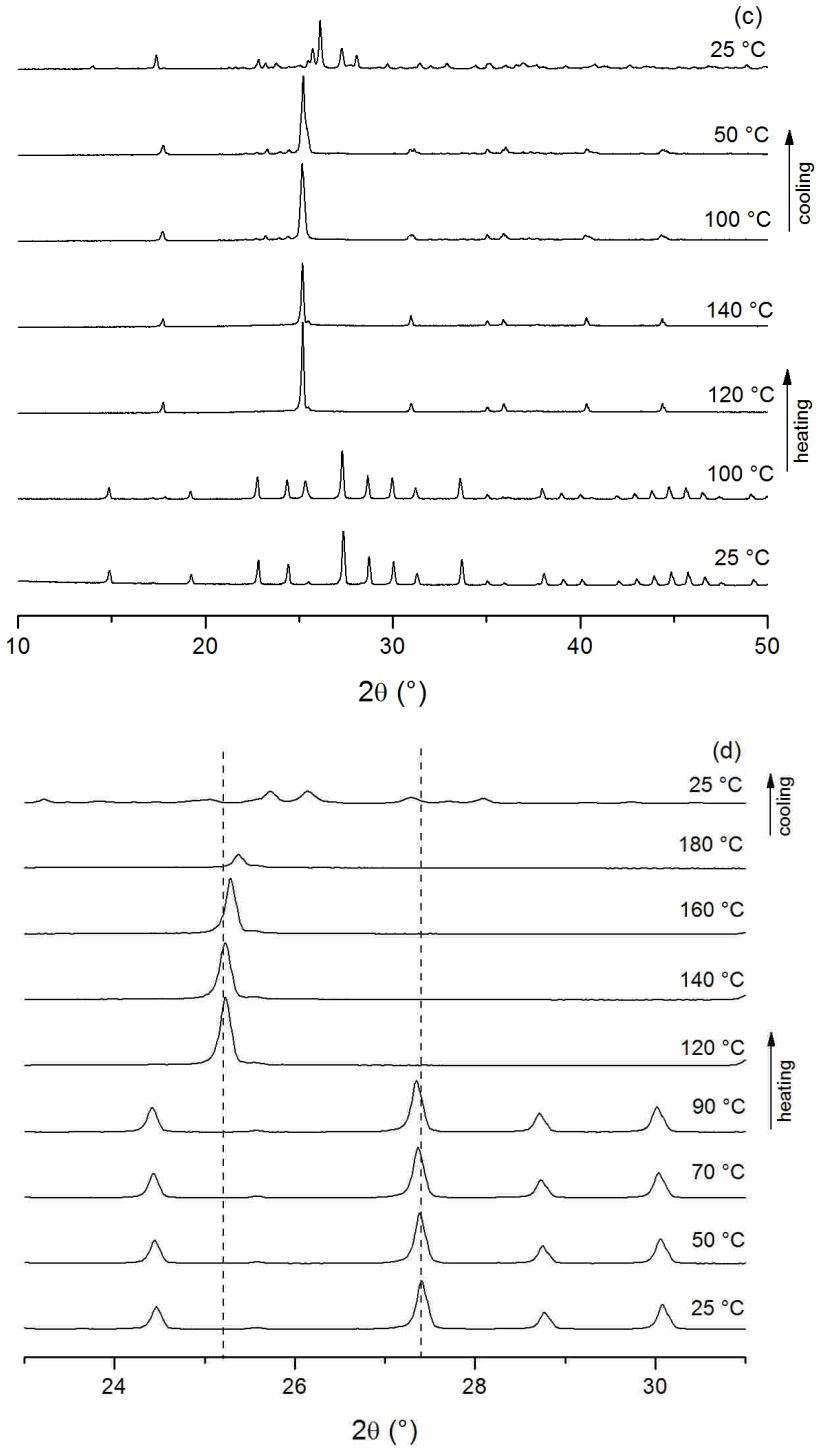

Figure 5.2. XRD patterns of $Cs_6(H_2SO_4)_3(H_{1.5}PO_4)_4$ collected at various temperatures as shown in the figures. (a) under humidified helium with pH_2O ~ 0.023 atm, (b) under dry helium, (c) and (d) under the same atmosphere as in (a) but heated up to 140 and 180 °C, respectively.

Secondly, once again another pellet was heated up to 120 °C similar to the experiment above, but under stagnant ambient atmosphere instead. The XRD patterns in Figure 5.2b show that, on heating, the sample transformed to the high-temperature phase, similar to what was observed previously. On cooling, however, the sample did not transform back to its original phase, even after cooled down to 25 °C as the pattern collected shortly after that revealed. This pattern did not match any of the known solid acids either. The sample looked shiny and its edge looked curved after taken out from the high-temperature chamber as if it was partially melted and solidified. About 4 days after the pellet sample was left at room temperature under ambient atmosphere, another XRD pattern was collected and it showed that the material slowly transformed back to the original phase.

Thirdly, a pellet was examined under the humidified atmosphere used above, but this time heated up to 140 °C. As shown in Figure 5.2c, upon heating, similar patterns were observed. The pattern of the high-temperature phase remained unchanged up to 140 °C, except small shifts of the peak positions due to thermal expansion. On cooling, the sample showed the same behavior as the one that was measured under stagnant atmosphere. That is the reverse transition did not occur right away, but eventually several days later (data not shown). The physical appearance of the pellet after the measurement was also similar to that of the one under stagnant atmosphere.

These three experiments indicated that dehydration might happen around 120 – 140 °C and higher humidity level helped prevent the dehydration to occur. Additionally, the fact that the pellets looked as if they were partially melted supports the possibility of dehydration since many solid acids become liquid when partially dehydrated [12-14].

In an attempt to obtain lattice parameters at various temperatures, Figure 5.2d shows the XRD patterns of the material up to 180 °C under humidified helium. The results from *ab initio* indexing are listed in Table 5.3. In the low-temperature phase, even though the material is cubic, unlike many other solid acids that are monoclinic, it did behave alike, i.e. it expanded as the temperature went up. Above the transition temperature, on the other hand, the peaks in the diffraction patterns shifted to higher angle, which could lead one to think of "negative thermal expansion". The same behavior was also previously observed by Chisholm [9] for this material and $Cs_6(H_2SO_4)_3(H_{1.5}PO_4)_4$ is so far the only solid acid that shows this behavior.

Table 5.3. Lattice parameter of $Cs_6(H_2SO_4)_3(H_{1.5}PO_4)_4$ at various temperatures under humidified helium (pH_2O ~ 0.023 atm).

Phase	Space Group	Temperature (°C)	a_0 (Å)
Body-centered cubic	*I*-43d	25	14.5413(3)
		50	14.5566(3)
		70	14.5657(2)
		90	14.5756(2)
Primitive cubic	*P*m-3m	120	4.9902(1)
		140	4.9912(2)
		160	4.9776(2)
		180	4.9641(9)

Nevertheless, Figure 5.3 demonstrates the effect of the humidity levels on the material and hence on the peak positions. Only the peak at about 25.3° of 2θ was shown in the figure although the full range of the diffraction data were collected. It was found that, as the sample was held at a fixed temperature, 120 °C, and the atmosphere was switched back and forth between humidified (pH_2O ~ 0.023 atm) and dry helium, the peak position really changed accordingly. Specifically, under humidified gas, the reflection appeared at a lower angle, while under dry condition, it shifted to a higher

angle. It was clear that every time the sample exposed to the same level of humidity, the peak lined up at exactly the same position. The lattice parameter of the sample under humidified and dry conditions were determined using *ab initio* indexing and listed in Table 5.4.

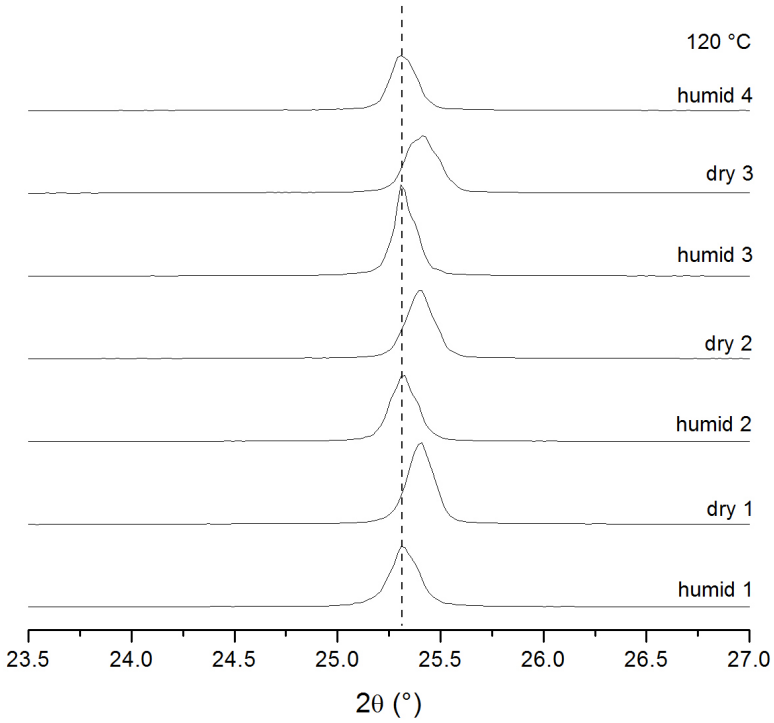

Figure 5.3. XRD patterns of $Cs_6(H_2SO_4)_3(H_{1.5}PO_4)_4$ at 120 °C under alternating atmosphere between humidified (pH_2O ~ 0.023 atm) and dry helium.

Table 5.4. Lattice parameter of $Cs_6(H_2SO_4)_3(H_{1.5}PO_4)_4$ at 120 °C under humidified (pH_2O ~ 0.023 atm) and dry helium.

Step	a_0 (Å)
Humidified 1	4.9950(6)
Dry 1	4.9729(3)
Humidified 2	4.9914(3)
Dry 2	4.9715(2)
Humidified 3	4.9909(6)
Dry 3	4.970(1)
Humidified 4	4.9918(6)

This finding supports the hypothesis that dehydration occurs around this temperature range and the process is reversible, i.e. the only decomposition product leaving the sample is water vapor and the remaining product has a smaller unit cell and once the material reabsorbs water, it can transform back to the original phase. Furthermore, this result suggests that the cause of the shift of the peaks to higher angles in the XRD patterns of the high-temperature phase in Figure 5.2d is related to the dehydration. As the water partial pressure is fixed, increasing temperature will dehydrate the material more, making more $Cs_6(H_2SO_4)_3(H_{1.5}PO_4)_4$ decompose to the product with a smaller unit cell and therefore, the negative-thermal-expansion-like behavior was observed. This also implies that the decomposition product must give a very similar diffraction pattern and even have a very similar crystal structure. The high-temperature phases of the compounds in $CsHSO_4$-CsH_2PO_4 family such as $Cs_2(HSO_4)(H_2PO_4)$, $Cs_3(HSO_4)_2(H_2PO_4)$, or $Cs_5(HSO_4)_3(H_2PO_4)_2$ are promising candidates for this decomposition product since they all have the same space group, *P*m-3m, and their unit cells are about the same size among one another, but smaller than that of $Cs_6(H_2SO_4)_3(H_{1.5}PO_4)_4$ at high temperatures [9-11].

5.5 Physical Observation of a Crystal Sample

In many solid acids, microcracks form when their crystals are heated up beyond the transition temperature and cooled down. The formation of these cracks makes the crystals turn cloudy as in the case of CsH_2PO_4 depicted in Figure 5.4a. Nonetheless, $Cs_6(H_2SO_4)_3(H_{1.5}PO_4)_4$ acts differently from those solid acids. Either heat-treated under humidified or stagnant atmospheres, the crystal remained clear. Shown in Figure 5.4 b-d,

optical images and SEM micrographs of a crystal of this compound displayed no cracks at all, but it can be seen in the micrographs of the crystal treated under stagnant condition, Figure 5.4d, that the surface and edges of the crystal became rougher, suggesting a sign of dehydration.

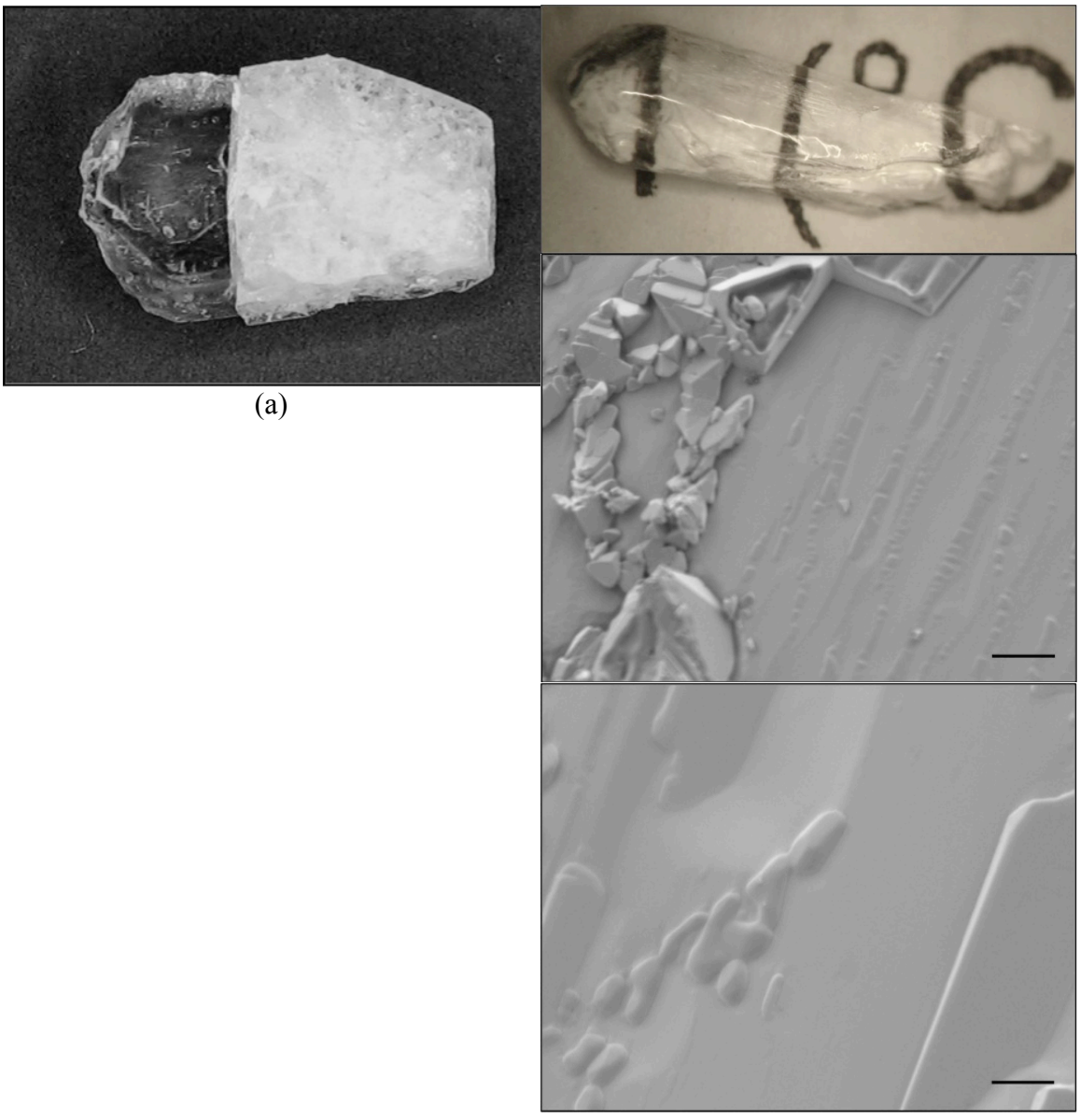

(a)

(b)

Figure 5.4. (See caption on next page)

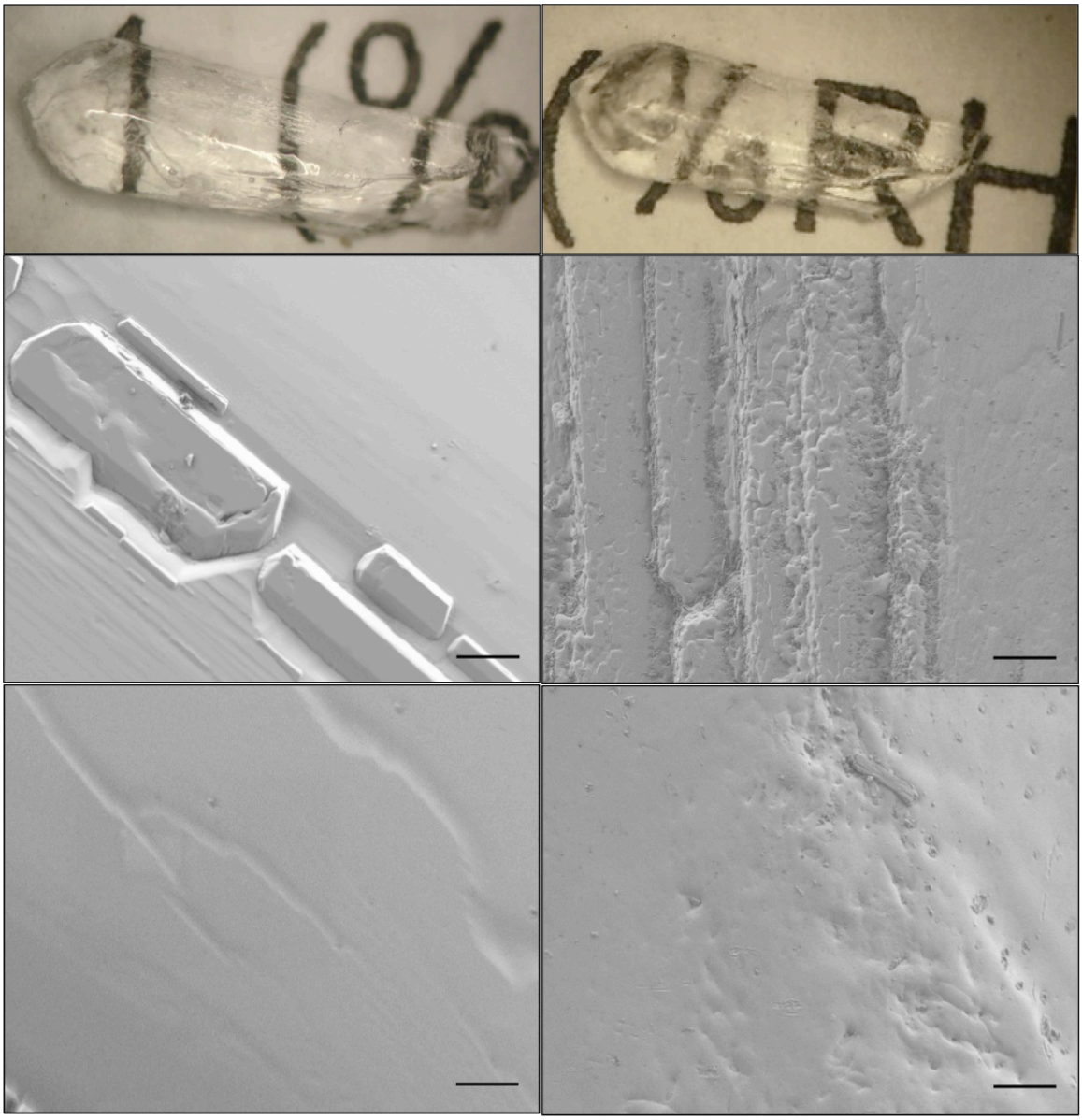

(c) (d)

Figure 5.4. (a) Optical image of CsH_2PO_4 before (left) and after (right) heating beyond the superprotonic transition [15]. (b)-(d) Optical images (top) and SEM micrographs (middle = 1000×, bottom = 2000×) of $Cs_6(H_2SO_4)_3(H_{1.5}PO_4)_4$: (b) before heat treatment, (c) after heating under humidified (pH_2O ~ 0.023 atm) nitrogen, and (d) after heating under ambient atmosphere (pH_2O ~ 0.011 atm).

5.6 Conductivity Measurements

The conductivities of $Cs_6(H_2SO_4)_3(H_{1.5}PO_4)_4$ measured in the single-frequency mode under humidified and dry nitrogen are shown in Figure 5.5. Like many other solid

acids, $Cs_6(H_2SO_4)_3(H_{1.5}PO_4)_4$ showed the superprotonic behavior. A sharp increase in conductivity arise in each case at about the same temperature, ~ 97 °C, where the conductivity dramatically increased by 3-4 orders of magnitude, from 8.76×10^{-7} to 1.68×10^{-3} S/cm for the humidified case and from 7.05×10^{-7} to 1.84×10^{-3} S/cm for the dry. Although the transition temperatures on heating in both cases were at a lower temperature compared to that observed in the HT-XRD experiments, the reverse transitions were consistent. Under the humidified condition, the reverse transition occurred at ~ 78 °C and finished at a temperature slightly below 70 °C, while the conductivity of the sample under the dry atmosphere remained high until 60 °C where the temperature cycle ended and decreased very slowly down to its initial value in a period of 2-3 days.

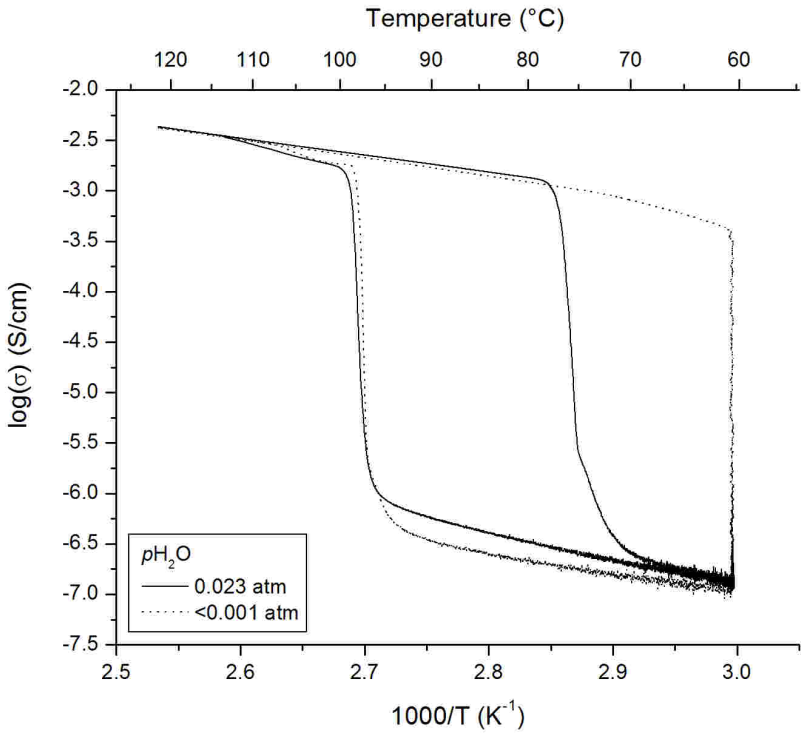

Figure 5.5. Conductivity of $Cs_6(H_2SO_4)_3(H_{1.5}PO_4)_4$ measured at 2 kHz under humidified (pH_2O ~ 0.023 atm) and dry nitrogen at a ramp rate of 0.1 °C/min.

5.7 Determination of Heat of Transition and Study of Dehydration

Figure 5.6 illustrates the DSC profiles of the material under the three humidity levels listed in the legend, heated up to 122 °C. Upon heating, an endothermic peak was detected in all cases at an onset temperature of about 113.5 °C. The enthalpies of transitions associating with these peaks, listed in Table 5.5, were around 110 kJ per mole $Cs_6(H_2SO_4)_3(H_{1.5}PO_4)_4$ or 17 kJ per mole of $CsHXO_4$ unit where 6.43 units were assigned to $Cs_6(H_2SO_4)_3(H_{1.5}PO_4)_4$ based on the formula weight. On cooling, only the sample in the higher humidity transformed back to its low-temperature phase as indicated by an exothermic peak at ~ 74 °C. The corresponding enthalpy was however lower than that of the endothermic peak, suggesting that a part of the sample did not undergo the reverse transition. The DSC signal from the experiment under the lower humidity was broad and spread over a wide temperature range, 70 – 30 °C, while the signal was almost undetected for the sample under the dry condition, indicating that the samples did not change back at all. The outcomes were also consistent with those from conductivity and high-temperature XRD measurements.

Table 5.5. Onset temperatures, enthalpies, and entropies of transitions of the samples heated up to 122 °C under three different humidity levels.

Step	pH_2O (atm)	T_{sp}-onset (°C)	ΔH (kJ/mol)	ΔS (J/mol·K)	ΔH* (kJ/mol)	ΔS* (J/mol·K)
Heating	0.023	113.3	107.5	278.2	16.72	43.28
	0.011	113.8	110.7	286.2	17.22	44.53
	< 0.001	114.1	106.7	275.6	16.60	42.88
Cooling	0.023	74.1	73.9	213.0	11.50	33.14
	0.011	68.0	34.0	99.7	5.29	15.51
	< 0.001	69.9	22.3	65.0	3.47	10.12

* Values per $CsHXO_4$ unit. $Cs_6(H_2SO_4)_3(H_{1.5}PO_4)_4$ has 6.43 units based on the formula weight.

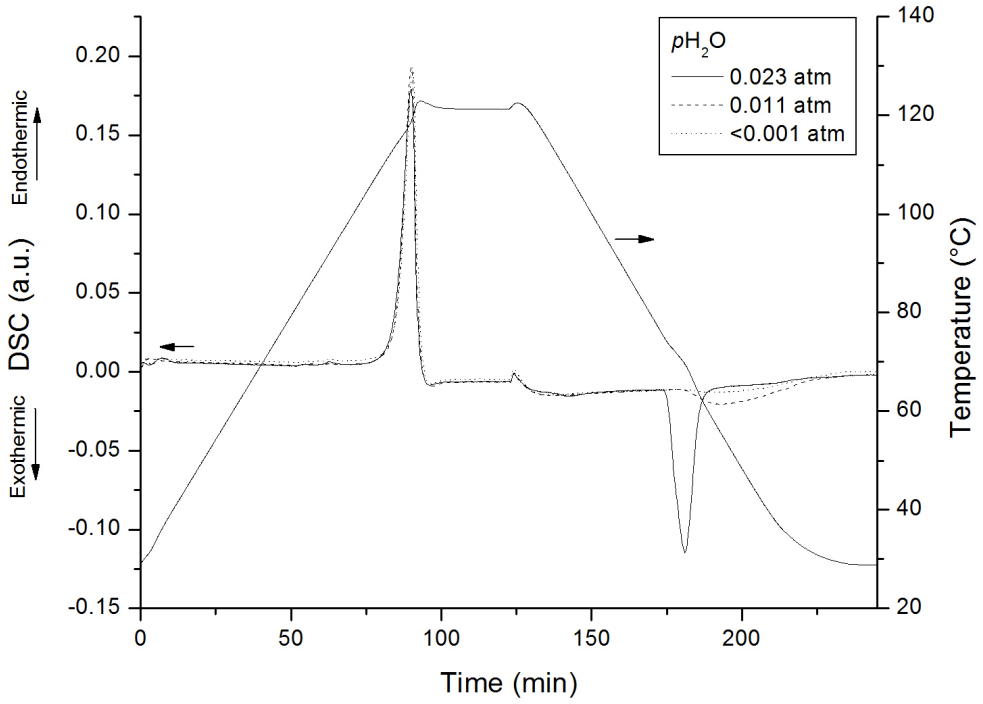

Figure 5.6. DSC profiles of $Cs_6(H_2SO_4)_3(H_{1.5}PO_4)_4$ measured under three different humidity listed in the legend up to 122 °C at a ramp rate of 1 °C/min.

Another set of DSC/TG measurements was conducted to study the dehydration of the material. The DSC profiles in Figure 5.7 agreed well with the findings from other experiments. The endothermic peaks emerged at the same temperature as in the previous experiments. Since all three samples were intended to be dehydrated, there were no exothermic peaks observed on cooling as expected. The TG profiles showed that the dehydration temperature increased as the humidity increased. In other words, the water vapor helped prevent the dehydration of the material. The data also confirmed that at a fixed water partial pressure, the sample dehydrated more as the temperature raised.

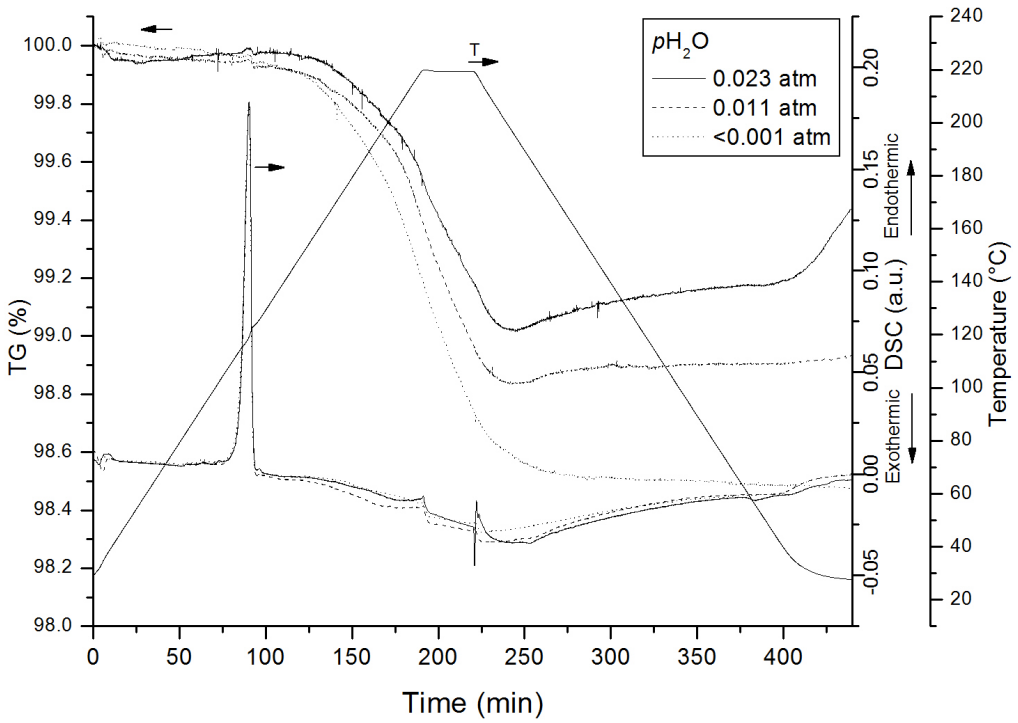

Figure 5.7. DSC and TG profiles of $Cs_6(H_2SO_4)_3(H_{1.5}PO_4)_4$ heated up to 220 °C under three different humidity listed in the legend at a ramp rate of 1 °C/min.

5.8 Discussion: Mechanism of Transition and Origin of the Apparent Negative Thermal Expansion in $Cs_6(H_2SO_4)_3(H_{1.5}PO_4)_4$

As discussed above, the origin of the apparent negative thermal expansion relates to the dehydration. However, this dehydration might not be the dehydration of the solid acid. This is because partially dehydrated solid acids are usually liquid [12-14] which will not give reflections in an X-ray diffraction pattern. Thus, the fact that the peaks did show up in the diffraction pattern and are very likely to be from a solid acid indicates that the dehydration must occur in another phase that is not crystalline, while the solid acid remained a crystalline solid. This definitely implies that a phase separation is involved, similar to what found in $Rb_3H(SO_4)_2$ in which case the phase separation products are Rb_2SO_4 and the high-temperature phase of $Rb_5H_3(SO_4)_4$ before the latter is dehydrated

and becomes a liquid at a higher temperature, while Rb_2SO_4 remained solid [12, 16], except what is happening in the current study is the opposite. The plausible candidates for the solid acid phase, as mentioned above, are likely to be in the $CsHSO_4$-CsH_2PO_4 family because of the lattice constant and space group, while the other phase could be H_3PO_4 for the following reasons: 1) the stoichiometry of $Cs_6(H_2SO_4)_3(H_{1.5}PO_4)_4$ suggests that there is an extra oxy-anion group which could relatively easily separate to form the acid, 2) H_3PO_4 can be dehydrated in the temperature of interest of this work to form fractions of its dehydrated compounds such as pyrophosphate and triphosphate [17], and 3) H_3PO_4 and its dehydrated products are all liquid in this temperature range. Hence, the proposed reactions involved in the temperature range above 100 °C are as follows:

$$Cs_6(H_2SO_4)_3(H_{1.5}PO_4)_4\ (s, LT) \rightarrow Cs_6(H_2SO_4)_3(H_{1.5}PO_4)_4\ (s, HT) \quad (1)$$

$$Cs_6(H_2SO_4)_3(H_{1.5}PO_4)_4\ (s) \rightarrow Cs_6(H_{2-0.5x}SO_4)_3(H_{1.5}PO_4)_{4-x}\ (s, HT) + x\ H_3PO_4\ (l) \quad (2)$$

$$2\ H_3PO_4\ (l) \rightarrow H_4P_2O_7\ (l) + H_2O\ (g) \quad (3)$$

To explain the proposed reactions in words, the low-temperature (LT) phase of $Cs_6(H_2SO_4)_3(H_{1.5}PO_4)_4$ undergoes superprotonic transition to its high-temperature (HT) phase at a temperature between 110 – 120 °C as described in Reaction (1). Then, Reactions (2) and (3) occur along with the superprotonic transition under low humidity or they can occur at a higher temperature under higher humidity. In Reaction (2), the proposed formula for the partially decomposed product of $Cs_6(H_2SO_4)_3(H_{1.5}PO_4)_4$ is $Cs_6(H_{2-0.5x}SO_4)_3(H_{1.5}PO_4)_{4-x}$ where x = 0-1 indicating the degree of decomposition and this product has a smaller unit cell. As Reaction (3) proceeds to the right, Reaction (2) is

also driven to the right. In other words, the more dehydration occurs, the more decomposed product $Cs_6(H_{2-0.5x}SO_4)_3(H_{1.5}PO_4)_{4-x}$ is formed and the smaller lattice parameter observed which explains the apparent negative thermal expansion behavior. It also should be noted that at x = 1 the solid acid emerged in Reaction (2) could be any of the solid acids in the $CsHSO_4$-CsH_2PO_4 family. $Cs_2(HSO_4)(H_2PO_4)$ is, however, more likely than the others because it fits the stoichiometry proposed in Reaction (2) perfectly and its superprotonic transition temperature is below 100 °C, so it is already in its high-temperature cubic phase when the decomposition occurs. $Cs_5(HSO_4)_3(H_2PO_4)_2$ is another plausible candidate for similar reasons.

5.9 Conclusions

A new solid acid, $Cs_6(H_2SO_4)_3(H_{1.5}PO_4)_4$, was synthesized and confirmed the composition. At room temperature, it is a body-centered cubic in *I*-43d space group with a_0 = 14.5413(4) Å, V = 3074.7(1) $Å^3$, Z = 4, and density = 3.1919 g/cm^3.

According to the combination of the findings from the three techniques above, it can be concluded that $Cs_6(H_2SO_4)_3(H_{1.5}PO_4)_4$ transforms from its low-temperature, low-conductivity phase to its high-temperature, high-conductivity phase at a temperature between 110 – 120 °C with a heat of transition of ~ 17 kJ per mole of $CsHXO_4$ unit and the dehydration process also starts about the same temperature. The dehydration observed in this work is not that of the solid acid itself as found in other cases, but is of one of the phase separation products, H_3PO_4, while the other, proposed to be $Cs_6(H_{2-0.5x}SO_4)_3(H_{1.5}PO_4)_{4-x}$, remains solid. The humidity in the gas phase controls the degree of the dehydration, which is the cause of the apparent negative thermal expansion.

The dehydrated products eventually reabsorbs water and recombines to form $Cs_6(H_2SO_4)_3(H_{1.5}PO_4)_4$ under the ambient condition over the course of a few days.

5.10 References

[1] C.R.I. Chisholm, S.M. Haile, *Acta Crystallogr B* **55** (1999) 937.

[2] C.R.I. Chisholm, S.M. Haile, *Mater Res Bull* **35** (2000) (7) 999.

[3] S.M. Haile, P.M. Calkins, *J Solid State Chem* **140** (1998) (2) 251.

[4] S.M. Haile, P.M. Calkins, D. Boysen, *J Solid State Chem* **139** (1998) (2) 373.

[5] S.M. Haile, K.D. Kreuer, J. Maier, *Acta Crystallogr B* **51** (1995) 680.

[6] Z. Jirak, M. Dlouha, S. Vratislav, A.M. Balagurov, A.I. Beskrovnyi, V.I. Gordelii, I.D. Datt, L.A. Shuvalov, *Phys Status Solidi A* **100** (1987) (2) K117.

[7] H. Matsunaga, K. Itoh, E. Nakamura, *J. Phys. Soc. Jpn.* **48** (1980) (6) 2011.

[8] A. Preisinger, K. Mereiter, W. Bronowska, *Mater Sci Forum* **166** (1994) 511.

[9] C.R.I. Chisholm, Superprotonic Phase Transitions in Solid Acids: Parameters affecting the presence and stability of superprotonic transitions in the MHnXO4 family of compounds (X=S, Se, P, As; M=Li, Na, K, NH4, Rb, Cs), *Materials Science*, California Institute of Technology, Pasadena, California (2003).

[10] S. Takeya, S. Hayashi, H. Fujihisa, K. Honda, *Solid State Ionics* **177** (2006) (15-16) 1275.

[11] C.R.I. Chisholm, S.M. Haile, *Solid State Ionics* **136** (2000) 229.

[12] L.A. Cowan, R.M. Morcos, N. Hatada, A. Navrotsky, S.M. Haile, *Solid State Ionics* **179** (2008) (9-10) 305.

[13] A. Ikeda, S.M. Haile, *Solid State Ionics* **213** (2012) 63.

[14] Y. Taninouchi, T. Uda, Y. Awakura, *Solid State Ionics* **178** (2008) (31-32) 1648.

[15] M.W. Louie, Electrocatalysis in solid acid fuel cells, *Chemical Engineering*, California Institute of Technology, Pasadena, California (2011).

[16] C. Panithipongwut, S.M. Haile, *Solid State Ionics* **213** (2012) 53.

[17] C.E. Higgins, W.H. Baldwin, *Anal Chem* **27** (1955) (11) 1780.

Appendix A Phase Behavior of $(Cs_xRb_{1-x})_3H(SO_4)_2$ Solid Solution System

A.1 Introduction

In spite of the fact that many solid acids in the family $M_3H(XO_4)_2$, where M = Cs, Rb, K, NH_4; and X = S, Se, such as $Cs_3H(SeO_4)_2$, $Rb_3H(SeO_4)_2$, $Rb_3H(SO_4)_2$, exist and stable at room temperature, $Cs_3H(SO_4)_2$ does not. Even though there are some groups that claimed they had synthesized $Cs_3H(SO_4)_2$, they had never showed any proof that they actually had got the correct compound. Additionally, although $Rb_3H(SO_4)_2$ exists at room temperature, it disproportionates at a high temperature and does not show its own superprotonic phase [1, 2]. This study of $(Cs_xRb_{1-x})_3H(SO_4)_2$ is an attempt to stabilize both $Cs_3H(SO_4)_2$ at room temperature and $Rb_3H(SO_4)_2$ at an elevated temperature.

A.2 Synthesis and Characterizations

A.2.1 Synthesis

The solid solutions were prepared from aqueous solutions of rubidium sulfate (Rb_2SO_4, Alfa Aesar 99%), cesium sulfate (Cs_2SO_4, Alfa Aesar 99.99%), and sulfuric acid (H_2SO_4, EMD Chemicals 95-98%) with different ratios. The solutions were poured into methanol to induce precipitation of the solid solutions. The products were then filtered, rinsed with methanol, and dried in a drying oven at ~ 100 °C overnight prior to further characterizations.

A.2.2 Characterizations using XRD, ACIS, and DSC/TG

All of the measurement parameters and settings were the same as those used in Chapter 3 for $Rb_3H(SO_4)_2$-$RbHSO_4$ system except the temperatures of the measurement were adjusted accordingly as shown in the following figures.

A.3 Results

The solubility limit was determined by XRD measurements at room temperature as shown in Figure A.1. It can be seen that additional peaks showed up in the patterns of above 20% Cs, so Cs ions can dissolve into the rubidium structure up to about 20% mole Cs and this composition was selected to represent the solid solution system in further characterizations.

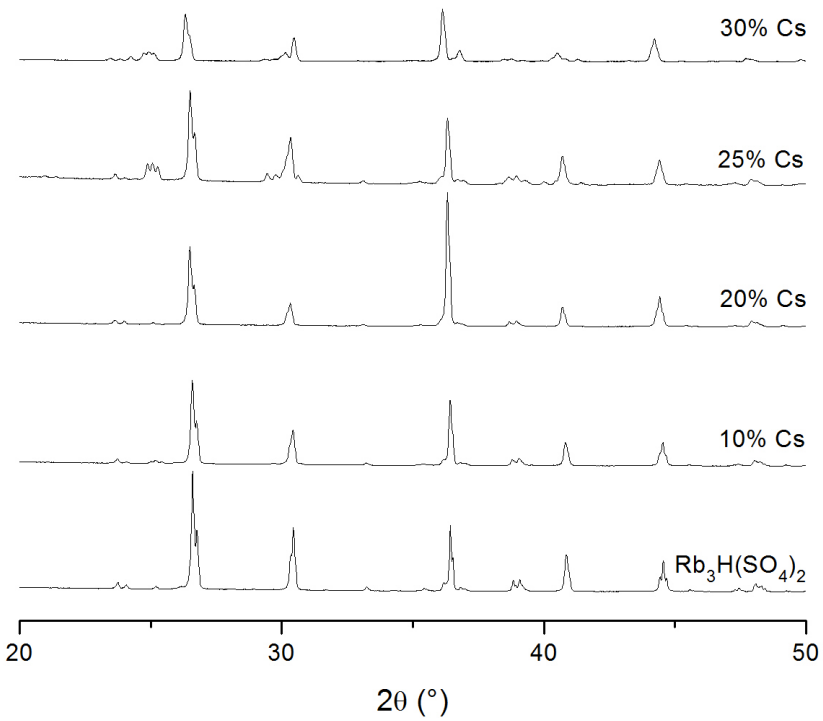

Figure A.1. XRD patterns of $(Cs_xRb_{1-x})_3H(SO_4)_2$, x = 0, 0.1, 0.2, 0.25, and 0.3 at room temperature.

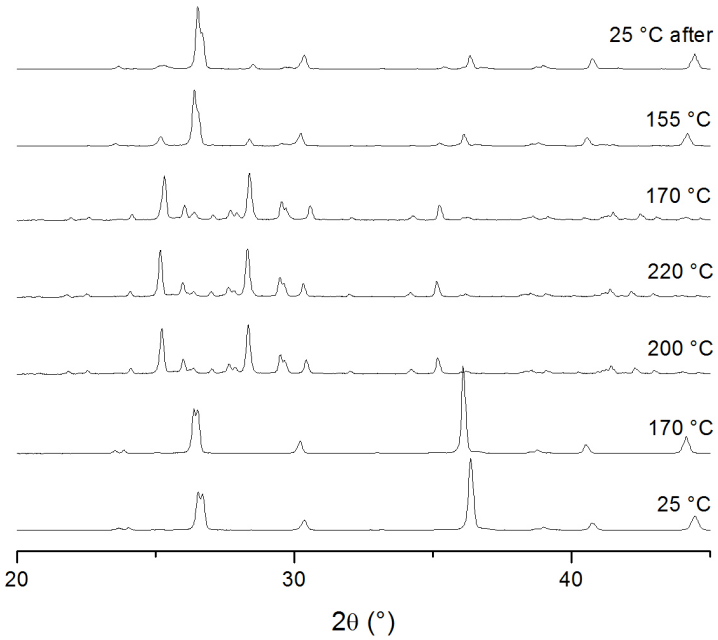

Figure A.2. XRD patterns of $Cs_{0.6}Rb_{2.4}H(SO_4)_2$ at high temperature under humidified He (pH_2O ~ 0.23 atm).

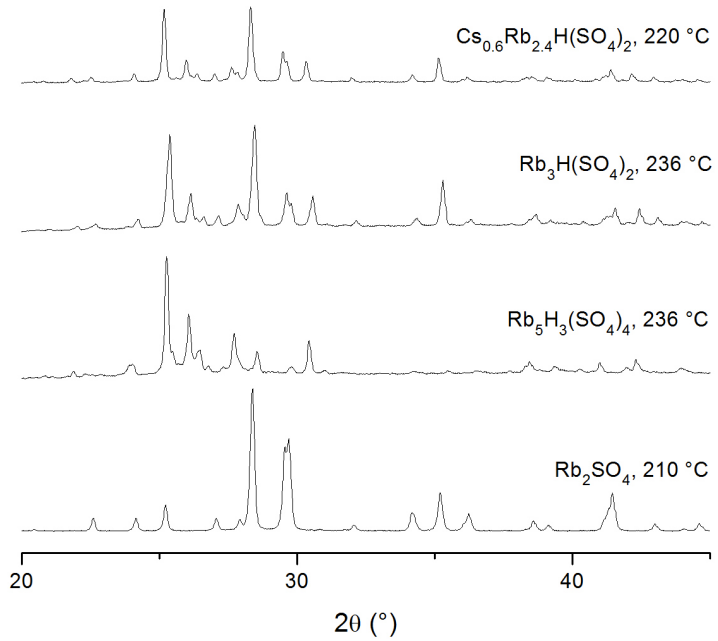

Figure A.3. XRD pattern of $Cs_{0.6}Rb_{2.4}H(SO_4)_2$ at 220 °C under humidified He (pH_2O ~ 0.23 atm) compared with high-temperature patterns of $Rb_3H(SO_4)_2$, $Rb_5H_3(SO_4)_4$, and Rb_2SO_4 at the temperatures as indicated in the figure.

Upon heating to 220 °C, the low-temperature phase of the 20%-Cs composition was stable up to at least 170 °C before a reaction occurred between 170 and 200 °C as illustrated in Figure A.2. The resulting XRD pattern of this reaction was compared to those of $Rb_3H(SO_4)_2$ and $Rb_5H_3(SO_4)_4$ at 236 °C, Figure A.3, and found that the pattern was consisted of those of $Rb_5H_3(SO_4)_4$ and Rb_2SO_4, similar to what was found in the pattern of $Rb_3H(SO_4)_2$. Therefore, this reaction of the solid solution is also a disproportionation similar to that of $Rb_3H(SO_4)_2$, but takes place at a lower temperature.

The solid solution also displayed superprotonic behavior as can be seen in Figure A.4. The conductivity rose quickly at ~ 186 °C for about 4 orders of magnitude and on cooling, started dropping sharply at 167 °C. Similar to $Rb_3H(SO_4)_2$, the apparent superprotonic behavior is expected to be from a high-temperature phase of the solid solution of $Rb_5H_3(SO_4)_4$.

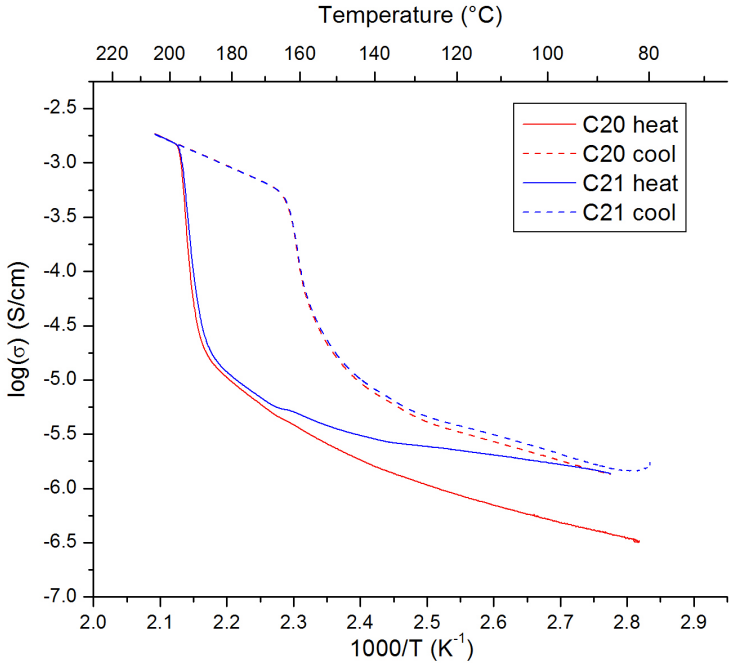

Figure A.4. Conductivity plots of $Cs_{0.6}Rb_{2.4}H(SO_4)_2$ upon heating (solid lines) and cooling (dotted lines) under humidified nitrogen (pH_2O ~ 0.023 atm) at a ramp rate of 0.5 °C/min up to 210 °C.

The DSC profiles, Figure A.5, revealed that there were two endothermic processes upon heating to 220 °C at 165 and 180 °C. The former is still unidentified, the latter is assigned to the disproportionation observed in the HT-XRD since it falls into the temperature range and is close to the transition temperature in the conductivity measurement. The enthalpy associating with this disproportionation is 15.1 kJ/mol, close to 17.8 kJ/mol of disproportionation of $Rb_3H(SO_4)_2$ [1].

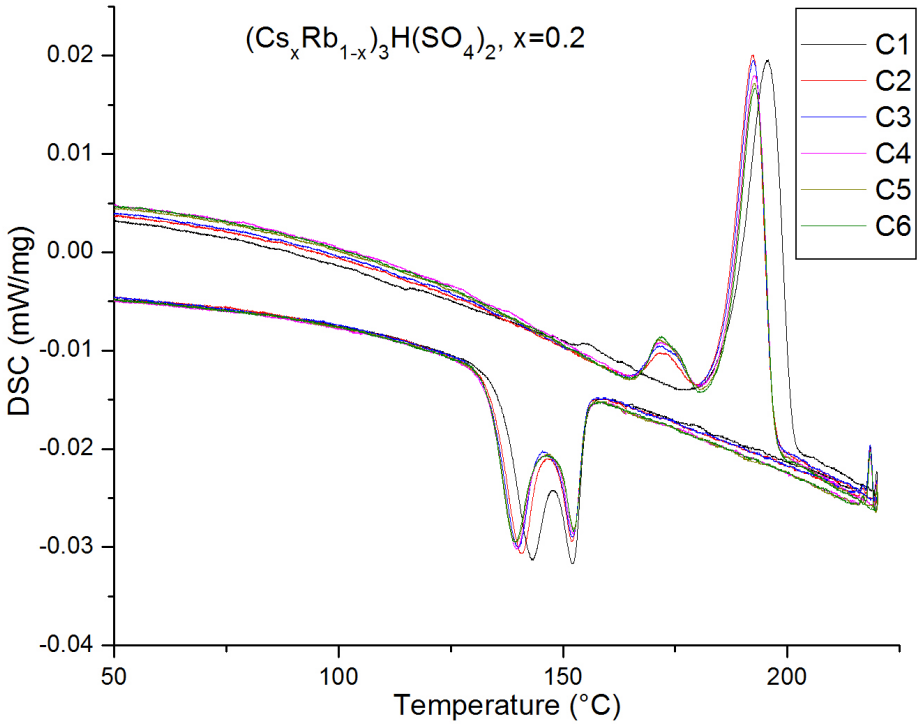

Figure A.5. DSC profiles of $Cs_{0.6}Rb_{2.4}H(SO_4)_2$ under humidified nitrogen (pH_2O ~ 0.023 atm) at a ramp rate of 2 °C/min up to 220 °C.

Figure A.6 shows that the solid solution started dehydrating at a temperature as low as 230 °C. It is inconclusive whether the dehydration stops after 0.9% weight loss or it could continue if the sample is heated up to a higher temperature or kept at 300 °C for longer time.

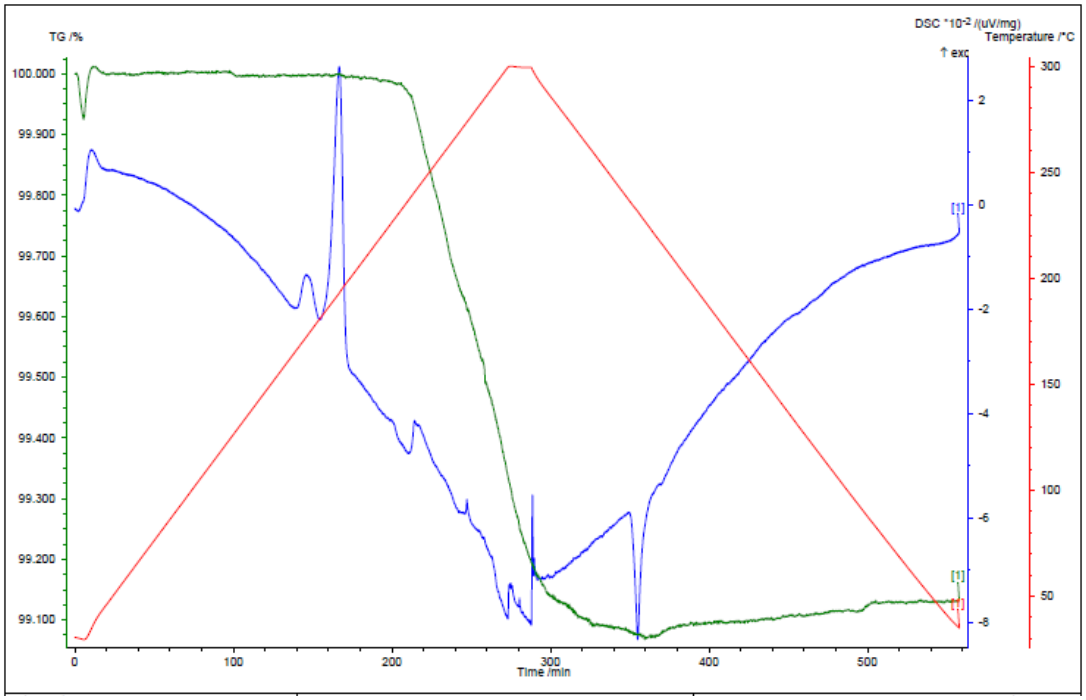

Figure A.6. DSC/TG profile of $Cs_{0.6}Rb_{2.4}H(SO_4)_2$ under humidified nitrogen (pH_2O ~ 0.023 atm) at a ramp rate of 1 °C/min up to 300 °C.

A.4 Conclusions

The solubility limit of Cs ions into $Rb_3H(SO_4)_2$ structure at room temperature is just about 20% mole Cs and not more than 25%; thus, $Cs_3H(SO_4)_2$ cannot be stabilized. At a temperature about 180 °C, the 20%-Cs solid solution disproportionates similar to $Rb_3H(SO_4)_2$, but a lower temperature and does not undergo a polymorphic transition either. The apparent superprotonic behavior is expected to be from another phase similar to $Rb_5H_3(SO_4)_4$.

A.5 References

[1] L.A. Cowan, R.M. Morcos, N. Hatada, A. Navrotsky, S.M. Haile, *Solid State Ionics* **179** (2008) (9-10) 305.

[2] C. Panithipongwut, S.M. Haile, *Solid State Ionics* **213** (2012) 53.

Appendix B Electrospray for Complex Solid Acid Syntheses

* This work was a part of the SURF program in summer 2012. Most of the lab work in this appendix was performed by Jeffrey Kowalski under the supervision of Chatr Panithipongwut and Rob Usiskin.

B.1 Introduction

Solid acids have been prepared via conventional methods such as precipitation, crystallization, and hydrothermal synthesis methods. Many of the solid acids were relatively easy to prepare, either from precipitation or crystallization. Some require slightly different ways to get around some specific issues, for example, the decomposition of selenic acid used in syntheses of selenate compounds. The others are more difficult to make, especially the ones that are more complex like the compounds in the $CsHSO_4$-CsH_2PO_4 family: $Cs_2(HSO_4)(H_2PO_4)$, $Cs_5(HSO_4)_3(H_2PO_4)_2$, $Cs_6(H_2SO_4)_3(H_{1.5}PO_4)_4$. These complex solid acids are obviously composed of many ions that are the same as ions in smaller compounds, which make them hard to be reproduced as a pure phase since the simpler solid acids can co-precipitate easily. Specific ways to reproduce these compounds were reported [1], yet reproducibility is still an issue. The cause of this issue is conjectured to be from concentration gradients of these ions occurring from different mobility in solutions. As the crystallization or the precipitation proceeds, the local concentration of each ion is no longer the same as the stoichiometric concentration. A promising idea to avoid the concentration gradients is to produce small drops of the solutions and quickly force the droplets to precipitate by fast evaporation.

Electrospray has been utilized in fabrication of various types of materials including solid acids. CsH_2PO_4 was the first solid acid successfully electrosprayed [2]

although with a different purpose, to fabricate an intricate nanostructure. This technique meets the proposed resolution above, both producing small droplets and fast evaporation, so it is expected that the correct composition of the complex solid acids can be obtained using electrospray. Varga et al. [2], however, precipitated CsH_2PO_4 out and confirmed the compound before dissolving it again into a solution. In the case of this study, again the conventional methods do not give the desired products, so one of the objectives here is to confirm that solid acids can be obtained directly from solutions of the reactants.

B.2 Sample Preparation and Electrospray

B.2.1 Sample preparation

Water-methanol solutions containing specific ratios of cesium carbonate (Cs_2CO_3, Alfa Aesar 99.99%), cesium sulfate (Cs_2SO_4, Alfa Aesar 99.99%), sulfuric acid (H_2SO_4, EMD Chemicals 95-98%), and phosphoric acid (H_3PO_4, Fisher Scientific 85%) were prepared in volumetric flasks to obtain accurate concentrations. The solutions were prepared fresh or kept in polyethylene bottles with a Parafilm seal for only a short period of time before electrospray. The ratios of these reactants and the desired products are listed in Table B.1.

B.2.2 Electrospray

Electrosprays of the sample solutions were performed using an in-house electrospray chamber constructed by Rob Usiskin. The schematic components of the chamber are shown in Figure B.1. Depending on the solutions, the voltages used were in the range from 6.8 to 8.3 kV; solution flow rate from 0.030 to 0.075 ml/h; gas, stage, and

wall temperatures from 20 to 100 °C; and deposition time from 2 hours to 7 hours. Most of the depositions were done on B-doped Si wafer substrate except one on carbon paper and one on Inconel (Ni-Cr alloys).

Table B.1. Concentrations of desired products and methanol and Cs:P:S mole ratio in solutions used in electrospray experiments.

Desired Product	% Product	% MeOH	Cs:P:S	Formation Equation
CsH_2PO_4	10	3.959	1:1:0	$Cs_2CO_3 + 2\ H_3PO_4 \rightarrow 2\ CsH_2PO_4 + H_2O + CO_2$
CsH_2PO_4	14	0	1:1:0	
CsH_2PO_4	20	0	1:1:0	
$CsHSO_4$	10	7.92	1:0:1	$Cs_2SO_4 + H_2SO_4 \rightarrow 2\ CsHSO_4$
$CsHSO_4$	15	7.92	1:0:1	
$Cs_2(HSO_4)(H_2PO_4)$	15	5	2:1:1	$Cs_2CO_3 + H_3PO_4 + H_2SO_4 \rightarrow Cs_2(HSO_4)(H_2PO_4) + H_2O + CO_2$
$Cs_3(HSO_4)_2(H_2PO_4)$	15	5	3:1:2	$3\ Cs_2CO_3 + 2\ H_3PO_4 + 4\ H_2SO_4 \rightarrow 2\ Cs_3(HSO_4)_2(H_2PO_4) + 3\ H_2O + 3\ CO_2$
$Cs_3(HSO_4)_2(H_2PO_4)$	15	5	10:3:7	
$Cs_5(HSO_4)_3(H_2PO_4)_2$	15	5	29:17:15	$5\ Cs_2CO_3 + 4\ H_3PO_4 + 6\ H_2SO_4 \rightarrow 2\ Cs_5(HSO_4)_3(H_2PO_4)_2 + 5\ H_2O + 5\ CO_2$
$Cs_6(H_2SO_4)_3(H_{1.5}PO_4)_4$	5	20	6:4:3	$3\ Cs_2CO_3 + 4\ H_3PO_4 + 3\ H_2SO_4 \rightarrow Cs_6(H_2SO_4)_3(H_{1.5}PO_4)_4 + 3\ H_2O + 3\ CO_2$
$Cs_6(H_2SO_4)_3(H_{1.5}PO_4)_4$	15	5	6:4:3	
$Cs_6(H_2SO_4)_3(H_{1.5}PO_4)_4$	15	5	20:11:9	

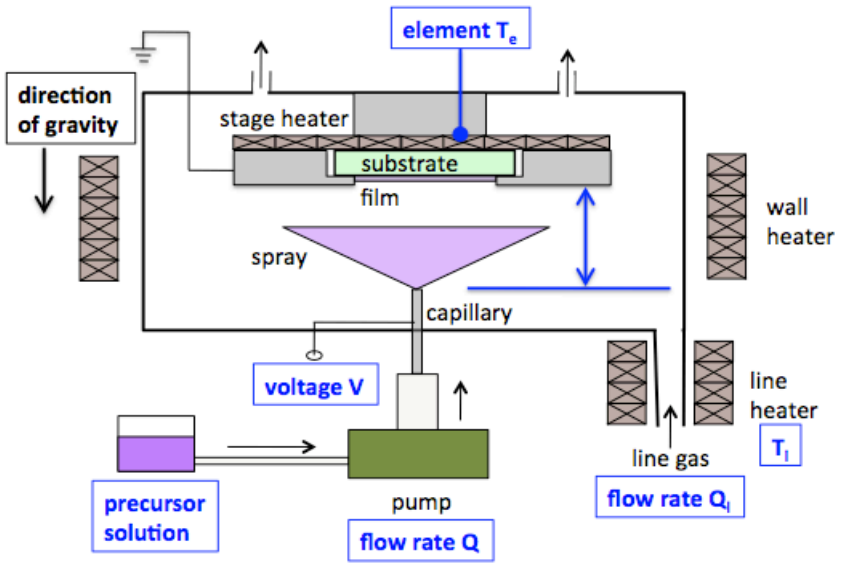

Figure B.1. Schematic of the electrospray chamber components and parameters. Courtesy of Rob Usiskin.

B.3 Results

A SEM micrograph of an electrosprayed CsH_2PO_4 sample, shown in Figure B.2, demonstrate a general resulting deposition of the solid acids studied. In general, there are islets, crystallites, crystals, and large smooth areas. The size of the crystals can be anywhere from 20 to 500 micrometers. The shape of the particles also vary, from a sphere to a needle to a platelet.

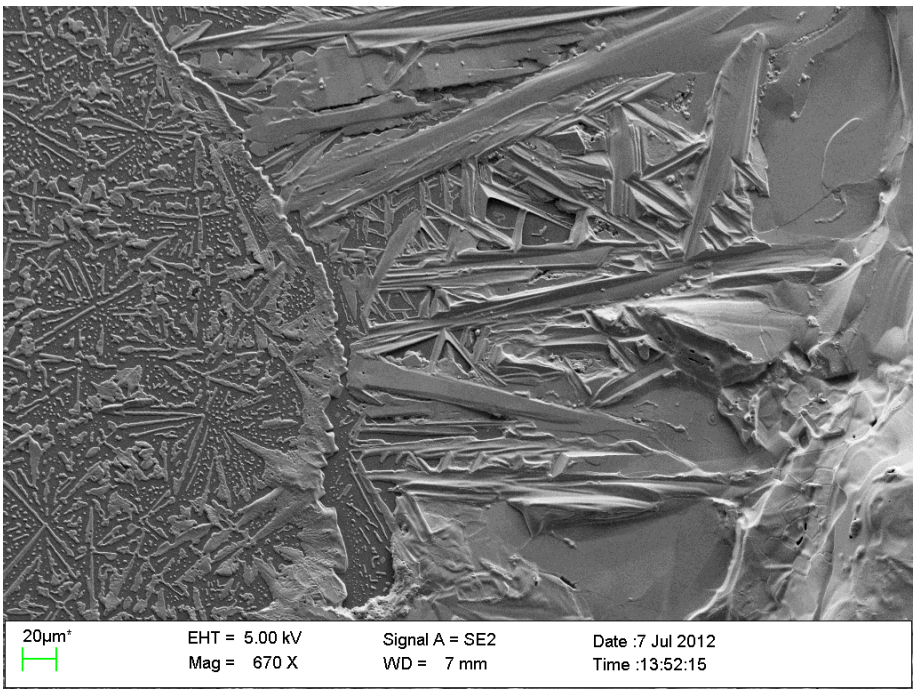

Figure B.2. SEM micrograph of an electrosprayed CsH_2PO_4 sample.

Figure B.3 a to d show XRD patterns of selected samples with those of the references. The pattern of CsH_2PO_4, Figure B.3a, demonstrates that the sample was deposited with a preferred orientation. The two highest peaks were from (200) and (400), respectively. This behavior was also observed in other samples of CsH_2PO_4 and $CsHSO_4$ (data not shown).

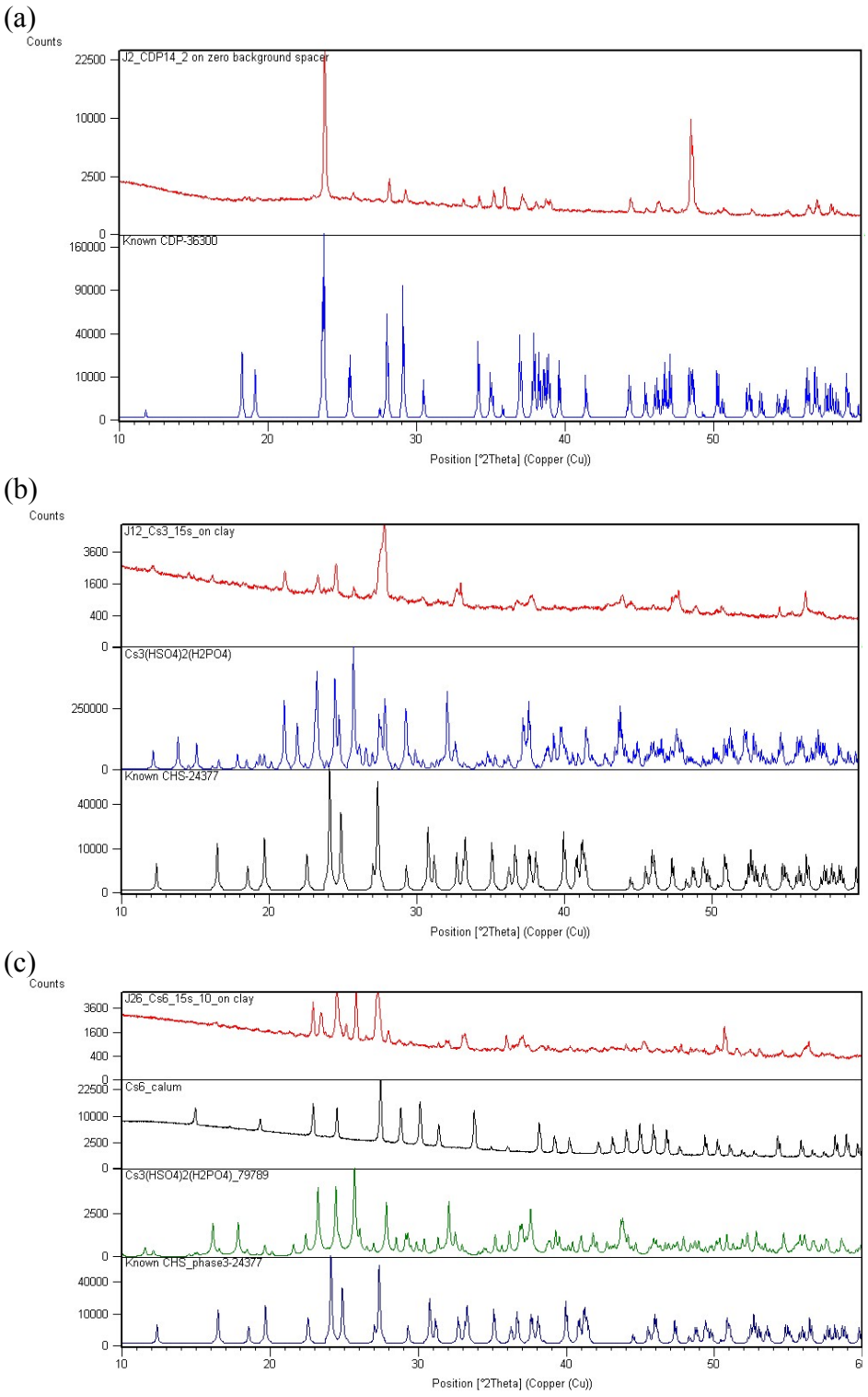

Figure B.3. (See caption on next page)

(d)

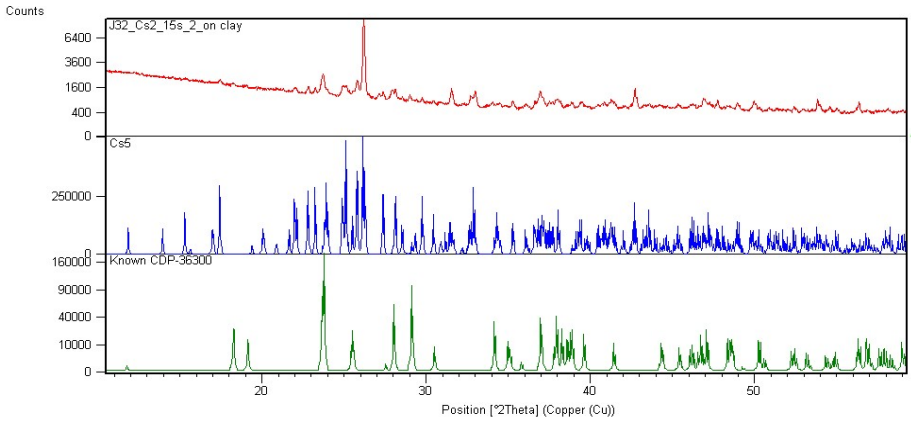

Figure B.3. XRD patterns of electrosprayed samples compared to those of known solid acids. The desired products were (a) CsH_2PO_4, (b) $Cs_3(HSO_4)_2(H_2PO_4)$, (c) $Cs_6(H_2SO_4)_3(H_{1.5}PO_4)_4$, and (d) $Cs_2(HSO_4)(H_2PO_4)$.

The XRD patterns of $Cs_3(HSO_4)_2(H_2PO_4)$, $Cs_6(H_2SO_4)_3(H_{1.5}PO_4)_4$, and $Cs_2(HSO_4)(H_2PO_4)$ in Figure B.3 b-d are somewhat complicated and cannot be identified instantly due to the combination of the already-complicated patterns of the monoclinic solid acids and the orientation effect. By visual comparisons and Rietveld refinements, these patterns can be identified to multiple phases listed in Table B.2. Note that while $Cs_3(HSO_4)_2(H_2PO_4)$ and $Cs_6(H_2SO_4)_3(H_{1.5}PO_4)_4$ formed along with other solid acids from their respective solutions, the deposition of $Cs_2(HSO_4)(H_2PO_4)$ solution resulted in $Cs_5(HSO_4)_3(H_2PO_4)_2$ and CsH_2PO_4 without $Cs_2(HSO_4)(H_2PO_4)$ formed at all.

Backscattered electron (BSE) micrographs and EDS mapping of the selected samples, Figure B.4 and B.5, were taken to find the distributions of the phases in each sample. The BSE results of $Cs_6(H_2SO_4)_3(H_{1.5}PO_4)_4$ and $Cs_2(HSO_4)(H_2PO_4)$, shown in Figure B.4 a and b, revealed that there were three and two phases in the samples, respectively. The brightness of each region in BSE micrographs and the intensities in EDS maps can be used to identify which region is which phase.

Table B.2. Desired and identified products from electrospray determined using XRD.

Desired product	Identified phases
$Cs_3(HSO_4)_2(H_2PO_4)$	$Cs_3(HSO_4)_2(H_2PO_4)$ + $CsHSO_4$
$Cs_6(H_2SO_4)_3(H_{1.5}PO_4)_4$	$Cs_6(H_2SO_4)_3(H_{1.5}PO_4)_4$ + $Cs_3(HSO_4)_2(H_2PO_4)$ + $CsHSO_4$
$Cs_2(HSO_4)(H_2PO_4)$	$Cs_5(HSO_4)_3(H_2PO_4)_2$ + CsH_2PO_4

(a)

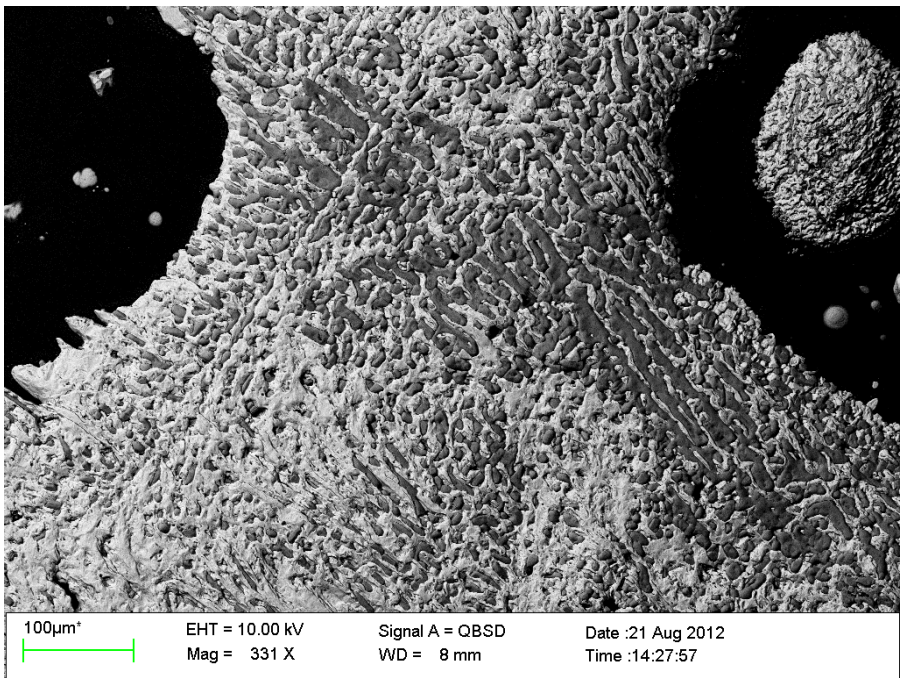

(b)

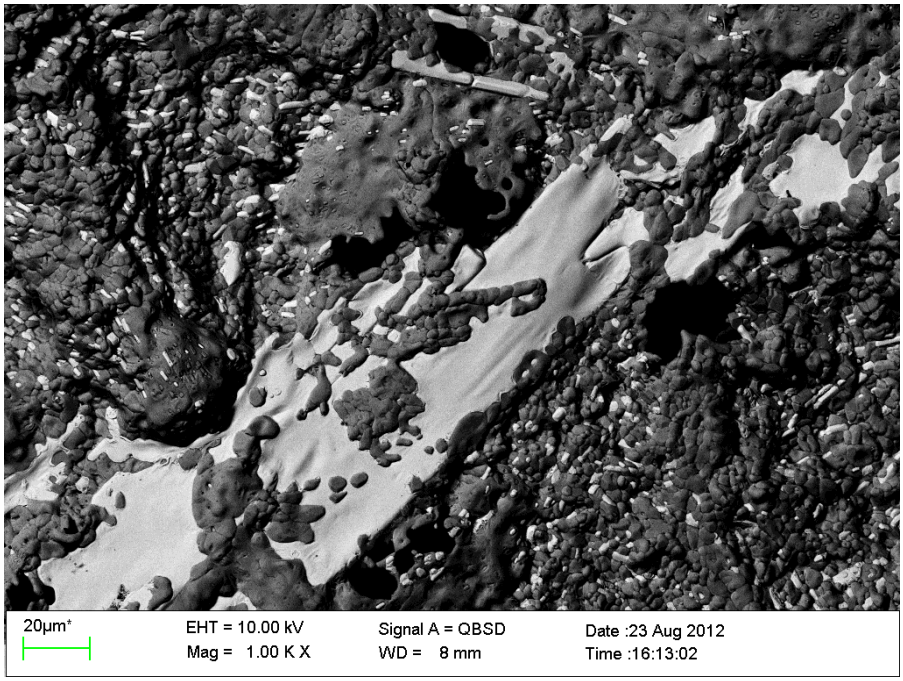

Figure B.4. BSE micrograph of (a) $Cs_6(H_2SO_4)_3(H_{1.5}PO_4)_4$ and (b) $Cs_2(HSO_4)(H_2PO_4)$.

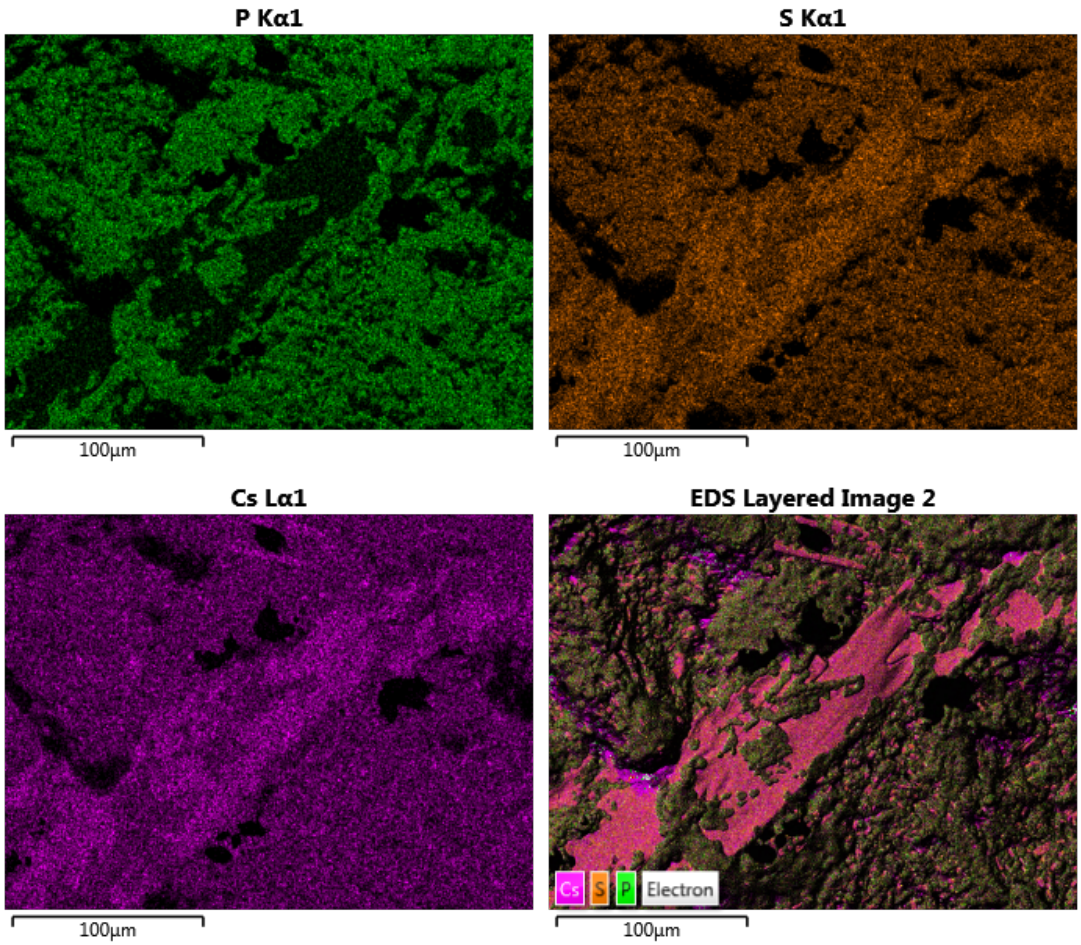

Figure B.5. EDS maps of $Cs_2(HSO_4)(H_2PO_4)$. Different colors and intensities show distributions of different elements: Cs, S, and P.

In BSE technique, lighter elements backscatter electrons less than heavier elements and therefore show darker area in micrographs. In Figure B.4a, since S is heavier than P, the region becomes darker with P content in the compound. Thus, the brightest region corresponds to $CsHSO_4$, the medium grey is $Cs_3(HSO_4)_2(H_2PO_4)$, and the darkest is $Cs_6(H_2SO_4)_3(H_{1.5}PO_4)_4$. For the product of $Cs_2(HSO_4)(H_2PO_4)$ solution, the combination of BSE micrograph (Figure B.4b) and EDS maps (Figure B.5) help identify the two phases: the bright region is $Cs_5(HSO_4)_3(H_2PO_4)_2$ and the dark region is CsH_2PO_4.

B.4 Discussions, Conclusions and Suggestions

Using electrospray to synthesize simple solid acids directly from water-methanol solutions such as $CsHSO_4$ and CsH_2PO_4 is proven to be successful without having to obtain the respective compounds by conventional methods first. Nonetheless, the more complex solid acids which this work attempted to synthesize, $Cs_2(HSO_4)(H_2PO_4)$, $Cs_3(HSO_4)_2(H_2PO_4)$, $Cs_5(HSO_4)_3(H_2PO_4)_2$, and $Cs_6(H_2SO_4)_3(H_{1.5}PO_4)_4$, were not successfully achieved as a pure phase and the phases were also intertwined in each sample, so these phase could not be separated either. The possible causes of this are accumulation of the droplets and difference in migrations of ions under the provided bias.

It was observed for some sprays that droplets accumulated on the substrate and formed a larger drop with a maximum size of about 2 mm, which is large enough for diffusions of ions to occur. To avoid this, the parameters that could be adjusted are temperatures – to make sure that solvents evaporate quickly before droplets approach the substrate – and methanol content – which will lower surface tension of droplets, lower the boiling point of solutions and thus facilitate evaporation of solvents.

Another possible cause is the migration of ions under bias. Ions of different sizes and charges migrate under an electric field with different mobility and this can cause concentration gradients. The migration can occur in the capillary of the electrospray apparatus and when droplets leave the tip of the capillary, the stoichiometry in the droplets differs from the original solution. Since there are several ions involved in formation of these complex solid acids, once the stoichiometry changes, another, undesired solid acid could form easily.

In summary, it is not impossible to synthesize complex solid acids, but definitely there are many parameters that need to be taken into account. More detailed studies of each parameter are required to understand its effect on the synthesis of the complex solid acids.

B.5 References

[1] C.R.I. Chisholm, Superprotonic Phase Transitions in Solid Acids: Parameters affecting the presence and stability of superprotonic transitions in the MHnXO4 family of compounds (X=S, Se, P, As; M=Li, Na, K, NH4, Rb, Cs), *Materials Science*, California Institute of Technology, Pasadena, California (2003).

[2] A. Varga, N.A. Brunelli, M.W. Louie, K.P. Giapis, S.M. Haile, *J. Mater. Chem.* **20** (2010) (30) 6309.